

**Non-equilibrium electron transport
in mesoscale superconducting hybrids**

Non-equilibrium electron transport in mesoscale superconducting hybrids

Proefschrift

ter verkrijging van de graad van doctor
aan de Technische Universiteit Delft,
op gezag van de Rector Magnificus prof. ir. K. Ch. A. M. Luyben,
voorzitter van het College voor Promoties,
in het openbaar te verdedigen op dinsdag 4 juni 2013 om 15:00 uur

door

Nathan VERCRUYSEN

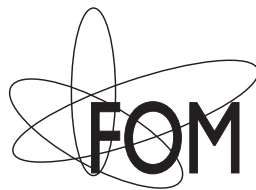
natuurkundig ingenieur
geboren te Antwerpen, België.

Dit proefschrift is goedgekeurd door de promotor:

Prof. dr. ir. T. M. Klapwijk

Samenstelling van de promotiecommissie:

Rector Magnificus,	voorzitter
Prof. dr. ir. T. M. Klapwijk	Technische Universiteit Delft, promotor
Prof. dr. J. P. Pekola	Aalto University School of Science
Prof. dr. M. A. Skvortsov	Landau Institute for Theoretical Physics
Prof. dr. ir. H. W. Zandbergen	Technische Universiteit Delft
Prof. dr. ir. L. M. K. Vandersypen	Technische Universiteit Delft
Dr. Y. M. Blanter	Technische Universiteit Delft
Dr. J. R. Gao	SRON / TU Delft
Prof. dr. ir. H. S. J. van der Zant	Technische Universiteit Delft, reservelid



Printed by: GVO printers & designers | Ponsen & Looijen, Ede, The Netherlands

An electronic version of this thesis is available at:

<http://repository.tudelft.nl>

Copyright © 2013 by N. Vercruyssen. All rights reserved.

Casimir PhD Series, Delft-Leiden, 2013-18

ISBN 978-90-8593-158-4

Contents

1	Introduction	1
1.1	Spontaneous order	2
1.2	Mesoscopic systems	4
1.3	Thesis outline	6
	References	7
2	Driven mesoscale heterostructures	9
2.1	Ordered electronic states	10
2.1.1	Electrons in a lattice	10
2.1.2	Ferromagnetism	12
2.1.3	Superconductivity	14
2.2	Interfaces	15
2.2.1	Length scales	16
2.2.2	Microscopic description	18
2.2.3	Boundary conditions	20
2.3	Driven electrons	21
2.3.1	Diffusive transport	22
2.3.2	Current conversion resistance	23
2.3.3	Energy absorption, relaxation and non-equilibrium	25
2.3.4	Nonlinear transport	28
2.4	Dielectric environment	29
2.4.1	Phonon relaxation	29
2.4.2	Two level systems	30
	References	31
3	Experimental Reality of Model Systems	35
3.1	Introduction	36
3.2	Superconducting nanowires	36
3.3	Aluminium Nitride tunnel barriers	38
3.4	Superconducting resonators	40

References	44
4 Minimal resonator loss for circuit quantum electrodynamics	45
4.1 Introduction	46
4.2 Power dependence of quality factors in NbTiN and Ta resonators	46
4.3 Two level systems	48
4.4 Enhanced quality factors by an optimized device geometry	51
4.5 Conclusions	53
References	53
5 Reduced frequency noise in superconducting resonators	57
5.1 Introduction	58
5.2 Frequency noise due to two level systems	58
5.3 Identifying the location of two level systems	59
5.4 Two level systems in NbTiN resonators	60
5.5 Optimized geometry for minimal frequency noise	64
5.6 Conclusion	64
References	65
6 Substrate-dependent recombination time in superconducting resonators	67
6.1 Introduction	68
6.2 Samples	68
6.3 Relaxation times	69
6.4 Cooling of the resonator	72
6.5 Conclusions	74
References	74
7 Possibility of enhanced cooling by using uniform AlN tunnel barriers	77
7.1 Introduction	78
7.2 Influence of uniformity	78
7.3 Influence of high current densities on the cooling power	83
7.4 Planar junctions	85
7.5 Stacked junctions	87
7.6 Conclusions	89
References	89

8	Evanescent states and non-equilibrium in driven superconducting wires	93
8.1	Introduction	94
8.2	Theoretical framework	96
8.3	Possible solutions	99
8.3.1	One global superconducting state	99
8.3.2	Bimodal superconducting state	102
8.4	Sample design, fabrication and characterization	103
8.4.1	Linear response of the nanowire	104
8.4.2	Characterization of the tunnel probe	106
8.5	Two-state analysis and discussion	108
8.5.1	Global superconducting state	110
8.5.2	Bimodal superconducting state	112
8.6	Conclusion	114
	References	116
9	Spin-dependent current conversion in a superconducting wire	119
9.1	Superconducting proximity effect in ferromagnets	120
9.2	Induced magnetism in superconductors	121
9.3	Current conversion resistance and nonlinear response	123
9.4	Model for spin transport in superconductors	125
9.5	Magnetic field dependence and spin switching	127
9.6	Conclusions and recommendations	129
	References	129
	Summary	133
	Samenvatting	137
	Curriculum Vitæ	141
	List of publications	143
	Acknowledgements	145

Chapter 1

Introduction

1.1 Spontaneous order

This thesis studies the behavior of electrons in solids. The mere existence of a solid state is tacitly accepted as an evident prerequisite. On a microscopic level, the interactions between atoms, nuclei, and electrons are well understood. However it is far from obvious how to understand the emergence of an ordered solid state from the microscopic laws, even if only due to the huge number of particles involved. Furthermore there is no clear reason why the solid state materials we observe are so diverse and so ubiquitously present [1].

The fundamental laws of physics are invariant under translations, rotations, and in time. In other words, no matter at which position, orientation, or moment in time, every experiment should obey the same physical laws. In a solid, the atoms spontaneously form an ordered lattice to lower the ground state energy, as opposed to more random configurations like in a liquid or a gas. The fixed position of atoms seems to contradict translational symmetry, or at least restrict it to translations which are a multiple of the interatomic distance. The key to this paradox lies in the fact that although the laws of physics are symmetrical, order does explicitly break the symmetry of the world around us. The emergence of any type of order is in general accompanied by a reduction of the associated symmetry and a lowered ground state energy, for example the appearance of a crystalline lattice corresponds to ordering in space but a loss of translational symmetry [2, 3].

On the electronic level, the same principles are observed. Electrons in a solid can adopt different macroscopic ground states. An archetypal example is the appearance of the superconducting state in a metal. In the normal state, the electrons behave as free, individual waves, each with a certain amplitude \mathbf{a}_n and phase ϕ_n . When superconducting, the electrons form a collective state characterized by a single macroscopic wave, with a strength Δ and one definite phase ϕ [4]. The driving force behind this behavior is a reduction in the free energy of the electronic system due to attractive electron-electron interactions. However, to benefit from this attractive interaction it is necessary for the electrons to synchronize their phases. This is schematically shown by the potential landscape in Fig. 1.1, representing the energy of the possible ground states of a normal (blue) and a superconducting (green) material. The height of the hills represents the energy of the system; the distance from the center indicates the strength of the emerging order; and the angle ϕ represents the common phase of the electrons. For the normal system the lowest energy state is found at the center of the graph, where the order parameter Δ is zero and the angle ϕ is undefined; the system is symmetrical with respect to the phase. For the superconducting sys-

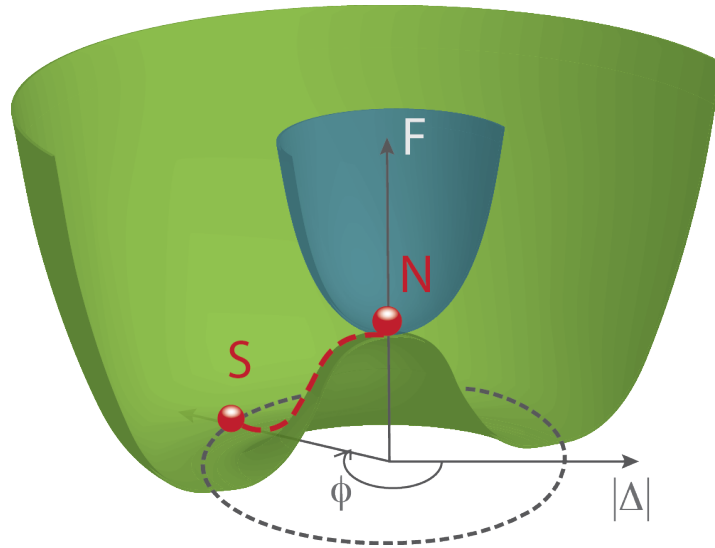


Figure 1.1: The free energy F of a normal metal (blue) and a superconductor (green). In a normal metal, the lowest energy state N is symmetric in phase space. However, in the presence of an attractive interaction between electrons, it becomes favorable for the electronic system to move to an ordered superconducting state S , with a strength $|\Delta|$ and a phase ϕ . Although the energy landscape is still symmetrical with respect to ϕ , the system chooses a particular value of ϕ ; thus breaking the phase symmetry.

tem it is advantageous to move from the center of the landscape to the low-lying valley. Although any angle can be chosen (the laws of physics do not prefer a certain phase), the system breaks this symmetry by picking one specific phase in a process which is called *spontaneous symmetry breaking*.

The emergence of a symmetry-breaking macroscopic state has far-reaching consequences. First, a broken symmetry leads to laws of physics which appear to be different. The broken phase symmetry in a superconductor leads to the London equations [5], which describe electrodynamics that appear different from the usual Maxwell equations. These equations lie at the heart of the superconducting state and explain phenomena such as the Meissner-effect [6], in which a magnetic field is completely screened by a superconductor. Second, the emergence of a collective state leads to macroscopic behavior of microscopic particles. The existence of a macroscopic coherent state in a superconducting ring leads to persistent currents and a quantization of the magnetic flux in quanta of $\phi_0 = \frac{h}{2e}$. The dc Josephson effect [7], in which a dissipationless current flows in between two superconductors with a different phase, is another example of macroscopic coherence. Third, the properties of the collective state are barely dependent microscopic properties of the material. The fact that the flux quantum only depends on fundamental

constants is a clear example. Also the presence of impurities only weakly affects the superconducting state, as long as they don't break time-invariance.

It is fascinating how elegantly these extraordinary phenomena are explained by assuming an organizing principle such as a symmetry-breaking macroscopic state. The robustness of such a collective state to and its weak dependence on the microscopic properties indicate that it is extremely difficult to explain its properties based on microscopic laws only. To grasp the full variety of phenomena at a higher level of complexity there is a need for new fundamental physical principles. Although these are not in contradiction with microscopic theories, it is impossible to reduce the behavior of a collective to the properties of the individual particles, a duck is more than a machine which converts food into droppings (Fig. 1.2).

1.2 Mesoscopic systems

Mesoscopic stems from the ancient Greek words $\mu\epsilon\sigma\omicron$ (middle) and $\sigma\kappa\omicron\pi\eta$ (to look), and means 'to look in the middle', in between different scales. It focusses on observing phenomena which occur at the boundary between various levels of complexity, in between different length, energy or time scales. In solid state physics, mesoscale commonly refers to systems which show both microscopic and macroscopic behavior. They are big enough to show collective phenomena like magnetism or superconductivity. The large number of particles also means that it is impossible to describe each electron independently, making a statistical approach unavoidable. At the same time they are small compared to length scales, associated with physical processes such as quantum interference or energy relaxation. Therefore a description in terms of averaged, macroscopic quantities like temperature or magnetization is insufficient. The mesoscale is thus a region 'in between', where quantum-mechanical behavior, statistics and self-organizing principles are intertwined. Its length scale is not uniquely defined as it depends on the physical processes involved. There is no such thing as a 'mesometer', unlike a nanometer.

Mesoscale devices are small compared to certain relevant length scales, one can no longer resort to a description in terms of an averaged quantity such as temperature. As an example we consider the relaxation of electrical energy which is dissipated in a metallic wire. The metal wire in a light bulb is heated to such an extent by the dissipation of an electrical current, that it starts to glow and radiates light. The notion of temperature is very intuitive to us, a high temperature simply means that an object feels 'hot'. Physically, this corresponds

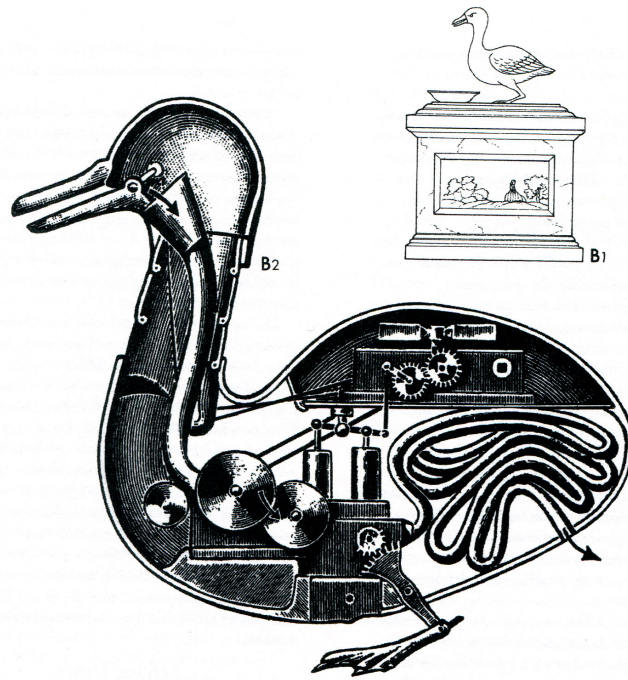


Figure 1.2: A schematic picture of the *Canard Digérateur*, an automaton built by the French artist Jacques de Vaucanson in 1739. In a reductionist view even living things can be reduced to a mechanical system, however a duck is more than a machine which eats grain and produces feces.

to an energy flow from an object at a higher temperature (the bulb) to an object at the lower temperature (your hand). If two objects are strongly coupled, they can easily exchange energy and adapt the same temperature; they are said to be in *thermal equilibrium*. Clearly this does not apply to the wire in the light bulb, as it is more hot than its environment. However, the atoms, electrons, and photons within the wire are strongly coupled, and all have the same, elevated temperature. They are said to be in a local or *quasi-equilibrium*. In the case of a microscopic wire, this intuitive picture breaks down. During the short time spent in the small sample, the driven electrons interact only weakly with each other and the lattice of the solid. Highly energetic electrons can not redistribute their energy. It is impossible to assign a collective temperature to the electrons, and one has to use a more general *non-equilibrium* energy distribution of the electrons.

In heterostructures, materials with different electronic ground states are in close proximity. Near the interfaces between the materials, distinct types of self-organized electronic order compete or interfere, leading to unexplored or unexpected physics. The small size enhances the influence of interfaces and surfaces,

rather than the bulk properties of the materials used. When these hybrid devices are driven by an electric field, different electron properties across the interfaces lead to current conversion processes. For example, near the boundary between a normal metal and a superconductor, a dissipative current of independent electrons is converted into a supercurrent carried by the superconducting condensate. This conversion process happens over a length scale which is inversely proportional to the strength of the superconducting order and can easily exceed the size of the device. The energy dissipation associated with the current conversion processes lead to non-equilibrium electron distributions which can not be characterized with a collective temperature. Mesoscale heterostructures therefore form an ideal playground to study the interaction between such non-equilibrium processes and a non-homogeneous electronic ground state.

1.3 Thesis outline

This thesis focusses on driven superconducting heterostructures. Both experimentally and theoretically we address the following questions: (a) how does the presence of different metallic and dielectric materials influence the electronic properties of a driven superconductor? (b) how does a non-equilibrium electron distribution arise and how does it influence the behavior of the sample? Mesoscale heterostructures offer a unique possibility to study this interplay between microscopic and macroscopic behavior in a controlled environment.

Besides the fundamental interest, the questions asked have a direct relevance for applications. The most apparent field of use is in submillimeter photon detectors, which in many cases rely on the electrical response of a driven mesoscopic superconductor.

Chapter 2 introduces theoretical concepts which are relevant to the experiments and models appearing in this thesis. After a brief discussion of the electronic properties of metals and insulators, the emergence of ferromagnetic and superconducting ground states is reviewed. Subsequently we assess the implications of interfaces on the electronic properties of heterostructures. Non-equilibrium electron transport and energy relaxation are discussed for diffusive wires with ac and dc driving. Finally we look how the dielectric environment influences energy relaxation and how it interacts with electromagnetic fields.

Chapter 3 inquires into the relationship between a conceptual *model system* and its experimental realization. It briefly discusses the interplay between sample design, fabrication, and measurement on the one hand and the physical concepts introduced in *Chapter 2* on the other hand.

Chapter 4 and 5: we achieve a reduction in frequency noise (*Chapter 4*) and an increase of the quality factor (*Chapter 5*) of coplanar waveguide superconducting resonators. This result is obtained by engineering the dielectric environment in order to reduce the effect of two level systems. Therefore parts of the dielectric substrate are removed from regions with high electric fields.

Chapter 6: we further investigate the influence of the dielectric substrate on the properties of superconducting resonators. We demonstrate an increased quasiparticle recombination time in superconducting resonators on a thin SiN_x membrane, compared to identical resonators on a SiN_x/Si wafer. We use an array of solid state refrigerators, based on normal metal - superconductor tunnel junctions, to cool or heat the membrane. We show that the resonators on the membranes are extremely sensitive to small changes of the phonon temperature.

Chapter 7: we analyze how the performance of solid state refrigerators can be improved using highly transparent tunnel junctions. A theoretical analysis demonstrates the importance of the lateral uniformity of the tunnel barrier for the cooling power. Therefore we develop normal metal (Aluminum) superconductor (Niobium) tunnel junctions based on AlN tunnel barriers, which are more uniform compared to AlO_x .

Chapter 8: we study the influence of a non-equilibrium electron distribution on a superconducting nanowire between normal reservoirs. We demonstrate theoretically and experimentally the existence of two different superconducting states appearing, which result from an interplay between the non-equilibrium and the superconducting proximity effect. The different states are identified by using two probe measurements of the wire, and measurements of the local density of states with tunneling probes.

Chapter 9: we consider a superconducting nanowire between ferromagnetic reservoirs. The response of the wire to current-driving is consistent with results obtained with normal reservoirs. When the spin orientation of the ferromagnetic contacts is reversed by a parallel magnetic field, we observe a spin dependent resistance, associated with the conversion a spin polarized current into a supercurrent. We propose to use a ferromagnetic tunneling probe to verify if an induced magnetization is present in the driven superconducting wire.

References

- [1] R. B. Laughlin and D. Pines, *The Theory of Everything*, Proceedings of the National Academy of Sciences **97**, 28 (2000).
- [2] P. W. Anderson, *More is different*, Science **177**, 393 (1972).

- [3] R. Mills, *Gauge fields*, Am. J. of Phys. **57**, 492 (1989).
- [4] V. Ginzburg and L. Landau, *The Electromagnetic Equations of the Supraconductor*, Zh. Eksp. Teor. Fiz. **20**, 1064 (1950).
- [5] F. London and H. London, *The Electromagnetic Equations of the Supraconductor*, Proc. Roy. Soc. **A149**, 71 (1935).
- [6] W. Meissner and R. Ochsenfeld, *Ein neuer Effekt bei Eintritt der Supraleitfähigkeit*, Naturwissenschaften **21**, 787 (1933).
- [7] B. D. Josephson, *Possible new effects in superconductive tunnelling*, Physics Letters **1**, 251 (1962).

Chapter 2

Driven mesoscale heterostructures

2.1 Ordered electronic states

2.1.1 Electrons in a lattice

Solid state materials consist of relatively immobile, positively charged ions surrounded by a dense cloud of much more mobile, negatively charged electrons. In general the properties of the electrons depend on the specific position of each ion, but also on the interactions between the electrons. Given the extremely high electron density in most solids (more than a billion electrons per cubic micrometer), trying to obtain a rigorous description is optimistic at best.

A much simplified system can be obtained by assuming an infinite, periodic lattice. The electrons are treated as independent particles in a mean effective potential, which combines the contribution of the positively charged ionic cores with the average screening of the total electron cloud. The resulting electron states follow the periodic structure of the lattice and are spatially extended over the crystal. Therefore it is more useful to label each state by its wave vector k rather than by its position, as k reflects the periodicity of the electronic state. Each momentum state has a certain energy $E(k)$, which is shown in a band diagram (Fig. 2.1) for a metal (Al) and an insulator (AlN). The total density of states (dos) versus energy gives the number of available electron states in an infinitesimal energy range dE [1].

The electrons occupy the lowest energy levels available in order to minimize the total energy of the system. However, the Pauli exclusion principle[2] forbids that two electrons occupy the same state, forcing subsequent electrons to populate states with increasingly higher energies. The energy of the highest occupied electron level is denoted as the Fermi energy E_f . At zero temperature it forms a surface (the Fermi-surface) between completely filled and empty states. At finite temperature, thermal fluctuations can excite an electron from a filled state below E_f into an unoccupied state above E_f . The typical energy of these fluctuations is proportional to the temperature $\Delta E \approx 4k_B T$, with k_B the Boltzmann constant. As this energy is much smaller than E_f , it only affects the occupation of states in a small energy range around E_f . Most relevant interactions and driving fields, like electric or magnetic potentials, have a similarly small energy. For electrons which are deeply bound below the surface there are no empty states available. Therefore they do not participate in interactions, transport or thermal properties. They merely form a negatively charged background which compensates the positive charge of the nuclei. The behavior of the solid is hence dominated by the properties of the electrons near the Fermi-surface.

In metals, the valence electrons are weakly bound due to effective screening

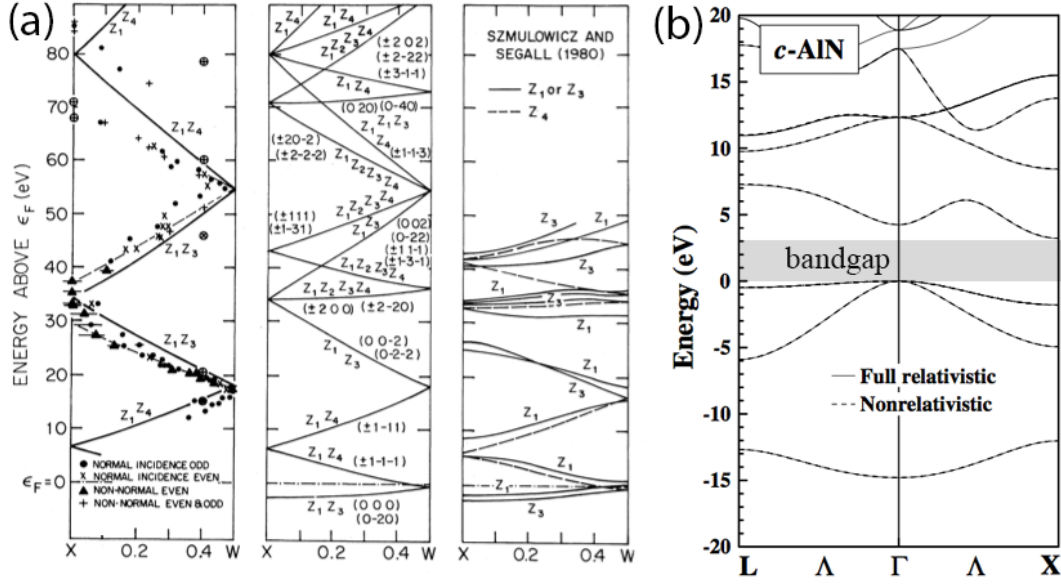


Figure 2.1: The band structures for (a) the metal Aluminum [3] and (b) the dielectric Aluminum Nitride [4]. (a) The metal has a continuum of electron states; for every energy E (vertical axis) there is an electronic state a_k with $E(k)$. Notice the close resemblance between the experimental data (first panel) and a free electron model (second panel) despite the oversimplifications of the latter. (b) For the dielectric, there is a region of energies without electron states, called a bandgap. To carry a current, electrons from filled states below the gap have to be excited to states above the gap.

of the nucleus. The electron wave functions of neighboring atoms show a large overlap and combine into a broad band of plane waves without much spatial structure. The Fermi-surface lies within a continuum of states (Fig. 2.1a), which means electrons can be easily excited, even at small energies. In the presence of an electric field, electrons are gradually accelerated until they collide with impurities or phonons (lattice vibrations). A net electric current flows because the electrons are excited into states with a high momentum in the direction of the field. It is thus the presence of available states with a relative low energy which allows metals to conduct electric current.

In dielectrics, electrons are often more strongly bound to the nuclei, with a wave function resembling the one of localized electrons in an isolated atom. This results in a band structure with narrow bands, separated by an energy gap E_g without any electronic states (Fig. 2.1b). If the Fermi level lies in between two energy bands, the band diagram consists of fully filled bands below E_f and completely empty bands above E_f . It is impossible to excite electrons into a

higher momentum state, unless a minimal energy equal to the band gap E_g is provided. The electrons can therefore not accelerate and the material can not support a current; it behaves as an insulator.

Treating electrons in a solid as independent or even free particles works surprisingly well, given the gross oversimplifications made. Part of the success can be explained by the effective electronic screening by the electron cloud, which makes it possible to describe the effects of the Coulomb interaction on the electronic wave functions using an effective potential. In addition it can be shown that an interacting electron system can be mapped one to one to a system of independent quasiparticles, as long as it can be described as a perturbation of the Fermi sea. These quasiparticles represent many electrons and their interactions, but have the same charge as electrons [5].

The presence of (even weak) electron-electron interactions can lead to a radically different ground state. Below we discuss ferromagnetism and superconductivity, two examples of ordered states which are relevant for this thesis. In both cases, the energy gain associated with the electron interactions leads to the spontaneous formation of long range order. For a ferromagnet, spin-spin interactions lead to a spontaneous magnetization \mathbf{M} . At finite temperatures the strength of \mathbf{M} decreases due to thermal excitations, until all magnetic ordering disappears at the Curie temperature T_{Cu} (Fig. 2.2a). Due to the strong interactions, the physics of ferromagnets can not be captured by a mean field theory of free electrons. For a superconductor, an attractive interaction between electrons leads to the formation of bound electron pairs (Cooper pairs [6]). The Cooper pairs form one coherent macroscopic wave function $|\Delta|e^{i\phi}$ with a well-defined phase ϕ . The collective nature of this state implies it can not be treated as a perturbation of the Fermi sea. The magnitude $|\Delta|$ is proportional to the density of Cooper pairs, while the value ϕ breaks symmetry in phase-space. For increasing temperature, thermal fluctuations break Cooper pairs until the superconducting order disappears at the critical temperature T_c (Fig. 2.3a).

2.1.2 Ferromagnetism

Besides an electronic charge, electrons have spin. It represents a discrete amount of angular momentum with a small magnetic moment associated with it, pointing up (\uparrow) or down (\downarrow). Due to this magnetic moment, the spins tend to align with an external magnetic field, thus enhancing it. In addition, strong spin-spin interactions exist between electrons. This interaction stems from a combination of the Pauli exclusion principle and electrostatic forces, rather than interaction between their magnetic moments. In the presence of such an effective spin-spin

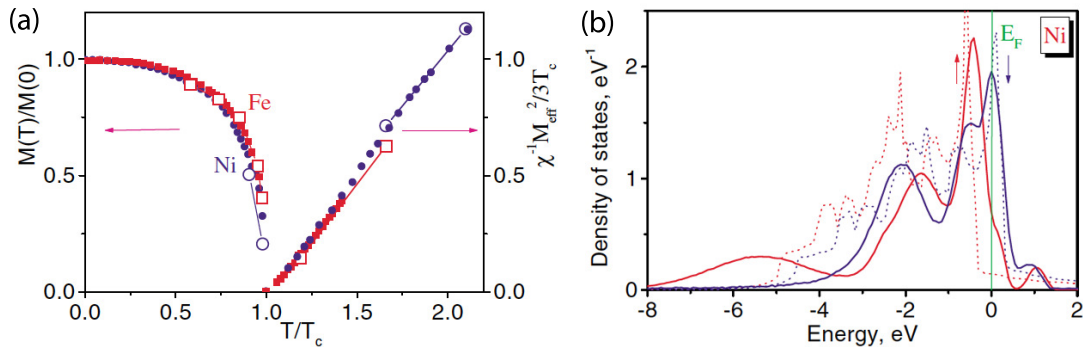


Figure 2.2: (a) The dependence of the spontaneous magnetization \mathbf{M} and the inverse susceptibility on temperature for Ni and Fe. The strong electron-electron interactions require a physical model which goes beyond a mean field theory. (b) The spin-dependent density of states of Ni at zero temperature (dashed lines) and at $0.9 T_{Cu}$. Because of the coupling between the electronic ground state and quasiparticle excitations, the density of states explicitly on the temperature [7].

interaction, the electronic spins can spontaneously align to reduce the energy of the system. Their individual magnetic moments combine into a macroscopic magnetization \mathbf{M} which breaks the rotational symmetry; the material reduces its energy at the cost of losing a degree of freedom [8].

At zero temperature all spins are aligned and the order is maximal. For increasing temperatures, single particle excitations and spin fluctuations randomize the spin orientations more and more, thus increasing the entropy of the system [9]. At the Curie temperature T_{Cu} no net magnetization is left. The thermal energy equals the condensation energy and the order disappears. The Curie temperature is therefore a measure for reduction in energy and the strength of the spin interactions.

For Ni, Co, and Fe the magnetic properties are due to spin exchange between isolated d -shell atoms. A net magnetization \mathbf{M} induces a Zeeman-splitting between the energy levels of spin-up and spin-down electrons (Fig. 2.2b). Although the associated energy shift between their respective density of states increases the kinetic energy of the system, it is outweighed by the gain in exchange energy. This leads not only to different density of states and Fermi-velocities $v_{f,\uparrow\downarrow}$ for the isolated electrons of the d -band, but also to spin-dependent scattering of the delocalized s -band electrons which dominate the conduction. A realistic framework should explicitly include electron interactions, and hence goes beyond a free electron picture [7].

2.1.3 Superconductivity

In a superconductor, the presence of an attractive electron-electron interaction renders the Fermi sea unstable against the formation of bound electron states [6]. Electrons of opposite momentum and spin form so-called Cooper pairs, which all condense into a coherent, macroscopically occupied state $|\Delta|e^{i\phi}$. The amplitude of the complex order parameter Δ is proportional to the number N of Cooper pairs in the condensate, while the well-defined phase ϕ reflects their coherence. Due to the uncertainty principle of Heisenberg $\Delta N \Delta\phi > 1$, the number of Cooper pairs fluctuates around their average number N [12].

The attraction between different electrons originates from the Coulomb interaction, mediated by phonons (lattice vibrations). The electronic interaction of a first electron with the inert lattice exerts a retarded, attractive force on a second electron. To realize a maximum energy reduction through this attractive interaction, a rearrangement of the electrons in momentum space takes place, at the cost of an increase in kinetic energy. This leads to a superconducting ground state which is a coherent superposition of states with different numbers of pairs, as first described by Bardeen, Cooper and Schieffer (BCS) [13]:

$$|\psi_{BCS}\rangle = \prod_k (u_k + v_k c_{k\uparrow}^* c_{-k\downarrow}^*) |\phi_0\rangle. \quad (2.1)$$

A certain momentum state k has a probability v_k^2 to be occupied by a pair of electrons $c_{k\uparrow}^* c_{-k\downarrow}^*$, while the probability for the state to be empty is given by $u_k^2 = 1 - v_k^2$. The condensation energy is proportional to $\sum V_{kl} u_k v_k^* u_l^* v_l$ and explicitly requires that states are partially occupied and have coherent phases, otherwise $\Delta = 0$. Therefore, *time-reversed* electron and hole states in a region of Δ around the Fermi level are mixed. The pairs with momenta in this region contribute most to the condensation energy.

The nature of the BCS ground state has far-reaching consequences for the excitations of a superconductor. As the electrons are bound in a coherent pair state, it is impossible to excite a single electron without affecting the complete condensate. The minimal energy to create an excitation from the superconducting ground state equals the loss in condensation energy associated with the broken Cooper pair, Δ . This leads to a spectral energy gap in the quasiparticle density of states (Fig. 2.3b). However, superconducting order (proportional to the order parameter Δ) does not necessarily induce a spectral energy gap, for example in the presence of magnetic impurities which break time-reversal symmetry.

For increasing temperatures more and more Cooper pairs are broken and the condensation energy decreases. As the critical temperature T_c of the superconductor is reached, all coherence is lost and the electrons behave independently

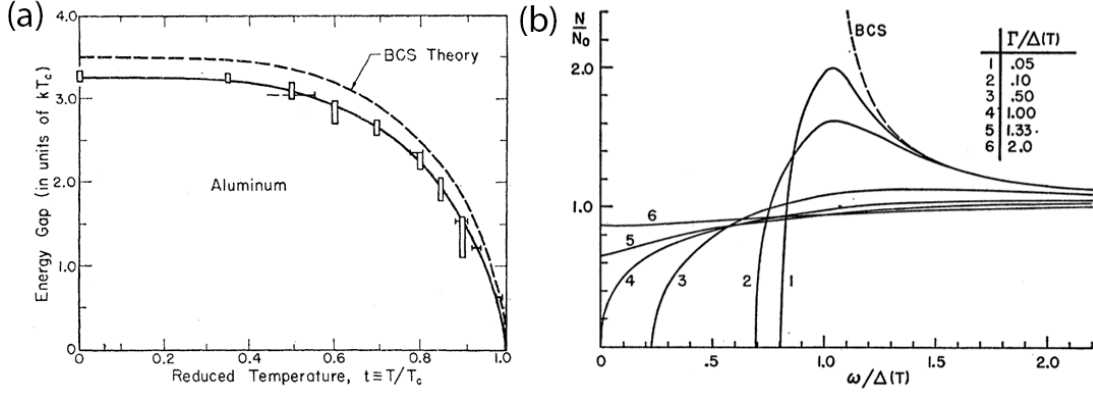


Figure 2.3: The temperature dependence of the spectral energy gap in a superconductor, measured by photon absorption [10]. For increasing temperatures Cooper pairs are broken, reducing the strength of the superconducting order. (b) The density of states in a superconductor [11]. The dashed line represents a bulk BCS superconductor and has no states below the gap; the spectral gap and the order parameter are identical. However, if time reversal symmetry is broken (in this case by paramagnetic impurities), subgap states are formed. Although spectroscopically gapless, the superconducting order is still present.

with random phases (Fig. 2.3). The effect of breaking Cooper pairs in the region of around the Fermi level is much stronger as they contribute more strongly to the formation of the superconducting order. In addition, the ground state as given by Eq (2.1) explicitly mixes electron and hole states in a region of Δ around the Fermi level. This means that the excitations at those momenta also behave as a mixture of an electron and a hole state and have an effective charge in between a full negative (electron) charge $-e$ and a positive (hole) charge e .

2.2 Interfaces

A heterostructure by definition consists of different materials, which necessarily creates interfaces. It is tempting to think of such an interface as a two-dimensional surface which is merely a boundary between two bulk materials, each with well-defined electronic properties. The influence of the interface is usually negligible in comparison with the bulk and is absorbed in some phenomenological properties, localized at the separating boundary, such as an interface resistance.

For mesoscopic structures however, this intuitively compelling picture breaks down. As the structures get smaller the surface to volume ratio becomes increasingly bigger, and the influence of the interfaces and surfaces can dominate the

behavior of the system. Furthermore, the electronic properties do not change abruptly at the interface, but gradually change over a distance, set by the relevant potentials on each side of the interface. These potentials themselves depend on the electronic properties. As the physical length of the sample becomes comparable to these conversion lengths, it is clear that it hardly makes sense to artificially separate a bulk region from the interface.

A way to cope with the non homogeneous character is to model the structures at the microscopic level. The electronic properties become strongly position-dependent, over length scales which are set by the physical processes involved. The potentials associated with these processes are obtained in a self-consistent way, together with the electronic properties.

2.2.1 Length scales

The interactions between an electron and its environment determine its behavior. Such interactions consist of elastic scattering on impurities and boundaries, and inelastic electron scattering on other electrons, phonons, or photons. In addition, the electrons experience the presence of self-consistent fields like a magnetization \mathbf{M} or a superconducting potential Δ . Each of these processes acts on different properties of the electron system, over a specific length scale.

In the diffusive metals used in this thesis, the most prominent scattering mechanism is elastic scattering on impurities. The density of impurities is relatively high, leading to an elastic mean free path l_{el} of the order of a few tens of nanometers. As l_{el} is still considerably larger than the Fermi wavelength of the electrons $\lambda_F = 2\pi/k_F$, the electron motion can be described semi-classically as a random walk between impurities [14]. The average distance $L = \sqrt{D\tau}$ an electron travels in a time τ , is set by the Fermi-velocity and the mean free path l_{el} which determine the diffusion constant $D = v_f l_{el}/3$. As the dimensions of the structures become smaller, scattering from surfaces and interfaces gains importance and can put an upper limit to the mean free path. In that case, the exact nature of the boundary determines whether the electronic momentum is conserved. A rough boundary on the scale of λ_F is more likely to randomize the momentum (diffusive scattering) than a smooth one (specular scattering). Inelastic interactions with electrons, phonons or photons mainly affect the excitation spectrum of the electrons, which will be treated in Section 2.3. This section only considers the influence on equilibrium properties such as the density of states and coherence. Self organized potentials as a magnetization \mathbf{M} or a superconducting order Δ have relatively small energies, and the associated length scales are considerably larger than l_{el} .

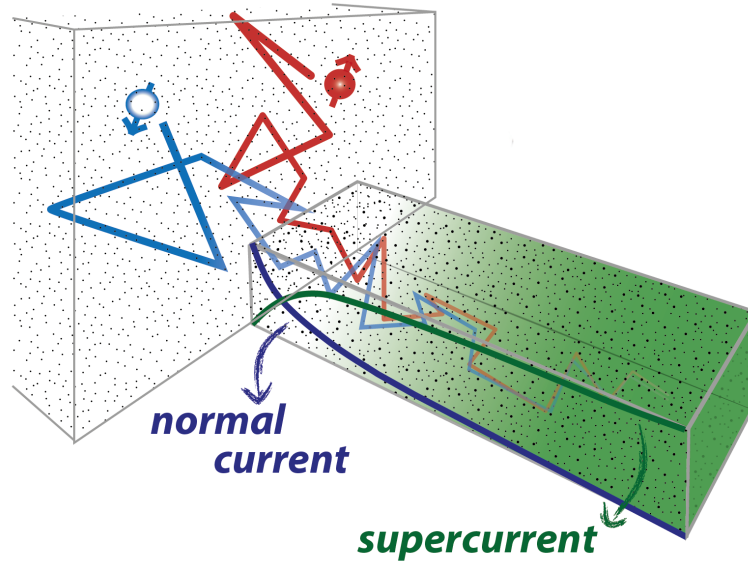


Figure 2.4: A schematic representation of the conversion of normal electrons into Cooper pairs at a normal metal - superconductor boundary. An incident normal electron (red) is retro-reflected as a phase coherent hole (blue). At the same time one Cooper pair is added to the condensate. This conversion process occurs due to the presence of the superconducting order parameter and takes place over roughly one coherence length ξ .

Consider a boundary between a normal metal and a superconductor (Fig. 2.4). Deep in the normal metal the electrons behave totally uncorrelated without any energy (spectral) dependence. Inside the superconductor, on the other hand, all the electrons are nicely ordered as well behaved cooper pairs, phase coherent, and not disturbed by any perturbation smaller than the gap. In the region near the interface it is clear the electrons should be a mixture of both. An important question is what the spatial extent of such an interface is. The superconducting wave function is not confined to the right hand side of the interface, but will leak into the normal metal. This superconducting proximity effect can be understood by looking at a normal wave packet impinging on the NS boundary. In the case of a perfect transparent interface, it will be converted into a Cooper pair inside the superconductor due to the presence of the superconducting order parameter Δ . The second electron of the pair, with opposite spin and momentum, originates from a hole which is retro-reflected into the normal metal. Hence, the reflected hole has exact opposite properties of the impinging electron and will retrace its trajectory [15]. Over a certain length scale this process establishes phase coherence between time reversed states in the normal metal. At the same time,

over some distance in the superconductor, there is a penetration of incoherent electrons until they combine into Cooper pairs.

The characteristic distances for this process can be estimated to first order by considering an impinging electron with an energy ϵ and a reflected hole with energy $-\epsilon$. Through the dispersion relation for free electrons $E = \hbar^2 k^2 / 2m$, this leads to a slight shift between the respective wave vector of the electron and the hole, given to first order by $\hbar^2 k_f \delta k / 2m \approx \epsilon$. As the hole retraces the path of the electron, this small shift in wave vector will generate a phase difference of $\delta k dl$. As the electron-hole pair diffuses in the normal metal, they gradually dephase until they are no longer correlated after a typical distance of $\xi_N = \sqrt{\hbar D / \epsilon}$. This coherence length ξ_N not only depends on the properties of the normal metal, but also on the energy of the incoming electron (at $\epsilon = 0$ it becomes infinite). In the superconductor the interaction with the pair potential mixes the electron with the hole. This is a process which takes place over a distance set by the superconducting gap $\xi_S = \sqrt{\hbar D / \pi \Delta}$, the superconducting coherence length. The effective size of an interface is hence set by the energy scale of the physical processes involved. If the size of the sample is small compared to this length scale, the interface affects the complete structure. The previous discussion only considered the influence of the superconducting order parameter on the electronic wave functions. However, the coherence of the electrons also influences the superconducting potential and the two have to be calculated self-consistently.

2.2.2 Microscopic description

The presence of interfaces implies non-homogeneous electronic wave functions, but more generally also the potentials and interactions become position dependent. A convenient framework to model such an interacting many-body system is the Green function theory. These Green functions reflect the propagations of electrons in space and time. A Green function $G_{\alpha,\beta}(r_2, t_2, r_1, t_1) = \langle \psi_\beta(r_2, t_2) \psi_\alpha^\dagger(r_1, t_1) \rangle$ is a complex number, representing the correlation between an electron state ψ_α created at a time t_1 at a position r_1 and an electron state ψ_β at a position r_2 and a time t_2 (inset Fig. 2.5a). The quantum numbers α, β reflect electronic properties other than space and time, for example the electron spin.

The short wavelength λ_F of electrons near the Fermi level means that G oscillates rapidly as a function of the position difference $r = r_2 - r_1$. However, as indicated in the previous Section, the main properties of interest occur at much lower energy scales and have an accordingly slow spatial dependence (Fig. 2.5a).

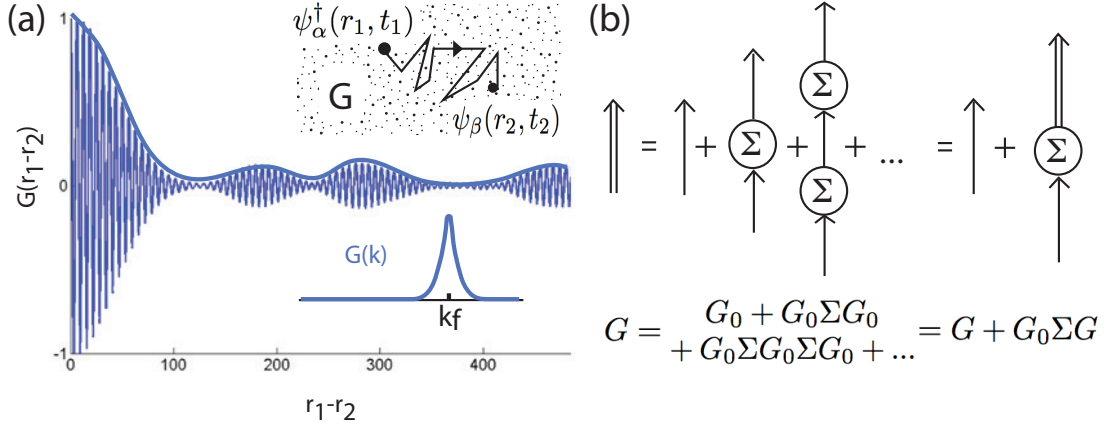


Figure 2.5: The evolution in time and space of a quasiparticle is given by a propagator G , which represents the probability that a particle $\psi^\dagger(r_1, t_1)$ created at time t_1 at position r_1 , is to be found at a time t_2 at a position r_2 : $\psi(r_2, t_2)$. (a) The propagator has a fast-varying component (proportional to E_f) due to the wave nature of the electron and a slow-varying component corresponding to low-energy potentials such as the superconducting order parameter. In momentum space this corresponds to a sharply peaked distribution around the Fermi momentum k_f (inset). In the quasiclassical approximation only the slow varying envelope (thick blue line) is taken into account. (b) Interactions are included by *dressing* the *bare* propagator G_0 with an infinite number of interactions, represented by the self-energy Σ . The self-energy itself depends on the properties of G , the available interactions, and potentials.

In momentum space the Green function is a sharply peaked function around k_F (inset Fig. 2.5a), and can be approximated with a δ function [16, 17]. The variations due to the slow spatial components is included through the dependence of G on the mean position $R = \frac{1}{2}(r_1 + r_2)$. A second approximation arises from the fact that the short elastic mean free path in dirty metals effectively randomizes the direction of the electronic momentum [18]. The Green functions $G(R, t_1, t_2) = G(R, k_f, t_1, t_2)$ are isotropic and do not explicitly depend on the electronic momentum, reducing the complexity of the equations considerably. The evaluation of G at k_F means that effects due to quantum interference are ignored, it is referred to as the quasi-classical approximation.

Interactions and many-body effects are included as a perturbation and *dress* the (unperturbed) *bare* propagator G_0 . The dressed propagator G represents the evolution of an interacting quasiparticle and is given by a summation over the bare propagator G_0 , which encounters an arbitrary number of interactions (Fig. 2.5b). This schematic can be condensed into $G = G_0 \Sigma G$, the Dyson equation. The

self-energy $\Sigma = \Sigma_{el-el} + \Sigma_{phonons} + \Sigma_{imp} + \dots$ represents the combined effect of all interactions and depends on the electronic trajectories, given by G . Hence G and Σ have to be evaluated simultaneously.

Knowledge of the Green function G contains spectral information (e.g. the local density of states) and allows to calculate the influence of interactions on the behavior of the fermi sea, or individual levels. Although this covers correlations between normal electrons, for superconductive electrons, also correlations between electrons and holes have to be taken into account. The Fermi sea is not a valid starting point for a perturbative theory and it is necessary to introduce a radically different ground state like the *BCS* ground state for bulk superconductors. Therefore an extra propagator is introduced, the anomalous Green function given by $F = \langle \psi_{\beta}^{\dagger}(r_2, t_2) \psi_{\alpha}^{\dagger}(r_1, t_1) \rangle$, which describes the creation (or annihilation) of a Cooper pair [19, 20].

2.2.3 Boundary conditions

The physical size of an interface between two materials is of the order of one or a few atomic layers. This means that material properties, potentials, and electronic wave functions change rapidly over length scales smaller than or comparable to the Fermi wavelength λ_F . Given the approximations outlined above, the quasi-classical theory is unable to describe the electronic properties in the direct vicinity of the interface. To overcome this problem the original Green functions with the full spatial dependence are used to generate appropriate boundary conditions, which match the quasi-classical functions on both sides of the interface [22, 23, 21].

Interfaces which are realized experimentally have in general complex properties, which are in addition difficult to measure. Obtaining a realistic model which captures the details of the electron wave functions near the interface is rather impossible, except in some limited systems. One approach to obtain a workable model is a phenomenological representation with a scattering matrix, which relates incoming and outgoing wave amplitudes on both sides of the interface (Fig. 2.6). The amplitude for transmission of an electron state ψ_{α}^L on the left side of the interface into a state ψ_{β}^R on the right side is given by $t_{\alpha,\beta}$, while the amplitudes of the reflected waves are given by $r_{\alpha,\beta}$. As the number of electrons is conserved the probability for transmission or reflection equals one $\sum |t_{\alpha,\beta}|^2 + |r_{\alpha,\beta}|^2 = 1$. The dependences of the transmission values on the energy, momentum or spin of the impinging electrons are in most cases either ignored or introduced *ad hoc*.

For a number of simplified model systems, the transmission values can be approximated theoretically. An important assumption concerns whether energy

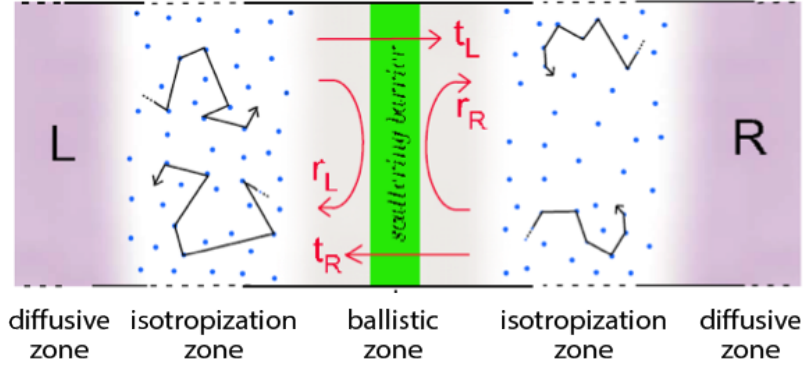


Figure 2.6: The interface between two diffusive metals can be modeled as a scattering region, characterized by a transmission (t) and reflection (r) coefficients which match the microscopic Green functions on both sides of the boundary [21].

and momentum are conserved upon transmission through the interface. For a clean interface the scattering matrix t is expected to be elastic (energy conservation) and specular (momentum conservation). Furthermore electronic properties like λ_F or the density of states are assumed to be unaffected by the presence of the interface. Under these assumptions the transparency is determined by the mismatch in Fermi wave vectors and has values which are close to unity. Tunnel barriers are a limiting case of an interface with transmission values close to zero. Ideally they consist of a few atomic layers of insulating material, with a certain band gap E_g . Electrons impinging on this interface have an evanescent tail penetrating the insulator, which gives them a small but finite probability to tunnel to the other side of the barrier. In a Werner-Kramer-Brillouin approximation, this probability is exponentially dependent on the barrier height $e\phi$ and thickness t [24]. The exponential dependence of the transmission and the large number of variables make a comparison with experiments difficult. In practice it is absorbed in an effective tunnel barrier resistance R_n .

2.3 Driven electrons

The electronic properties of a structure are investigated by looking at its response to current-driving. The linear response is determined by the resistance of the structure, which for a normal metal is a backscattering resistance. For a heterostructure, the resistance not only reflects the properties of the different materials, but also the influence of conversion processes near the interfaces. For strong bias, the electrons are driven out of equilibrium. If the structures are short compared to typical energy relaxation lengths, the non-equilibrium can no

longer be characterized by an effective temperature. This non-equilibrium in the normal state is ‘hidden’ in the sense that the resistance does not depend on the energy distribution of the electrons. For a driven superconductor however, the electronic properties depend explicitly on the distribution of quasiparticles over the energies. The response becomes a nonlinear function of the driving, reflecting the interaction between non-equilibrium quasiparticles and the superconducting condensate.

2.3.1 Diffusive transport

In normal metals, the resistance is dominated by the backscattering of electrons. An applied electric field \mathbf{E} accelerates electrons until their momentum is randomized by scattering on impurities, phonons or boundaries. They acquire an average drift velocity \mathbf{v}_d in the direction of the applied field, which is proportional to the average time they spend between two scattering events. The associated current is given by the *total number of electrons*, all moving at an average drift velocity $\mathbf{j} = en_s \mathbf{v}_d$.

Alternatively, the electric field can be seen as a gradient in the electro-chemical potential of the electrons $\nabla\mu = e\mathbf{E}$. This causes a changing electron density near the Fermi level and a net flow of electrons. In this case the total current is carried *by electrons near the Fermi level only*. The current is given by Fick’s law $\mathbf{j} = -eDN_0\nabla\mu$, where N_0 is the electron density at the Fermi level and the diffusion constant $D = v_f l_{el}/3$ is a measure for the mobility of the electrons. Through $\mathbf{j} = \sigma\mathbf{E}$, the Einstein relation between the conductivity and the diffusion constant is obtained, $\sigma = e^2 N_0 D$ [25].

A ferromagnet is characterized by a spin-dependent density of states $N_{0,\uparrow,\downarrow}$, conductivity $\sigma_{\uparrow,\downarrow}$, and diffusion constant $D_{\uparrow,\downarrow}$. The transport can be modeled by assuming two independent spin-channels, with a spin-dependent chemical potential $\mu_{\uparrow,\downarrow}$ and quasiparticle current $j_{\uparrow,\downarrow}$ [26]:

$$j_{\uparrow,\downarrow} = \sigma_{\uparrow,\downarrow} \nabla\mu_{\uparrow,\downarrow}, \quad \sigma_{\uparrow,\downarrow} = e^2 N_{0,\uparrow,\downarrow} D_{\uparrow,\downarrow}. \quad (2.2)$$

A difference in chemical potential between spin-up and spin-down is relaxed by spin flip scattering over a length scale λ_{sf} . The electrons not only carry a charge current, but also a net spin current given by $j_{spin} = j_{\uparrow} - j_{\downarrow} = \frac{1}{e}(\sigma_{\uparrow} - \sigma_{\downarrow})\mathbf{E}$. The spin-polarization of the current $\alpha_F = \frac{j_{\uparrow} - j_{\downarrow}}{j_{\uparrow} + j_{\downarrow}}$ can take on any value between -1 and 1 . In a bulk ferromagnet, the gradients $\nabla\mu_{\uparrow}$ and $\nabla\mu_{\downarrow}$ are equal, leading to a spin polarization of $\alpha_F = \frac{\sigma_{\uparrow} - \sigma_{\downarrow}}{\sigma_{\uparrow} + \sigma_{\downarrow}}$.

In a superconductor, a dissipationless supercurrent is proportional to a gradient in the phase of the superconducting order parameter, rather than a gradient

in particle density. Although the Cooper pairs can carry a charge current without any resistance, any energy or charge current is effectively blocked. The reason for this is that a singlet Cooper pair carries no net spin as it consists of a spin-up and a spin-down electron and no net energy as it is located at the Fermi level. The only way a superconductor can support an energy or spin current is by quasiparticles. The transport equations and the quasiparticle distribution are disentangled into a part connected to charge transport (in which the Cooper pairs do participate) and a part connected to energy or transport (in which they do not directly participate). In addition, the presence of a charge, energy or spin non-equilibrium in the quasiparticle spectrum will affect the superconducting ground state in different ways. In the following sections and *Chapters 8* and *9* we address this problem in more detail.

2.3.2 Current conversion resistance

Backscattering of electrons in normal, bulk materials gives rise to an electrical resistance which only depends on the normal resistivity and the geometry of the structure. The presence of interfaces between different materials in heterostructures introduces an extra resistance by two different mechanisms. The finite transparency of the interface results in backscattering of electrons similar to the normal resistance. Furthermore, the carriers of the current on both sides of the interface are in general not the same, which gives rise to a current conversion resistance. The magnitude of this resistance is proportional to the length scale of the conversion process and the resistivity of the material where the conversion process takes place. The location of this resistance is not uniquely defined. It can be thought of as a drop in the Fermi level at the interface, but a picture in which it extends over the length of the conversion is more appropriate from a physical point of view.

Fig. 2.7 represents a clean contact between a ferromagnet carrying a spin-polarized normal current and a superconductor where the current is carried by spin-neutral (singlet) Cooper pairs. On the ferromagnetic side the spin-polarized current introduces an overabundance of one type of spin carriers (spin up in Fig. 2.7), because each electron needs to combine with a spin down electron in order to form a Cooper pair. The density of spin-up carriers near the interfaces increases until spin relaxation exactly balances the net accumulation due to the spin-polarized current. Spin relaxation occurs mainly in the ferromagnet over a distance $\lambda_{sf} = \sqrt{D\tau_{sf}}$, because the ferromagnet has a much higher spin-flip relaxation rate than the superconductor. The spin accumulation causes a split in the Fermi levels for spin-up and spin-down in the ferromagnet, and a jump in the

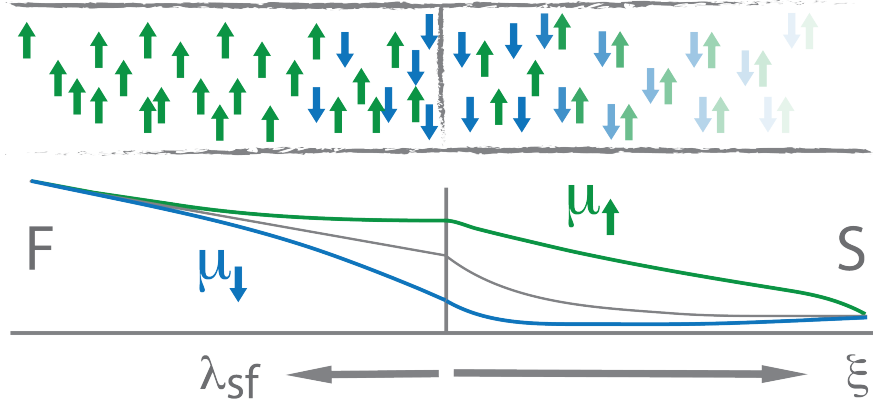


Figure 2.7: The conversion of a spin-polarized current carried by normal electrons into a supercurrent carried by the superconducting condensate leads to a current conversion resistance. Spin accumulation in the ferromagnet relaxes over a length scale λ_{sf} which is inversely proportional to the magnetization \mathbf{M} . Analogously charge accumulation in the superconductor decays over a length scale ξ set by the superconducting order parameter.

average Fermi level at the interface appears as an interface resistance. Intuitively the current near the interface is forced to use the more resistive spin-down channel over a distance comparable to λ_{sf} , because only a spin-neutral current can penetrate into the superconductor. Similarly, normal electrons which are injected from the ferromagnet into the superconductor are converted into Cooper pairs over a distance of roughly a coherence length $\xi = \sqrt{(\hbar D/2\Delta)}$, set by the superconducting order parameter Δ . In this region close to the interface, normal electrons accumulate which leads to the presence of a net charge in the quasiparticle spectrum. A dc electric field associated with this charge mode penetrates the superconductor, leading to a resistance $R \sim \xi\rho$. Hence, two conversion processes take place near the interface: (1) the conversion of a spin-polarized current into a spin-neutral current on the ferromagnetic side, (2) the conversion of a normal current into a supercurrent on the superconducting side. Each of the conversion processes is associated with the accumulation of the quantity which needs to be converted (respectively spin and charge), leading to a resistance proportional to the conversion length and the material specific resistivity. The linear response to current-transport is an accurate probe of the microscopic electronic properties near the interface of such a heterostructure.

2.3.3 Energy absorption, relaxation and non-equilibrium

In thermal equilibrium, only electrons in an energy range of roughly $4k_B T$ around the Fermi energy are thermally excited. Although this is a random process, it is possible to quantify the average distribution of the electrons over the different energy levels. The mean occupation $f(\epsilon, T)$ of a single electronic state is given by a Fermi-Dirac distribution $f_{FD}(\epsilon, T) = 1/(\exp(\epsilon/k_B T) + 1)$. It depends only on the relative energy with respect to the Fermi energy $\epsilon = E - E_f$ and the temperature T of the system.

In a driven structure, energy is absorbed by the electron system. Quasiparticle excitations are created and existing quasiparticles gain energy. This results in a non-equilibrium energy distribution $f(\epsilon)$, which differs from the equilibrium Fermi-Dirac distribution. For relatively weak driving the distribution function is quasi-thermal and can be characterized by a local, enhanced temperature T^* . In general however, $f(\epsilon)$ can have an arbitrary shape, and the only way to describe the non-equilibrium is to take into account the full energy dependence. This situation is often encountered in mesoscale structures, as their size is small compared to the different energy relaxation lengths. The energy relaxation occurs through inelastic electron-electron and electron-phonon scattering. Electron-electron interactions allow hot quasiparticles to redistribute their energy amongst the electron bath. In this process total energy contained within the electronic system stays constant. Inelastic interactions with phonons or photons provide a way to lose (or gain) net energy.

Hot quasiparticles in a dc-driven wire

Fig. 2.8 shows a diffusive normal metal wire between two normal reservoirs, biased at respectively $\pm eV/2$. The contact pads act as equilibrium reservoirs at the bath temperature T_{bath} , from which electrons with a well-defined energy distribution are injected into the wire. The average time it takes for an electron to diffuse through the wire, $\tau_D = L^2/D$, is determined by the length L of the wire and its diffusion constant D . For short enough wires, the diffusion time can be small in comparison to electron-electron or electron-phonon interaction times, $\tau_D \ll \tau_{ee}, \tau_{eph}$. The absence of effective relaxation leads to a position-dependent energy distribution, which is a linear interpolation of the electronic distribution in the reservoirs, $f(x, \epsilon) = (x/L)f_L + (1 - x/L)f_R$. The two-step distribution with excitations extending over an energy range between $-eV/2$ and $eV/2$ differs significantly from a thermal Fermi-Dirac. The only way temperature enters the problem is through the energy distribution of the reservoirs, set by T_{bath} .

If inelastic electron-electron scattering is strong $\tau_{ee} \ll \tau_D \ll \tau_{eph}$, high energy

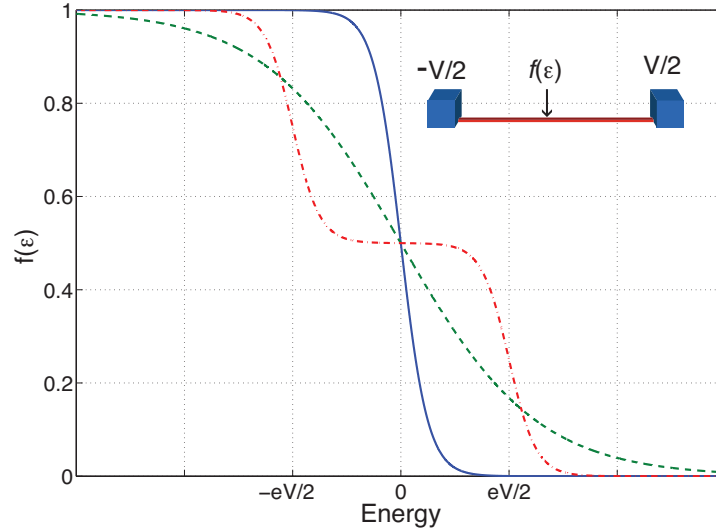


Figure 2.8: The electronic energy distribution $f(E)$ in a mesoscopic wire which is biased with a voltage eV . In the case of strong electron-phonon relaxation, the electrons are in thermal equilibrium (blue). If only inelastic electron-electron scattering is present, the electrons adopt a quasi-equilibrium distribution with a locally elevated temperature (green). In the absence of interactions, the distribution function is given by a two-step distribution function which is an interpolation of the electron distribution of the reservoirs (red).

electrons redistribute their energy. The electron system reaches a local equilibrium, characterized by a Fermi-Dirac distribution with a position-dependent temperature $f(x, \epsilon) = f_{FD}(T(x))$. The effective temperature profile is parabolic, the highest temperatures occur in the center of the wire while the ends of the wire stay at the bath temperature due to the presence of the equilibrium reservoirs. The quasiparticle excitations extend over an energy range set by the local temperature $\Delta E \approx 4kT(x)$. Electronic excitations can acquire energies beyond eV , in contrast to the case without inelastic scattering. In the presence of strong electron-phonon scattering $\tau_{eph} \ll \tau_D$, the electrons can relax their energy to the phonon bath. The electrons acquire a Fermi-Dirac distribution at the bath temperature T_{bath} . Experimentally these distribution functions can be observed with local tunneling probes [27] or by measuring shot noise [28, 29, 30, 31].

Photon absorption in an ac-driven wire

In the presence of an alternating electric field $V \cos(\omega t)$, energy is absorbed in quanta set by the photon energy $\hbar\omega$, similar to photon assisted tunneling [32] through superconducting junctions. The electrons adopt a staircase distribution

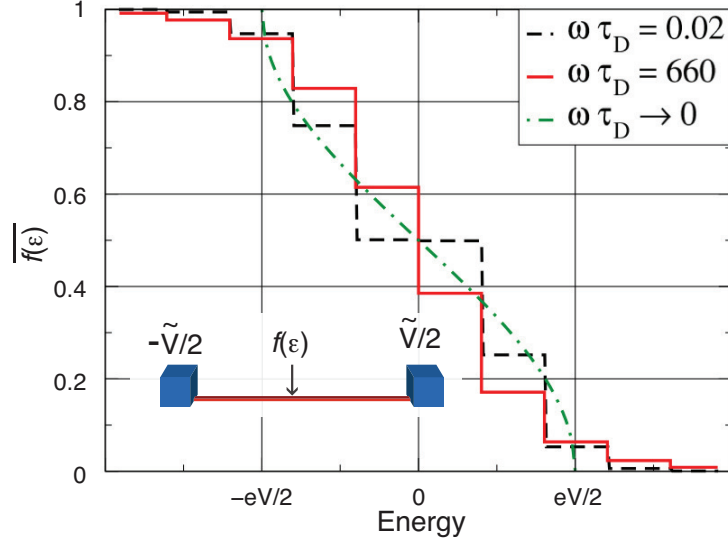


Figure 2.9: The time-averaged electron distribution in an ac-driven mesoscopic wire. For slow fields, the electrons follow the electric field instantaneously and have a time-dependent distribution function similar to the dc case (dashed green line). For higher frequencies, photon absorption leads to a staircase distribution with energy steps which match the photon energy $\hbar\omega$. In this case the electrons can reach excitation energies beyond the bias voltage [33].

function, consisting of several plateaus with a width of $\hbar\omega$ and extending over an energy range roughly set by the bias voltage eV . These plateaus disappear due to thermal excitations at high temperatures ($k_B T > \hbar\omega$) or due to rounding by strong inelastic scattering ($\tau_{ee}, \tau_{eph} \gg \frac{eV}{\hbar\omega}$).

The irradiation makes the system explicitly dependent on the time. An approach using a time-dependent Boltzmann equation is valid, if the time scale associated with the photon-field ($\tau = 2\pi\omega^{-1}$) is smaller than the elastic scattering time τ_{el} , and the RC -times associated with the sample. However, the definition of an energy distribution function in the presence of a time-dependent potential is not trivial. A scalar electric potential $V \cos(\omega t)$ modulates the energy levels of the quasiparticles: $\tilde{\epsilon} = \epsilon + \cos(\omega t)$. Therefore, even an equilibrium energy distribution $f_{FD}(\tilde{\epsilon}, T_{bath})$ appears to be time-dependent, with frequency components at $\epsilon + n\hbar\omega$. It is more convenient to use a different gauge, in which the electric field is represented as a vector-potential $A = \frac{eV}{c\omega} \sin(\omega t)$. The only time dependence left in $f(x, \epsilon, t)$ is the *real* dependence of the occupation number as the field strength is varied.

If the response time of the wire is fast compared to the applied field $\omega\tau_D \ll 1$, the electronic energy distribution follows the field variations adiabatically.

Although the distribution function is very similar to the one in the dc case, energy is absorbed in quanta of $\hbar\omega$. Quasiparticles can be excited to energies beyond the applied voltage $n\hbar\omega > eV$. Only in the limit $eV \gg \hbar\omega$, $f(x, \epsilon, t)$ is equal to the dc distribution function which instantaneously follows the oscillating voltage $V(t)$. Fig. 2.9 shows the time-averaged distribution function $\overline{f(x, \epsilon, t)}$. For fast fields $\omega\tau \gg 1$, the electron system is unable to follow the field oscillations and the energy distribution function takes on an average value.

The effect of inelastic interactions on the energy distribution is similar to the dc case. Electron-electron scattering rounds the photon steps in the distribution function, thus creating a quasi-thermal equilibrium. Inelastic electron-phonon scattering cools the electron bath, creating a parallel relaxation channel to the diffusive transport. This means that the response of the electron bath can be fast for materials with strong electron-phonon interaction, even when diffusion times are long. It is hence the dominating relaxation mechanism which determines the frequency cut-off $\hbar\omega_{cut-off} \approx \min\{\tau_D, \tau_{eph}\}$. Electron-electron interactions have almost no influence on the response time of the system, because no energy is relaxed.

2.3.4 Nonlinear transport

The superconducting ground state is explicitly dependent on a non-equilibrium quasiparticle distribution. The most obvious example is the fact that superconductivity is gradually suppressed if the temperature is raised to T_c . However, a general non-equilibrium quasiparticle distribution can also influence other aspects of the superconducting state. Therefore it is convenient to split a non-equilibrium into an even and an odd part in particle-hole space. The even part, or temperature mode, has a similar influence as an increase in temperature. The odd part, or charge mode, describes a situation in which the quasiparticle spectrum contains an overabundance of electron-like (or hole-like) quasiparticles. In that case the quasiparticle system contains a net electric charge, which is compensated by a change in the number of Cooper pairs in the condensate. The presence of such a charge mode is related to the injection of electrons (holes) and leads to the presence of an electric field in the superconductor.

A microscopic description should not only include both the quasiparticles and the condensate, but also their interactions. Using the anomalous propagators of the quasi-classical theory it is possible to keep track of the coherence properties of the electrons in the superconductor. In addition, a generalized distribution function $h(x, \epsilon, t)$ is introduced, which can be disentangled into a symmetric (temperature mode, f_L) and an asymmetric part (charge mode, f_T) with re-

spect to the Fermi level: $h = 1 - f_L - f_T$. Using a perturbation theory called a Keldysh contour, one can obtain a set generalized diffusion equations for f_L and f_T [34, 35, 36, 37, 38].

We consider a superconducting wire between normal contact pads, analogous to the normal wire in Section 2.3.3. The massive normal electrodes act as equilibrium reservoirs, from which normal quasiparticles are injected into the superconductor. At a given bias point, the superconductor is found to exhibit two metastable ground states, called a global and a bimodal superconducting state. The two states have a different resistance, electric potential distribution, superconducting order parameter and distinct contributions of normal and supercurrents. For the global superconducting state, the wire is in one coherent state and most of the current is carried by Cooper pairs as a supercurrent. Only over a distance of roughly one coherence length near the interface, normal quasiparticles injected from the reservoirs penetrate the superconductor. This leads to charge accumulation and a dc electric field inside the superconductor, with an associated, relatively small resistance of roughly $R \sim \rho\xi/A$. The bimodal state consists of two distinct superconducting blobs near the ends of the wire. The center of the wire stays normal due to a strong temperature mode non-equilibrium, caused by the electric dissipation of the normal electrons which dominate the transport in this case.

2.4 Dielectric environment

The previous Section discusses driven electrons in mesoscale structures. However, such structures are deposited on a support material, which is in most practical cases a dielectric substrate. Apart from mechanical support, the substrate also acts as a heat sink for the phonons of the metal films. Furthermore, it interacts with the electronic system, as the electric fields used to drive the electron system also penetrate this dielectric substrate.

2.4.1 Phonon relaxation

Energy which is dissipated in the electron system of a mesoscale structure, is eventually relaxed as phonons in the metallic films. These excess phonons escape to the dielectric substrate within a time scale τ_{esc} . Phonons which are reabsorbed by the electron system before they escape, effectively enhance the inelastic electron-phonon relaxation times [39]. The escape time τ_{esc} is set by an attempt escape frequency ν_{esc} and the phonon-transmissivity T_{esc} of the metal-substrate interface. The attempt frequency $\nu_{esc} = c_s/2t$ is to first order given by

the phonon velocity (the speed of sound c_s) divided by the thickness of the film t .

Alternatively, the film phonons can be modeled as an extra thermal bath with a temperature T . The number of phonon modes scales with T^2 at low temperatures, and each phonon carries an average energy comparable to $k_B T$. This leads to a heat capacity $C(T)$ and conductance $G(T)$, which both scale with the temperature cubed T^3 . While the conductance scales with the contact area of the film, the heat capacity scales with its volume. The relaxation time for the phonon bath is therefore temperature independent and proportional to the film thickness $\tau_{ph-sub} = C/G \sim V/A = t$.

The transmissivity D of the interface can be modeled by an acoustic mismatch model [40], where reflection at the interface is due to a mismatch in sound velocity between the two materials. It also includes the generation of surface waves which travel at the interface between the two materials. In a diffusive mismatch model one assumes every phonon scatters at the interface. The diffusive mismatch model usually overestimates the escape time, while the acoustic mismatch model underestimates it. However, for solid-solid interfaces their values differ only by roughly 30 % [41].

In some cases, the dielectric substrate itself does not behave as an equilibrium bath. An example is given by thin SiN_x membranes, which are used for their low thermal conductance, for example in sensitive detectors. However, in *Chapter 6* we show that also more conventional substrates can suffer from effects due to non-equilibrium phonons.

2.4.2 Two level systems

Electric fields used for driving, are not confined to the metal structures but extend deep into the dielectrics surrounding the sample. Two level systems (TLS) can be present in dielectrics, at metal-dielectric interfaces and on different surfaces. The interaction between the driving field and the dipole moment of these two level systems leads to dissipation through resonant modes and to phase fluctuations in the field [42].

The origin of two level systems is most probable to be found in different atomic configurations of an amorphous material. These configurations have a slight difference in energy and are coupled by a tunnel element. Through their dipole moment \mathbf{d}_0 they affect both the real and imaginary part of the dielectric

permittivity ϵ of the host material (for weak fields) [43]:

$$\frac{\epsilon''}{\epsilon} = \delta_{TLS}^0 \tanh\left(\frac{\hbar\omega}{2k_B T}\right), \quad (2.3)$$

$$\frac{\epsilon'}{\epsilon} = -\frac{\delta_{TLS}^0}{\pi} \left\{ \operatorname{Re} \left[\Psi \left(\frac{1}{2} - \frac{\hbar\omega}{2j\pi k_B T} \right) \right] - \log \frac{\epsilon_{max}}{w\pi k_B T} \right\}. \quad (2.4)$$

In this equation, δ_0 is the loss tangent at zero temperature in a weak electric field, Ψ is the complex digamma function, and ϵ_{max} is the maximum energy splitting of TLS. The imaginary part ϵ'' is connected to dissipation (losses), while the real part ϵ' induces changes in the phase of the field. Strong fields saturate the TLS leading to a decrease in losses given by a factor $1/\sqrt{1 + |E/E_c|^2}$, with E_c a critical field [44]. The influence on the real part ϵ' is small.

If the TLS fluctuates randomly between its different states due to interaction with the environment, this will also induce a fluctuation in the dielectric permittivity. The presence of TLS hence influences both electric losses and phase noise. In Section 3.4 and *Chapters 4* and *5* of this thesis we analyze how these effects can be identified and minimized by a careful design for microwave resonators.

References

- [1] W. Ashcroft and N. D. Mermin, *Solid State Physics*, Thomson Learning, 1976.
- [2] W. Pauli, *The Connection Between Spin and Statistics*, Phys. Rev. **58**, 716 (1940).
- [3] H. J. Levinson, F. Greuter, and E. W. Plummer, *Experimental band structure of aluminum*, Phys. Rev. B **27**, 727 (1983).
- [4] F. Litimein, B. Bouhafs, Z. Dridi, and P. Ruterana, *The electronic structure of wurtzite and zincblende AlN: an ab initio comparative study*, New J. of Phys. **4**, 1 (2002).
- [5] D. Pines and P. Nozieres, *The theory of quantum liquids I*, Addison-Wesley Publishing Co., 1989.
- [6] L. N. Cooper, *Bound Electron Pairs in a Degenerate Fermi Gas*, Phys. Rev. **104**, 1189 (1956).
- [7] A. I. Lichtenstein, M. I. Katsnelson, and G. Kotliar, *Finite-Temperature Magnetism of Transition Metals: An ab initio Dynamical Mean-Field Theory*, Phys. Rev. Lett. **87**, 067205 (2001).

-
- [8] A. H. Morrish, *The physical principles of magnetism*, Wiley, New York, 1965.
- [9] P. Mohn and E. P. Wohlfarth, *The Curie temperature of the ferromagnetic transition metals and their compounds*, J. of Phys. F: Metal Physics **17**, 2421 (1987).
- [10] M. A. Biondi and M. P. Garfunkel, *Millimeter Wave Absorption in Superconducting Aluminum. I. Temperature Dependence of the Energy Gap*, Phys. Rev. **116**, 853 (1959).
- [11] S. Skalski, O. Betbeder-Matibet, and P. R. Weiss, *Properties of Superconducting Alloys Containing Paramagnetic Impurities*, Phys. Rev. **136**, A1500 (1964).
- [12] M. Tinkham, *Introduction to superconductivity*, Dover publications, Mineola, 1996.
- [13] J. Bardeen, L. N. Cooper, and J. R. Schrieffer, *Theory of Superconductivity*, Phys. Rev. **108**, 1175 (1957).
- [14] Y. Imry, *Introduction to Mesoscopic Physics*, Oxford University Press, 1997.
- [15] A. F. Andreev, *Thermal conductivity of the intermediate state of superconductors*, Sov. Phys. JETP **19**, 1228 (1964).
- [16] G. Eilenberger, *Transformation of Gorkov's equation for type II superconductors into transport-like equations*, Z. Phys. **214**, 195 (1968).
- [17] A. L. Shelankov, *On the derivation of quasiclassical equations for superconductors*, J. of Low Temp. Phys. **60**, 29 (1985).
- [18] K. D. Usadel, *Generalized Diffusion Equation for Superconducting Alloys*, Phys. Rev. Lett. **25**, 507 (1970).
- [19] L. P. Gor'kov, *Microscopic derivation of the Ginzburg-Landau equations in the theory of superconductivity*, Sov. Phys. JETP **36**, 1364 (1959).
- [20] W. Belzig, F. K. Wilhelm, C. Bruder, and G. Schön, *Quasiclassical Greens function approach to mesoscopic superconductivity*, Superlattices and Microstructures **25**, 1251 (1999).
- [21] A. Cottet, D. Huertas-Hernando, W. Belzig, and Y. V. Nazarov, *Spin-dependent boundary conditions for isotropic superconducting Green's functions*, Phys. Rev. B **80**, 184511 (2009).
- [22] G. E. Blonder, M. Tinkham, and T. M. Klapwijk, *Transition from metallic to tunneling regimes in superconducting microconstrictions: Excess cur-*

- rent, charge imbalance, and supercurrent conversion, *Phys. Rev. B* **25**, 4515 (1982).
- [23] M. Y. Kuprianov and V. F. Lukichev, *Thermal conductivity of the intermediate state of superconductors*, *Sov. Phys. JETP* **67**, 1163 (1988).
- [24] E. L. Wolf, *Principles of electron tunnel spectroscopy*, International Series of Monographs on Physics Vol. 71, Oxford University Press, New York, 1985.
- [25] S. Datta, *Transport in mesoscopic systems*, Cambridge University Press, 1995.
- [26] F. Jedema, *Electrical spin injection in metallic mesoscopic spin valves*, PhD thesis, Rijksuniversiteit Groningen, 2002.
- [27] H. Pothier, S. Guéron, N. O. Birge, D. Esteve, and M. H. Devoret, *Energy Distribution Function of Quasiparticles in Mesoscopic Wires*, *Phys. Rev. Lett.* **79**, 3490 (1997).
- [28] K. E. Nagaev, *On the shot noise in dirty metal contacts*, *Phys. Lett. A* **169**, 103 (1992).
- [29] K. E. Nagaev, *Influence of electron-electron scattering on shot noise in diffusive contacts*, *Phys. Rev. B* **52**, 4740 (1995).
- [30] V. I. Kozub and A. M. Rudin, *Shot noise in mesoscopic diffusive conductors in the limit of strong electron-electron scattering*, *Phys. Rev. B* **52**, 7853 (1995).
- [31] A. H. Steinbach, J. M. Martinis, and M. H. Devoret, *Observation of Hot-Electron Shot Noise in a Metallic Resistor*, *Phys. Rev. Lett.* **76**, 3806 (1996).
- [32] P. K. Tien and J. P. Gordon, *Multiphoton Process Observed in the Interaction of Microwave Fields with the Tunneling between Superconductor Films*, *Phys. Rev.* **129**, 647 (1963).
- [33] A. V. Shytov, *Structured energy distribution and coherent ac transport in mesoscopic wires*, *Phys. Rev. B* **71**, 085301 (2005).
- [34] L. V. Keldysh, *Diagram technique for nonequilibrium processes*, *Sov. Phys. JETP* **20**, 1018 (1965).
- [35] A. Schmid and G. Schön, *Linearized kinetic equations and relaxation processes of a superconductor near T_c* , *J. of Low Temp. Phys.* **20**, 207 (1975).
- [36] J. Rammer and H. Smith, *Quantum field-theoretical methods in transport theory of metals*, *Rev. Mod. Phys.* **58**, 323 (1986).
- [37] T. H. Stoof and Y. V. Nazarov, *Kinetic-equation approach to diffusive superconducting hybrid devices*, *Phys. Rev. B* **53**, 14496 (1996).

- [38] N. Kopnin, *Theory of Nonequilibrium Superconductivity*, International Series of Monographs on Physics Vol. 110, Oxford University Press, New York, 2001.
- [39] A. Rothwarf and B. N. Taylor, *Measurement of Recombination Lifetimes in Superconductors*, Phys. Rev. Lett. **19**, 27 (1967).
- [40] R. Peterson and A. Anderson, *The Kapitza thermal boundary resistance*, J. of Low Temp. Phys. **11**, 639 (1973).
- [41] E. T. Swartz and R. O. Pohl, *Thermal boundary resistance*, Rev. Mod. Phys. **61**, 605 (1989).
- [42] W. A. Phillips, *Two-level states in glasses*, Reports on Progress in Physics **50**, 1657 (1987).
- [43] J. Gao, M. Daal, A. Vayonakis, S. Kumar, J. Zmuidzinas, B. Sadoulet, B. A. Mazin, P. K. Day, and G. H. Leduc, *Experimental evidence for a surface distribution of two-level systems in superconducting lithographed microwave resonators*, Appl. Phys. Lett. **92**, 152505 (2008).
- [44] J. M. Martinis, K. B. Cooper, R. McDermott, M. Steffen, M. Ansmann, K. D. Osborn, K. Cicak, S. Oh, D. P. Pappas, R. W. Simmonds, and C. C. Yu, *Decoherence in Josephson Qubits from Dielectric Loss*, Phys. Rev. Lett. **95**, 210503 (2005).

Chapter 3

Experimental Reality of Model Systems

3.1 Introduction

The structures described in this thesis are designed to probe fundamental physical processes or to have a certain functionality. In order to realize a desired sample, different materials have to be deposited and patterned in a series of fabrication steps. There is a close connection between the design, the fabrication route, and the physical properties of the final structure. Design choices depend on requirements for the device, for example a material needs to be a superconductor with a certain critical temperature T_c or electrical conductivity σ . Additional constraints are placed by the availability and compatibility of materials, deposition methods, and patterning steps. The measurement environment restricts the choice further, as only a limited parameter space is accessible. This can be the available temperature range, the number of electrical wires, and the requirements on their filtering; or even the dimensions of the sample holder. In the end, measurements are done to reveal the physical properties or functionality of the sample. These measurements are interpreted within a conceptual framework, which makes certain assumptions and simplifications about the geometry, material properties, and physics of the sample. As reality is complex, it is necessary to assess the validity of such a *model system*. The following sections illustrate the connection between a conceptual design, fabrication, measurement, and model for the devices described in this thesis.

3.2 Superconducting nanowires

In *Chapters 8 and 9* we consider electron transport through a superconducting nanowire between normal (NsN) or ferromagnetic (FsF) contacts. The contacts serve as equilibrium reservoirs, from which electrons with a well-defined energy (and spin) distribution $f(\epsilon \pm eU/2, T, \uparrow\downarrow)$ are injected into the wire. The structures are realized by shadow evaporation through a double layer resist mask (Fig. 3.1). Using electron beam lithography (EBL), structures with nanoscale dimensions can be patterned into the resist layer. The two layers have a different sensitivity, or a different solution is used to develop the exposed areas of each layer. This allows to create an undercut, which means that the lower layer is developed more than the upper one. In the following steps material is evaporated through this mask, under different angles. This deposition method is very directional, therefore the pattern written in the resist mask is projected onto the substrate at different positions for each angle. The strength of this technique lies in the fact that it allows to create a structure with multiple materials with a single mask, without breaking the vacuum during deposition. The interfaces

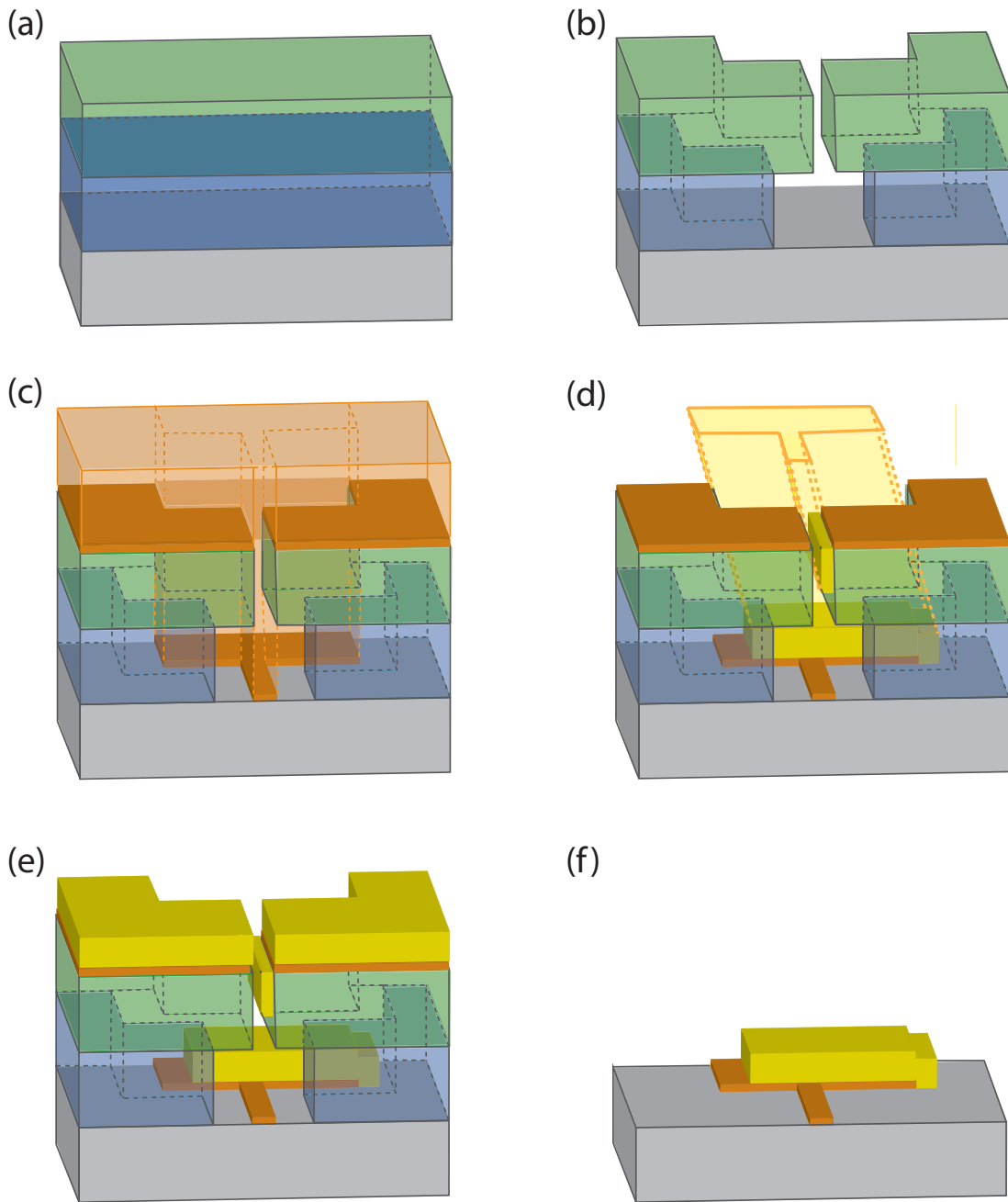


Figure 3.1: The fabrication recipe for a superconducting nanowire between normal pads. (a) A PGMI/PMMA double resist layer is deposited on a Si/SiO_x substrate. (b) After electron beam lithography (EBL), the lower resist layer is developed more extensively than the upper one leading to an undercut. (c) The Aluminum wire is deposited normal to the sample. (d) The Copper contacts are evaporated under an angle of 37°, which shifts the pattern. (e) The structure after the two evaporation steps. (f) When the double resist layer is removed, only the metal which sticks to the substrate is left.

between the materials can be very clean, and there is no need to pattern the layers afterwards.

Fig. 3.1 schematically shows the fabrication of an aluminum superconducting nanowire between normal, copper pads. The normal reservoirs of the sample are massive to provide an effective thermalization for hot electrons. Although they consist of an aluminum-copper bilayer they stay normal down to the lowest temperature measured due to the inverse proximity effect of the copper on the aluminum. This requires a clean interface between the two metal layers, which makes the choice for shadow evaporation evident. Although the considerations above are implemented in the design and fabrication of the structures, measurements still show signs of heating and superconducting proximity effects. Therefore a careful analysis of the validity of the assumed boundary conditions is necessary, before interpreting the data (*Chapter 8*). For the FsF structure, relatively thin, ellipsoid contact pads are chosen to favor a single domain ferromagnetic contact with little stray fields. To achieve an as uniform spin polarization as possible in the ferromagnet-superconductor contact, the size of this contact is chosen to be small. This means that even for moderate driving, the contacts can no longer be assumed to be in thermal equilibrium (*Chapter 9*) The design of a sample is a compromise between different requirements. As not all of them are completely met, it is a necessity to include unwanted effects explicitly in the analysis of the sample.

3.3 Aluminium Nitride tunnel barriers

A tunnel junction consists of two electrodes with the barrier material in between. A popular barrier material is amorphous aluminum oxide AlO_x , because of a relatively easy and reliable fabrication route [1]. For highly transparent barriers however, polycrystalline AlN has superior properties [2]. In this case N_2 molecules have to be broken by a plasma to nitridize the aluminum, which complicates the fabrication process. A convenient fabrication route is to first deposit the bottom electrode with a thin (≈ 7 nm) layer of aluminum on top. In a second step, the Al can be oxidized or nitridized to create the AlO_x or AlN barrier, after which the top electrode is deposited. The deposition of this trilayer is done without breaking the vacuum to ensure a controllable barrier growth and clean interfaces between the different layers. In a subsequent step the junction is defined using EBL and a reactive ion etch. Finally the top wiring is deposited and patterned to contact the junction.

As seen in Fig. 3.2, a tunnel barrier consists of a thin layer of dielectric (typi-

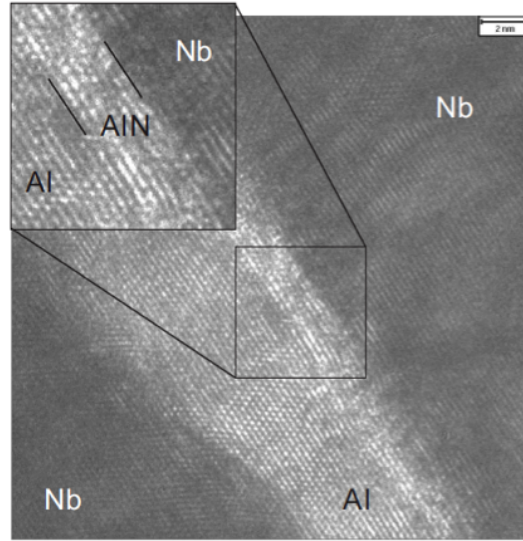


Figure 3.2: An Aluminum Nitride tunnel barrier in between Nb electrodes, visualized by high resolution electron microscopy.

cally a few nm), which is insulating due to the presence of a bandgap. Impinging electrons have a small probability $|T|^2 \approx 10^{-3} - 10^{-5}$ to tunnel through this layer, as their wavefunction has an evanescent tail which penetrates the potential barrier. In a WKB approximation, this probability depends exponentially on the thickness d and the height $e\phi$ of the barrier $|T| \approx \exp(-\alpha d \sqrt{e\phi - \epsilon})$, with ϵ the energy of the electron and α a constant that depends on the effective electron mass. If specular tunneling is assumed and for small voltages $eV \ll e\phi$, this gives rise to a constant normal tunnel resistance R_n which scales with the number of channels and the transmission per channel $|T|$ [3].

In superconducting tunnel junctions, the presence of the superconducting gap suppresses single electron tunneling at subgap energies $\epsilon < \Delta$. Higher order electron tunneling is still possible, but small in magnitude as it scales with $|T|^4, |T|^6, \dots$. The subgap current, which is measured in practice, exceeds the expected values. The excess current can be attributed to a few mechanisms, such as subgap states in the superconductor or *reflectionless* tunneling in which an electron coherently attempts multiple times to tunnel [4, 5]. Alternatively, it is known that tunnel barriers are laterally inhomogeneous, in the sense that their thickness varies over the area of the junction. Therefore a few, highly transmissive spots can dominate the electron transport while the average transmission is very low. In *Chapter 7* we analyze the influence of such a laterally inhomogeneous tunnel junction on the electrical and thermal transport through a normal metal - insulator - superconductor junction.

3.4 Superconducting resonators

A superconducting resonator consists of a superconducting waveguide, along which microwave electromagnetic fields can travel [6]. If the length of the superconducting line corresponds to a multiple of a quarter wavelength $l = n\frac{\lambda}{4}$ of the field, it becomes resonant. The shortest resonator is a quarterwave resonator $\lambda_0 = 4l$, with an associated resonant frequency $f_0 = v_{ph}/4l$. The phase velocity v_{ph} at which the wave travels, is set by the capacitance C and inductance L of the waveguide $v_{ph} = 1/\sqrt{LC}$. The capacitance is determined by the geometry of the waveguide and the dielectric permittivity ϵ_r of the substrate. The inductance consists of a geometric inductance L_g and a kinetic inductance L_k , whereby $L = L_g + L_k$. The kinetic inductance is due to kinetic energy of Cooper pairs which are accelerated (and decelerated) by the electromagnetic field. Hence, the resonant frequency depends on the geometry of the waveguide, the dielectric permittivity ϵ_r , and the kinetic inductance of the superconductor. Losses are quantified by a quality factor Q , which corresponds to the number of field cycles it takes before a signal is completely dissipated. The properties of the resonator are obtained by measuring the transmission through a feed line, which is capacitively coupled to the resonator. At the resonant frequency, the electromagnetic field is absorbed by the resonator and the majority of the signal is reflected towards the input port of the feed line. This causes a dip in the amplitude of the transmitted signal and a shift in its phase. Therefore, the resonant frequency f_0 can be measured by either reading out the amplitude or the phase of the signal. In a superconductor these losses are extremely low leading to quality factors above a million, as the current is carried by dissipationless Cooper pairs. Only thermally excited quasiparticles contribute to the loss and their number decays exponentially at low temperatures, at least theoretically [7, 8]. The number of quasiparticles fluctuates due to the interaction with the phonon bath, which introduces recombination-generation noise. Another source of losses and noise are two level systems, which interact with the microwave field through their dipole moment (Section 2.4.2). They alter both the real and the imaginary part of the dielectric permittivity, leading to changes in the resonant frequency f_0 and the quality factor Q (for weak fields) [9]:

$$\frac{\Delta f_0}{f_0} = -\frac{\int_{V_h} \epsilon'_{TLS} |\vec{E}|^2 d\vec{r}}{2 \int_V \epsilon |\vec{E}|^2 d\vec{r}} = \frac{F \delta_{TLS}^0}{\pi} \left\{ \text{Re} \left[\Psi \left(\frac{1}{2} - \frac{\hbar\omega}{2j\pi k_b T} \right) \right] - \log \frac{\epsilon_{max}}{w\pi k_b T} \right\} \quad (3.1)$$

$$\Delta \frac{1}{Q} = -\frac{\int_{V_h} \epsilon''_{TLS} |\vec{E}|^2 d\vec{r}}{\int_V \epsilon |\vec{E}|^2 d\vec{r}} = F \delta_{TLS}^0 \tanh \left(\frac{\hbar\omega}{2k_b T} \right) \quad (3.2)$$

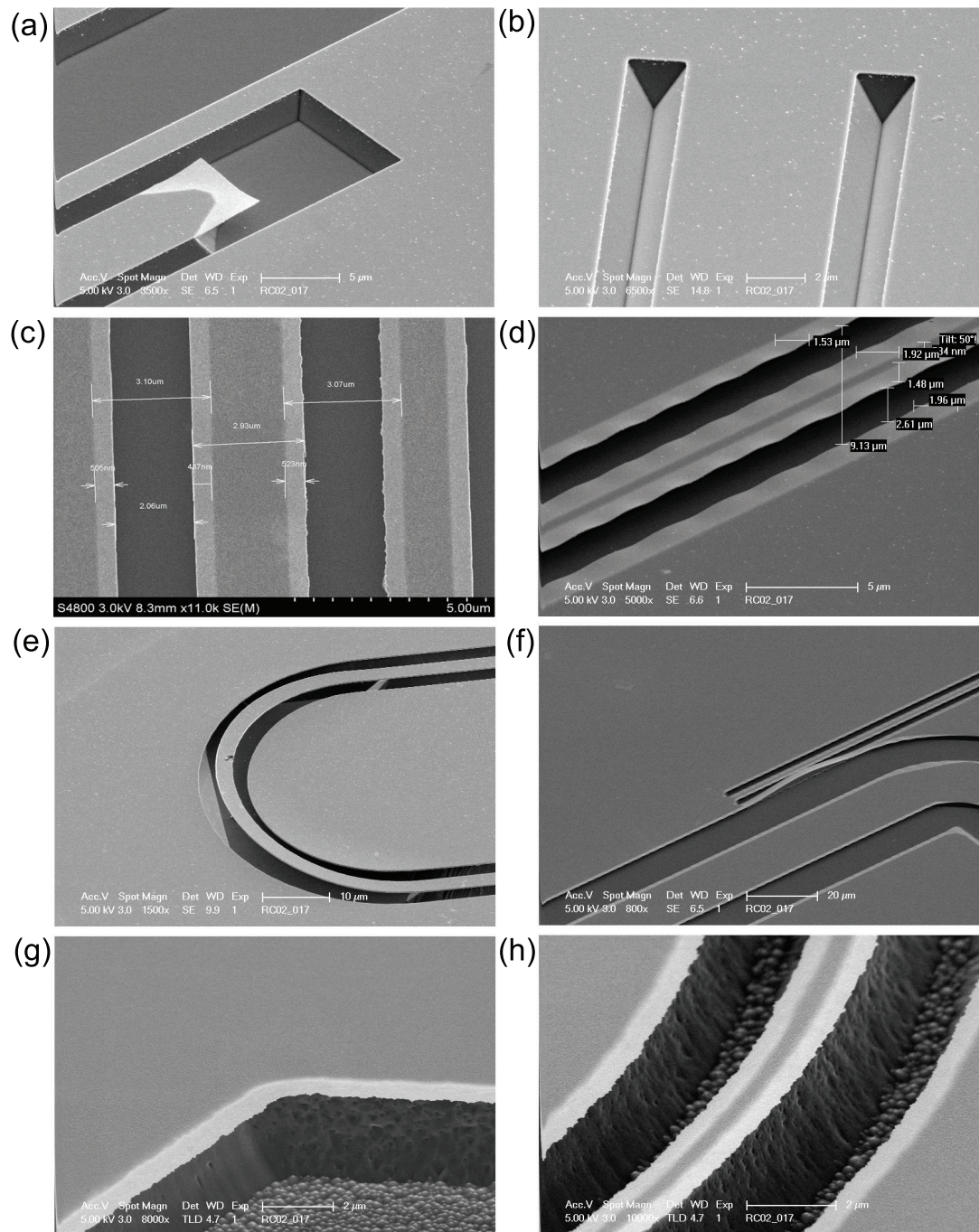


Figure 3.3: Images of different etch recipes for Si, using scanning electron microscopy. Wet-etching with KOH results in a highly anisotropic etch. (a,b) For resonators aligned along the $\langle 011 \rangle$ axis the etch is self-limiting and there is no undercut. (c,d) If the resonators are aligned along the $\langle 010 \rangle$ axis, the etch is isotropic, resulting in a considerable undercut. The compressive stress in the NbTiN results in resonators with ‘wobbles’. (e,f) Bends or narrow lines are better avoided. (g,h) Another possible fabrication route is a reactive ion etch with SF_6/O_2 , but this degrades the NbTiN film quality.

with

$$F = \frac{\int_{V_h} \epsilon_h |\vec{E}|^2 d\vec{r}}{2 \int_V \epsilon |\vec{E}|^2 d\vec{r}} = \frac{w_h^e}{w^e} \quad (3.3)$$

being a filling factor which reflects the fact that only a fraction F of the field energy is stored in the volume V_h where the TLS are located. The changes in f_0 and Q depend on temperature through the occupation numbers of the two level states. If these occupation numbers fluctuate, the resonant frequency starts to fluctuate accordingly:

$$\frac{S_{\delta f_0}}{f_0}^2 = \frac{\int_{V_h} S_\epsilon(\vec{r}, f, T) |\vec{E}|^4 d\vec{r}}{4 \left(\int_V \epsilon |\vec{E}|^2 d\vec{r} \right)^2}, \quad (3.4)$$

with $S_\epsilon(\vec{r}, f, T)$ being the noise spectral density of the fluctuations in ϵ'_{TLS} . For strong fields there is a saturation effect of the field on the TLS, which is taken into account by a heuristic factor $S_\epsilon = S_\epsilon / \sqrt{|\vec{E}(\vec{r})|^2 + E_{n,c}^2(f, T)}$.

Two level systems hence influence the resonant frequency, quality factor, and the noise of a superconducting resonator, with a strong dependence on the microwave power and the temperature. In addition their effect depends on their strength, location, and the field distribution. Therefore an optimized choice of materials, fabrication route, and geometry can significantly reduce their effect. We use coplanar waveguide NbTiN quarterwave resonators, as the quality factor for NbTiN is dominated by the exposed substrate surface. A 50 to 300 nm NbTiN is DC sputter deposited on a HF-cleaned high resistivity ($> 1 \text{ k}\Omega\text{cm}$) $\langle 100 \rangle$ -oriented Si wafer, without an additional Ar sputter clean. Patterning is done by EBL and a reactive ion etch in an SF_6/O_2 plasma. In order to identify the location of the TLS, the exposed Si is removed from the gaps of the CPW with a KOH wet etch. Due to the crystallographic properties of the Si, this etch is highly anisotropic. If the resonator is oriented along the $\langle 110 \rangle$ axis (Fig. 3.3a,b), this etch leads to a gap with 54° sidewalls and no undercut. For resonators oriented along the $\langle 100 \rangle$ (Fig. 3.3c,d), a strong undercut is observed. However, the compressive stress of the NbTiN film resulted in wobbled edges. Comparing these different geometries to a reference sample, we identify in *Chapters 4* and *5* the exposed substrate in the gaps of the CPW as the dominant source of TLS. At the same time we demonstrate a reduction in noise and an improvement of the quality factor, by removing these exposed areas.

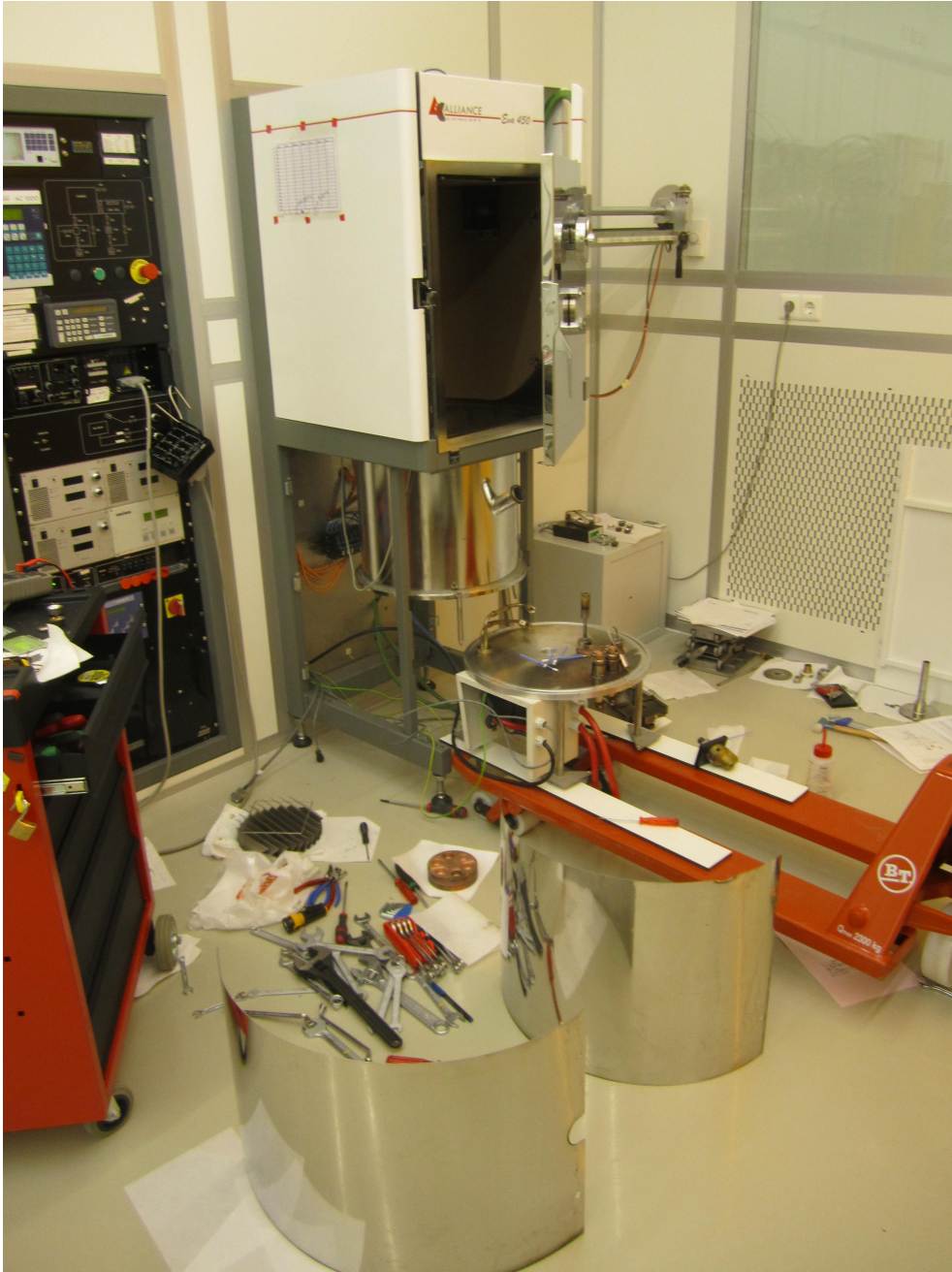


Figure 3.4: Experimental reality of the clean room.

References

- [1] W. Miller, R.E. and Mallison, A. Kleinsasser, K. Delin, and E. Macedo, *Niobium trilayer Josephson tunnel-junctions with ultrahigh critical-current densities*, Appl. Phys. Lett. **63**, 1423 (1993).
- [2] T. T. Zijlstra, C. F. J. Lodewijk, N. Verduyssen, F. D. Tichelaar, D. N. Loudkov, and T. M. Klapwijk, *Epitaxial aluminum nitride tunnel barriers grown by nitridation with a plasma source*, Appl. Phys. Lett. **91**, 233102 (2007).
- [3] J. G. Simmons, *Generalized Formula for the Electric Tunnel Effect between Similar Electrodes Separated by a Thin Insulating Film*, Journal of Applied Physics **34**, 1793 (1963).
- [4] B. J. van Wees, P. de Vries, P. Magnée, and T. M. Klapwijk, *Excess conductance of superconductor-semiconductor interfaces due to phase conjugation between electrons and holes*, Phys. Rev. Lett. **69**, 510 (1992).
- [5] F. W. J. Hekking and Y. V. Nazarov, *Subgap conductivity of a superconductor / normal-metal tunnel interface*, Phys. Rev. B **49**, 6847 (1994).
- [6] R. Barends, *Photon-detecting Superconducting Resonators*, PhD thesis, TU Delft, 2009.
- [7] S. B. Kaplan, C. C. Chi, D. N. Langenberg, J. J. Chang, S. Jafarey, and D. J. Scalapino, *Quasiparticle and phonon lifetimes in superconductors*, Phys. Rev. B **14**, 4854 (1976).
- [8] P. J. de Visser, J. J. A. Baselmans, P. Diener, S. J. C. Yates, A. Endo, and T. M. Klapwijk, *Number Fluctuations of Sparse Quasiparticles in a Superconductor*, Phys. Rev. Lett. **106**, 167004 (2011).
- [9] B. A. Mazin, *Microwave kinetic inductance detectors*, PhD thesis, California Institute of Technology, 2008.

Chapter 4

Minimal resonator loss for circuit quantum electrodynamics

We report quality factors of up to $500 \cdot 10^3$ in superconducting resonators at the single photon levels needed for circuit quantum electrodynamics. This result is achieved by using NbTiN and removing the dielectric from regions with high electric fields. As demonstrated by a comparison with Ta, the crucial sources of intensity-dependent loss are dielectrics on the surface of the metal and substrate.

This chapter was published as R. Barends, N. Vecruyssen, A. Endo, P. J. de Visser, T. Zijlstra, T. M. Klapwijk, P. Diener, S. J. C. Yates, and J. J. A. Baselmans *Applied Physics Letters* 91, 023508 (2010). The main contribution of the present author was in the design of the experiment and the fabrication of the devices.

4.1 Introduction

In circuit quantum electrodynamics quantum information processing is done by coupling the qubit state to a single photon bound to a superconducting resonator [1]. The lifetime of a single photon with frequency f is defined by: $\tau = Q/2\pi f$ [2], therefore a high resonator quality factor (Q) is needed to maximize the lifetime. Presently used resonators, made from Nb or Al, have quality factors on the order of 10^4 to 10^5 [2, 3, 4, 5, 6]. In contrast, superconducting resonators for astronomical photon detection [7] have shown quality factors in excess of a million in the many-photon regime. One would like to maintain these high values down to the single photon level. Therefore, we study the unloaded quality factor of NbTiN and, for comparison, Ta quarterwave resonators down to the single photon level. NbTiN has a minimal dielectric layer compared to Nb, Al and Ta [8]. We find that in the single photon regime the quality factor of NbTiN resonators is so high that the loss is largely due to the exposed substrate surface. In contrast, for Ta resonators the metal surface dominates. We show that a further reduction of the loss in NbTiN resonators is achieved by removing the substrate from the regions with a high electric field density. This increases the quality factor to half a million for resonators with a central line width of $6\ \mu\text{m}$, three times higher than recently reported for Re [2].

4.2 Power dependence of quality factors in NbTiN and Ta resonators

We use NbTiN and Ta quarterwave coplanar waveguide resonators which are capacitively coupled to a feedline [7, 8], see inset Fig. 4.1. This allows extracting the unloaded quality factor from the feedline transmission. The NbTiN films, 300 and 50 nm thick, are DC sputter deposited on a hydrogen passivated high resistivity ($> 1\ \text{k}\Omega\text{cm}$) $\langle 100 \rangle$ -oriented Si wafer. The NbTi target used contains 70 at. % Nb and 30 at. % Ti. Patterning is done by reactive ion etching in an SF_6/O_2 plasma. For the 300 nm thick film the critical temperature is $T_c = 14.7\ \text{K}$, the low temperature resistivity is $\rho = 161\ \mu\Omega\text{cm}$ and residual resistance ratio $RRR = 0.94$. For the 50 nm thick film: $T_c = 13.6\ \text{K}$, $\rho = 142\ \mu\Omega\text{cm}$ and $RRR = 0.96$. The 150 nm thick Ta film ($T_c = 4.43\ \text{K}$, $\rho = 8.4\ \mu\Omega\text{cm}$ and $RRR = 3.0$) is sputtered on a similar wafer and patterned in a CF_4/O_2 plasma. The devices are cooled to 310 mK using a He-3 sorption cooler and down to 60 mK using an adiabatic demagnetization refrigerator. The sample space magnetically is shielded [9]. Measurements have been done using a vector network analyzer,

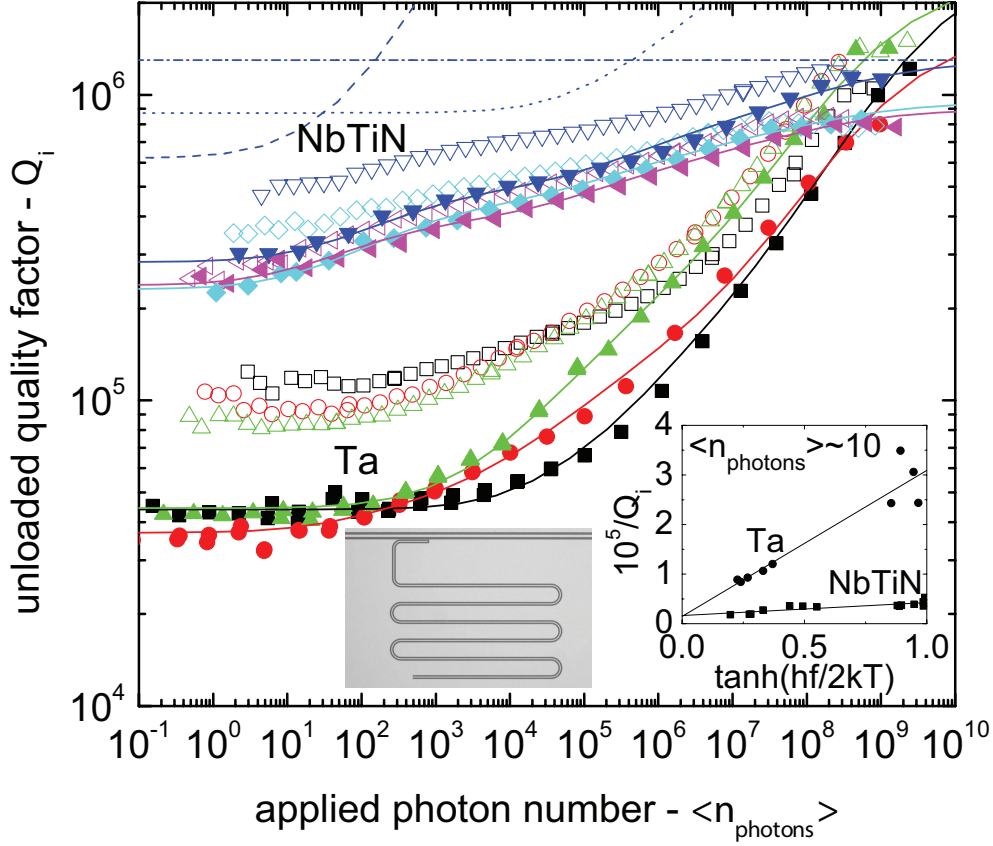


Figure 4.1: The unloaded quality factor of NbTiN and Ta quarterwave resonators versus applied microwave photon number in the resonator. Bath temperatures are 60 mK (closed symbols) and 310 mK (open symbols). Central line width is $S = 3 \mu\text{m}$ and gap width is $W = 2 \mu\text{m}$. Frequencies of the resonators used are 3.7 (\blacktriangledown), 4.2 (\blacklozenge) and 6.2 (\blacktriangleleft) GHz for NbTiN, and 3.2 (\blacksquare), 4.5 (\bullet) and 5.0 (\blacktriangle) GHz for Ta. The solid lines are fits using Eq. 4.1. The quality factors of the metal surfaces (dashed), exposed substrate surface (dotted) and a fixed loss term (dash-dotted) are shown for the 3.7 GHz NbTiN data. The right inset shows the microwave loss in the single photon regime versus $\tanh(hf/2kT)$. The left inset shows the resonator geometry.

locked to a frequency standard. An isolator is placed in front of the low noise amplifier.

The unloaded quality factor of NbTiN and Ta resonators is plotted versus applied photon number [10] in the resonator in Fig. 4.1. The resonators have resonance frequencies in the 3-6 GHz range, a central line width of $S = 3 \mu\text{m}$ and a gap width of $W = 2 \mu\text{m}$. Bath temperatures are 60 mK and 310 mK. In the many-photon regime, quality factors between $0.8 \cdot 10^6$ and $1.5 \cdot 10^6$ are observed for both materials. In addition, in this regime the 60 mK and 310 mK data overlap.

With decreasing applied photon number the quality factors decrease. For NbTiN resonators, a weak intensity dependence is observed and quality factors decrease to $\sim 250 \cdot 10^3$ at 60 mK in the single photon regime. On the other hand, Ta quality factors degrade quickly, decreasing to $\sim 40 \cdot 10^3$. Interestingly, an inflection point is visible in the NbTiN data around $\langle n_{photons} \rangle = 10^2 - 10^3$, whereas Ta data show a plateau at low intensities. Additionally, at low intensities a temperature and frequency dependence develops for both materials. At 310 mK (open symbols) the quality factors are increased, for resonators with lower frequencies the increase is larger.

4.3 Two level systems

Previously, we have shown that NbTiN resonators contain fewer dipole two-level systems (TLS) than Ta, by measurements of the resonator frequency temperature dependence [8]. Dipole TLS are configurational defects with dipole moment p which reside in amorphous dielectrics [11], such as native oxides. Dielectric loss at low temperatures ($kT < hf$) arises from resonant absorption: $1/Q \propto \tanh(hf/2kT)/\sqrt{1 + E^2/E_s^2}$ [11, 12]. The factor $\tanh(hf/2kT)$ reflects the thermal population difference between the lower and upper level. With increasing intensity TLS are excited, lowering the loss. The saturation field $E_s = \hbar/p\sqrt{T_1T_2}$ is controlled by the dipole moment and relaxation times T_1 and T_2 .

The microwave loss of our resonators in the single photon regime scales with $\tanh(hf/2kT)$, see the inset of Fig. 4.1, consistent with resonant absorption from TLS. This also explains the frequency dependence which develops at 310 mK. Moreover, different resonators made from the same material follow the same trend, indicating that the loss is very comparable over the whole chip. In addition, the slope for Ta is steeper than for NbTiN, consistent with a larger TLS density for Ta, compared to NbTiN resonators.

In order to identify the location of these TLS and quantify the influence of their saturation on the quality factor, we calculate the effect of a hypothetical thin dielectric layer with thickness $t \rightarrow 0$ containing TLS. Dielectric loss in a quarterwave resonator due to dipole TLS is given by [2, 13]:

$$\frac{1}{Q_{TLS}} = \frac{\tanh\left(\frac{hf}{2kT}\right) \frac{1}{2} \epsilon_0 \epsilon_h \iiint_{V_h} \frac{|\vec{E}(\vec{r})|^2}{\sqrt{1 + |\vec{E}(\vec{r})|^2/E_s^2}} d\vec{r}}{\frac{1}{4} C V_r^2 l} \quad (4.1)$$

with V_r the standing wave voltage inside the resonator, l its length and C the capacitance per unit length. The dielectric loss of the layer is $1/Q_{TLS,0} =$

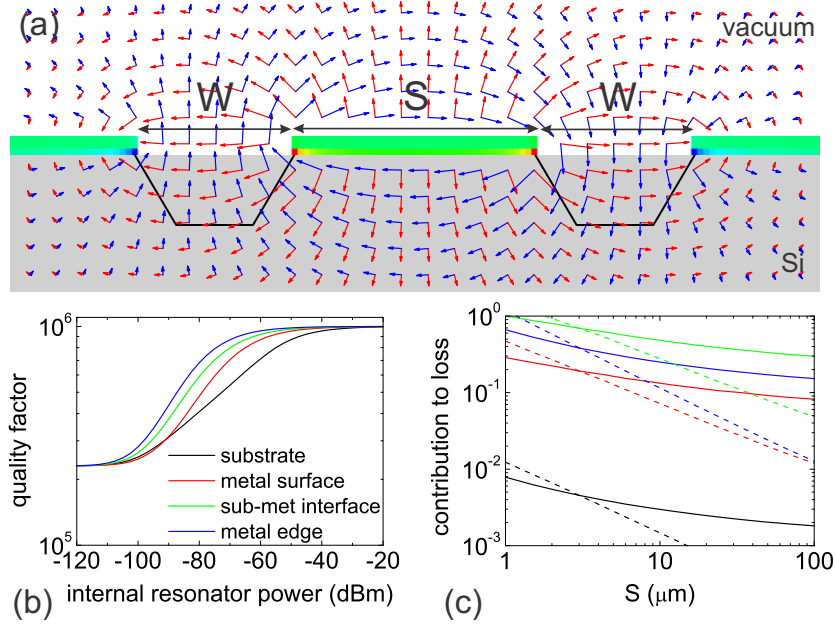


Figure 4.2: (a) the charge distribution (red denotes a positive charge, blue a negative and green a neutral one), electric fields (red arrows) and magnetic fields (blue arrows) in the coplanar waveguide geometry. (b) The power dependence using Eq. 4.1 for a TLS distribution placed on the exposed substrate surface, top metal surface, substrate-metal (sub-met) interface and etched metal edges. $Q_0 = 10^6$, and at low intensity each surface is assumed to limit the Q to $300 \cdot 10^3$. (c) The normalized contribution to loss of the dielectric layers versus central line width S , for $W = 2 \mu\text{m}$ (solid) and $W = \frac{2}{3}S$ (dashed).

$N\pi p^2/3\epsilon_0\epsilon_h$, with N the TLS density of states and V_h and ϵ_h the volume and relative permittivity of the dielectric layer hosting the TLS.

The electric fields for our resonator geometry are calculated by using the potential matrix \mathbf{P} to find the charge density q : $\mathbf{V} = \mathbf{P}\mathbf{q}$ [2, 14]. The substrate is included using the method of partial image charges. The potential matrix elements are given by $P_{ij} = P_{ji} = -(\ln|r_i - r_j| + K \ln|r_i^* - r_j|)/2\pi\epsilon_0$ for $i \neq j$, and $P_{ii} = -(\ln a + K \ln[|r_i - r_i^*| + a])/2\pi\epsilon_0$, with r_i the location of the i -th element, r_i^* the location of the i -th element mirrored in the plane of the substrate surface, a its radius, $K = (1 - \epsilon_s)/(1 + \epsilon_s)$ and ϵ_s the relative permittivity of the substrate. The electric fields and magnetic fields are shown in Fig. 4.2a.

We place this hypothetical layer on either the exposed substrate surface, top metal surface, etched metal edges or at the substrate-metal interface. Interestingly, when the dielectric layer is placed on any of the metal surfaces, its contribution to the loss is two orders of magnitude larger than when placed on

Table 4.1: The quality factor of the dielectric layer containing TLS, its saturation field and the additional loss factor for the superconducting metals and for their Si substrates, used for fitting the data in Fig. 4.1, using Eq. 4.1 and $1/Q = 1/Q_0 + 1/Q_{TLS,met}(E_{s,met}) + 1/Q_{TLS,sub}(E_{s,sub})$. Calculations have been done for $\epsilon_h = 1$ and $t \rightarrow 0$.

material	Q_0 (10^6)	$Q_{TLS,0}/\epsilon_h t$ (1/nm)	E_s (kV/m)
NbTiN	0.9-1.3	330-450	0.05
Ta	1.7-3	70-90	0.1-2
Si (NbTiN)		13-16	5
Si (Ta)		1.1-1.9	2

the exposed substrate (Fig. 4.2c). This is due to the high electric fields near the metal. In addition, a dielectric placed near the metal leads to a much stronger power dependence than when located on the substrate (Fig. 4.2b). We use this to distinguish between surfaces. Furthermore, the quality factor increases with central line width, irrespective of the location of the dielectric.

In Fig. 4.1, we show that the power dependence of the quality factor arises from the superposition of loss (solid lines) from TLS (Eq. 4.1) located at the metal surfaces (dashed line) as well as at the exposed substrate surface (dotted line) [15]. Interestingly, for NbTiN resonators the exposed substrate, together with the metal surfaces, is a significant contributor to the microwave loss. This superposition of loss closely describes the observed point of inflection at $\langle n_{photons} \rangle = 10^2 - 10^3$ as well.

The saturation fields of NbTiN are on the order of 50 V/m, see Table 4.1, similar to values for Re and Al [2]. For Ta we find a large spread in the saturation fields. The dielectric loss of NbTiN is clearly smaller than that of Ta. The substrate surface values are consistent with SiO_x . The saturation field is $E_s \sim 2 - 5$ kV/m; comparable to measurements on vitreous silica [16]. Moreover, a value of $E_s \sim 2 - 3$ kV/m has been reported for SiO_2 also by Martinis *et al.* [12]. The quality factor of the Si surface layer, assuming $t = 3$ nm and $\epsilon_h = 4$, lies around 15-200, which is on the order of the value of ~ 200 reported for SiO_2 [12]. At high intensity the quality factors are temperature independent, suggesting loss other than due to TLS. We include an intensity-independent fitting term $1/Q_0$ to account for this loss. We suspect that we reach the level of the intrinsic loss of the superconductor. For Ta, relaxation times saturate for $T/T_c < 0.2$ [17], suggesting that the quasiparticle density becomes temperature independent. At $T/T_c = 0.2$ we estimate $Q \sim 10^6$ based on Mattis-Bardeen, on the order of values found for Q_0 .

4.4 Enhanced quality factors by an optimized device geometry

The data in Fig. 4.1 and the analysis provide a clear guide towards improving the quality factor. Ta suffers from significant microwave loss due to dipole TLS in its metal surface. We believe that the presence of a native oxide is the reason why resonators made of Nb, Ta, Al, or deposited on top of SiO₂, consistently show low quality factors in the single photon regime [2, 3, 4, 5, 6]. In this respect NbTiN is different, because the metal atoms are bound to nitrogen. Moreover, resonators with $S = 3 \mu\text{m}$ and $W = 2 \mu\text{m}$ have quality factors around $250 \cdot 10^3$, nearly a doubling compared to Re on Si resonators which have quality factors around $150 \cdot 10^3$ (loaded, with $Q_c > Q_i$) and are wider ($S = 5 \mu\text{m}$ and $W = 2 \mu\text{m}$) [2]. Nevertheless, the NbTiN resonator quality factor is significantly limited by the exposed and oxidized Si surface. Therefore NbTiN has a clean surface compared to Si, as the metal surface influences the loss much stronger than the exposed substrate (Fig. 4.2c).

With NbTiN shown to be a superior superconductor, we have redesigned our resonators to have fewer dielectrics. We have made 50 nm thick NbTiN resonators, fully straight, which are aligned along the $\langle 110 \rangle$ axis of the $\langle 100 \rangle$ -oriented HF-cleaned Si wafer. Using KOH wet etching, grooves of $0.9 \mu\text{m}$ deep are etched in the gaps along the full length of the resonators, see the inset of Fig. 4.3; this removes the substrate surface from the region with the highest electric field density (black lines in Fig. 4.2a).

The NbTiN resonators with grooves etched in the gaps have significantly higher quality factors, see Fig. 4.3. In the single photon regime, the quality factor has improved from a value of $250 \cdot 10^3$ for the standard design to an intensity-independent plateau value of $350 \cdot 10^3$ for the etched resonators, for $S = 3 \mu\text{m}$ and $W = 2 \mu\text{m}$. Moreover, this increase is a clear indication that the Si surface was the limiting factor also for another reason: the decrease of dielectric has lead to a decrease in the capacitance C in Eq. 4.1. Therefore, if the metal surfaces would dominate the losses, the quality factors would *decrease*. The intensity-independent plateau points towards a single surface dominating loss. With the Si removed, the loss at the single photon level is dominated by the metal surfaces. Determining which surface is complicated by the similarity in dependence on intensity and width (Fig. 4.2). In the many-photon regime the loss is more due to the exposed substrate surface, indicated by the higher quality factors for etched resonators and the high saturation field values. Finally, when increasing the width to $S = 6 \mu\text{m}$ and $W = 2 \mu\text{m}$, the quality factor improves to

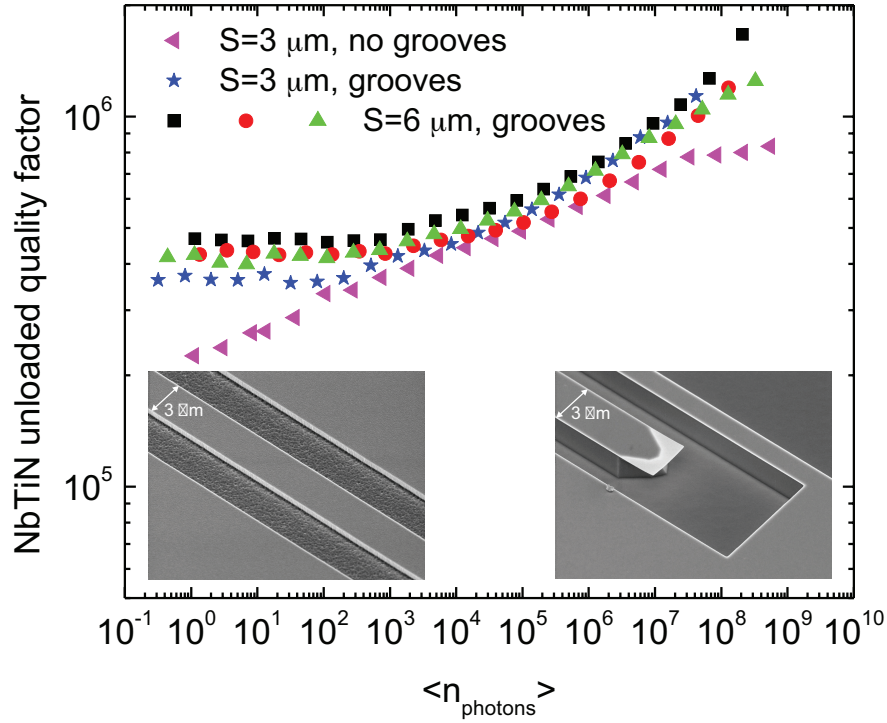


Figure 4.3: The unloaded quality factor versus applied photon number of NbTiN quarterwave resonators with the standard geometry and $S = 3 \mu\text{m}$ and $W = 2 \mu\text{m}$ (\blacktriangleleft) (6.2 GHz), and with grooves etched in the exposed Si substrate with $S = 3 \mu\text{m}$ and $W = 2 \mu\text{m}$ (\star) (4.7 GHz) and $S = 6 \mu\text{m}$ and $W = 2 \mu\text{m}$ at frequencies of 4.2 (\blacksquare), 4.4 (\bullet) and 5.2 GHz (\blacktriangleright). Bath temperature is 60 mK. The left inset is a scanning electron microscope image from the standard coplanar waveguide design, the right inset shows the etched grooves near the open end of the resonator ($S = 3 \mu\text{m}$ in both images). The cross section of the etched resonators is outlined in Fig. 4.2a.

around $450 \cdot 10^3$. This 30 % increase is consistent with our calculation (Fig. 4.2b) and shows that further increases can be obtained by widening the resonator.

With quality factors as high as $470 \cdot 10^3$, we estimate single photon lifetimes of $18 \mu\text{s}$ at 4.2 GHz, one order of magnitude longer than decoherence times measured for superconducting qubits [18, 19]. These long lifetimes make superconducting resonators, as shown in Fig. 4.3, appealing building blocks for a quantum processor, as they can be used as quantum memory elements [20] and for a quantum bus for long-range qubit-qubit coupling [21, 22]. Interestingly, the resonators with grooves also have less frequency noise [23].

4.5 Conclusions

To conclude, we have found NbTiN resonators to have a higher quality factor in the single photon regime than any of the previously studied superconductors, indicating it has a minimal lossy dielectric layer. The losses arise largely due to a surface distribution of two-level systems on the exposed Si substrate. By removing the substrate from the region with highest electric fields the quality factor is increased further, showing that using NbTiN resonators and removing dielectrics is a straightforward route to high quality factors in the single photon regime.

References

- [1] A. Wallraff, D. I. Schuster, A. Blais, L. Frunzio, R.-S. Huang, J. Majer, S. Kumar, S. M. Girvin, and R. J. Schoelkopf, *Strong coupling of a single photon to a superconducting qubit using circuit quantum electrodynamics*, Nature **431**, 162 (2004).
- [2] H. Wang, M. Hofheinz, J. Wenner, M. Ansmann, R. C. Bialczak, M. Lenander, E. Lucero, M. Neeley, A. D. O’Connell, D. Sank, A. N. Weides, M. Cleland, and M. J. M., *Improving the coherence time of superconducting coplanar resonators*, Appl. Phys. Lett. **95**, 233508 (2009).
- [3] A. D. O’Connell, M. Ansmann, R. C. Bialczak, M. Hofheinz, N. Katz, E. Lucero, C. McKenney, M. Neeley, H. Wang, E. M. Weig, A. N. Cleland, and M. J. M., *Microwave dielectric loss at single photon energies and millikelvin temperatures*, Appl. Phys. Lett. **92**, 112903 (2008).
- [4] A. Palacios-Laloy, F. Nguyen, F. Mallet, P. Bertet, D. Vion, and D. Esteve, *Tunable Resonators for Quantum Circuits*, Journal of Low Temperature Physics **151**, 1034 (2008).
- [5] P. Macha, S. H. W. van der Ploeg, G. Oelsner, E. H. Il’ichev, G. S. Meyer, G. Wünsch, and M. Siegel, *Losses in coplanar waveguide resonators at millikelvin temperatures*, Appl. Phys. Lett. **96**, 062503 (2010).
- [6] T. Lindström, J. E. Healey, M. S. Colclough, C. M. Muirhead, and A. Y. Tzalenchuk, *Properties of superconducting planar resonators at millikelvin temperatures*, Phys. Rev. B **80**, 132501 (2009).
- [7] P. K. Day, H. G. LeDuc, B. A. Mazin, A. Vayonakis, and J. Zmuidzinas, *A broadband superconducting detector suitable for use in large arrays*, Nature **425**, 817 (2003).

- [8] R. Barends, H. L. Hortensius, T. Zijlstra, J. J. A. Baselmans, S. J. C. Yates, J. R. Gao, and T. M. Klapwijk, *Contribution of dielectrics to frequency and noise of NbTiN superconducting resonators*, Appl. Phys. Lett. **92**, 223502 (2008).
- [9] R. Barends, *Photon-detecting Superconducting Resonators*, PhD thesis, TU Delft, 2009.
- [10] Applied number of photons: $\langle n_{\text{photons}} \rangle = CV_r^2 l / 2hf$, with $V_r = 2\sqrt{P_{\text{int}}Z}$ the standing wave voltage, P_{int} the internal resonator power [9] and Z the waveguide impedance.
- [11] W. A. Phillips, *Two-level states in glasses*, Reports on Progress in Physics **50**, 1657 (1987).
- [12] J. M. Martinis, K. B. Cooper, R. McDermott, M. Steffen, M. Ansmann, K. D. Osborn, K. Cicak, S. Oh, D. P. Pappas, R. W. Simmonds, and C. C. Yu, *Decoherence in Josephson Qubits from Dielectric Loss*, Phys. Rev. Lett. **95**, 210503 (2005).
- [13] J. Gao, M. Daal, A. Vayonakis, S. Kumar, J. Zmuidzinas, B. Sadoulet, B. A. Mazin, P. K. Day, and G. H. Leduc, *Experimental evidence for a surface distribution of two-level systems in superconducting lithographed microwave resonators*, Appl. Phys. Lett. **92**, 152505 (2008).
- [14] P. P. Silvester and R. L. Ferrari, *Finite elements for electrical engineers*.
- [15] At $T > hf/k$ relaxational absorption can become relevant as well [11]. We therefore use Eq. 4.1 only for the 60 mK data.
- [16] M. Von Schickfus and S. Hunklinger, *Saturation of the dielectric absorption of vitreous silica at low temperatures*, Phys. Lett. A **64**, 144 (1977).
- [17] R. Barends, J. J. A. Baselmans, S. J. C. Yates, J. R. Gao, J. N. Hovenier, and T. M. Klapwijk, *Quasiparticle Relaxation in Optically Excited High-Q Superconducting Resonators*, Phys. Rev. Lett. **100**, 257002 (2008).
- [18] P. Bertet, I. Chiorescu, G. Burkard, K. Semba, C. J. P. M. Harmans, D. P. DiVincenzo, and J. E. Mooij, *Dephasing of a Superconducting Qubit Induced by Photon Noise*, Phys. Rev. Lett. **95**, 257002 (2005).
- [19] A. A. Houck, J. A. Schreier, B. R. Johnson, J. M. Chow, J. Koch, J. M. Gambetta, D. I. Schuster, L. Frunzio, M. H. Devoret, S. M. Girvin, and R. J. Schoelkopf, *Controlling the Spontaneous Emission of a Superconducting Transmon Qubit*, Phys. Rev. Lett. **101**, 080502 (2008).

-
- [20] P. J. Leek, M. Baur, J. M. Fink, R. Bianchetti, L. Steffen, S. Filipp, and A. Wallraff, *Cavity Quantum Electrodynamics with Separate Photon Storage and Qubit Readout Modes*, Phys. Rev. Lett. **104**, 100504 (2010).
- [21] M. A. Sillanpaa, J. I. Park, and R. W. Simmonds, *Coherent quantum state storage and transfer between two phase qubits via a resonant cavity*, Nature **449**, 438 (2007).
- [22] J. Majer, J. M. Chow, J. M. Gambetta, J. Koch, B. R. Johnson, J. A. Schreier, L. Frunzio, D. I. Schuster, A. A. Houck, A. Wallraff, A. Blais, M. H. Devoret, S. M. Girvin, and R. J. Schoelkopf, *Coupling superconducting qubits via a cavity bus*, Nature **449**, 443 (2007).
- [23] R. Barends, N. Verduyssen, A. Endo, P. J. de Visser, T. Zijlstra, T. M. Klapwijk, and J. J. A. Baselmans, *Reduced frequency noise in superconducting resonators*, Appl. Phys. Lett. **97**, 033507 (2010).

Chapter 5

Reduced frequency noise in superconducting resonators

We report a reduction of the frequency noise in coplanar waveguide superconducting resonators. The reduction of 7 dB is achieved by removing the exposed dielectric substrate surface from the region with high electric fields and by using NbTiN. In a model-analysis the surface of NbTiN is found to be a negligible source of noise, experimentally supported by a comparison with NbTiN on SiO_x resonators. The reduction is additive to decreasing the noise by widening the resonators.

This chapter was published as R. Barends, N. Vecruyssen, A. Endo, P. J. de Visser, T. Zijlstra, T. M. Klapwijk, and J. J. A. Baselmans *Applied Physics Letters* 97, 033507 (2010). The main contribution of the present author was in the design of the experiment and the fabrication of the devices.

5.1 Introduction

The development of large and sensitive imaging arrays for far infrared astronomical instrumentation is rapidly progressing with microwave kinetic inductance detectors [1]. Arrays have already been taken to ground-based telescopes [2, 3], and readout using frequency domain multiplexing has been demonstrated [4]. The frequency noise in these superconducting resonators is two to three orders of magnitude above the fundamental limit of generation-recombination noise. The noise has been conjectured to arise from dipole two-level systems (TLS) in surface dielectrics [5], which is supported by recent experiments: The surface has been shown to be a dominant source of noise, by measurements on the width scaling by Gao *et al.* [6]. Moreover, we have shown that introducing dielectrics by covering the resonators with SiO_x leads to an increase in the noise [7]. Noroozian *et al.* showed that the noise arises predominantly from the capacitive portion of the resonator by using a lumped element capacitor [8]. Noise reduction can be achieved by widening the resonator, in essence decreasing the surface to volume ratio [6, 8, 9]. However, the practically limiting source of noise remains to be identified and reduced.

In this chapter we show that the noise can be decreased by minimizing the dielectrics in the resonator itself. The lowest noise is achieved by using NbTiN deposited on top of a hydrogen passivated substrate as well as by removing the substrate from the region with the largest electric fields. The combination of removing the substrate and widening the resonator leads to a reduction of 9 dB for our first-generation resonators.

5.2 Frequency noise due to two level systems

Dipole TLS are known to influence the temperature dependent permittivity ϵ [10], and consequently the resonance frequency. The superposition of permittivity and complex conductivity ($\sigma_1 - i\sigma_2$) controls the resonance frequency [7, 11]

$$\frac{\delta f_0}{f_0} = \frac{\alpha\beta}{4} \frac{\delta\sigma_2}{\sigma_2} - \frac{F}{2} \frac{\delta\epsilon}{\epsilon} \quad (5.1)$$

with α the kinetic inductance fraction and $\beta = 1$ for the thick film and $\beta = 2$ for the thin film limit. The filling factor F [11] takes into account the location of the dielectric and weighs its contribution to the frequency by the electric field energy inside our resonator geometry. It is defined by $F = \frac{1}{2}\epsilon_0\epsilon_h \iiint_{V_h} |\vec{E}(\vec{r})|^2 d\vec{r} / \frac{1}{4}CV_r^2l$, with C the capacitance per unit length, V_r the standing wave voltage, l the

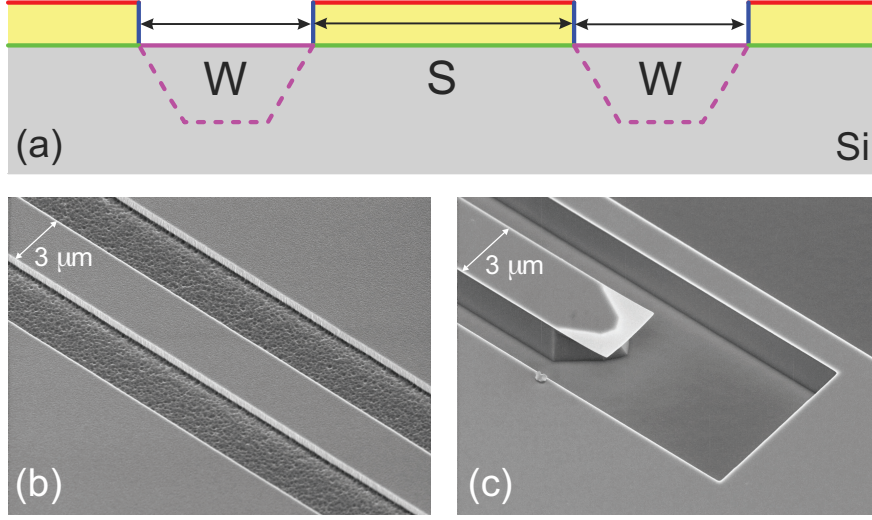


Figure 5.1: (a) The coplanar waveguide with the top metal surface, the exposed substrate, the substrate-metal interface and the etched metal edges outlined. (b) A scanning electron microscope image from the standard resonator design. (c) The etched grooves near the open end of the resonator, its cross section is outlined in (a) (dashed). The central line width is $S = 3 \mu\text{m}$ in both images.

length of the resonator, and ϵ_h the relative permittivity and V_h the volume of the dielectric hosting the TLS.

Similarly, dipole TLS cause frequency noise through the time-varying permittivity $\epsilon(\vec{r}, t)$ [5]. Consequently, the power spectral density of the permittivity $S_\epsilon = 2\epsilon_0^2 F\{\langle \epsilon_h(t)\epsilon_h(t - \tau) \rangle\}$ translates to frequency noise [6],

$$\frac{S_{f_0}}{f_0^2} = \frac{\frac{1}{4} \iiint_{V_h} S_\epsilon |\vec{E}(\vec{r})|^4 d\vec{r}}{(\frac{1}{4} CV_r^2 l)^2} \quad (5.2)$$

with S_{f_0}/f_0^2 the normalized frequency noise.

5.3 Identifying the location of two level systems

In order to identify the contribution of the various surfaces to noise we calculate the effect of a hypothetical surface layer with thickness $t \rightarrow 0$ containing dipole TLS. The electric fields in the coplanar waveguide geometry are calculated using the potential matrix to find the charge density. The approach is detailed in Ref. [12]. We adopt the assumption by Gao *et al.* [6] that the noise spectral density

follows: $S_\epsilon = \epsilon_0^2 \kappa / \sqrt{|E|^2 + E_s^2}$, with E_s the saturation electric field strength, following the saturation of microwave loss due to TLS at high intensities [10].

The hypothetical layer is placed along each of the outlined surfaces in Fig. 5.1a, the exposed substrate surface, the top metal surface, the etched metal edges and the substrate-metal interface. The results are shown in Fig. 5.2a-b. Importantly, the contribution to the frequency noise is about two orders of magnitude larger when the layer is placed on surfaces adjacent to the metal than when placed on the exposed substrate. This is due to the high electric fields close to the metal. Moreover, we find that the noise follows $S_{f_0}/f_0^2 \propto 1/P_{int}^{0.5}$ in the relevant power range, with P_{int} the internal resonator power [13]. In addition, when widening the resonator geometry the noise decreases. We have also calculated the influence of a metal surface dielectric with finite thickness t on the noise as well as the frequency shift, i.e. Eq. 5.1 and Eq. 5.2. We find that for the noise, only the first few nanometers matter, whereas the full volume influences the frequency shift. This is consistent with our previous experiments, where we showed that frequency deviations arise from the bulk of the dielectric while noise arises predominantly at surfaces and interfaces [7]. The difference arises from the surface layer being weighed by $|\vec{E}(\vec{r})|^4$ for the noise and $|\vec{E}(\vec{r})|^2$ for the frequency shift. Interestingly, the power and width dependence is very similar for each of the surfaces, and identification of the dominant noise source can be done only by removing or altering a specific surface.

5.4 Two level systems in NbTiN resonators

In order to identify and reduce the dominant noise source, we have fabricated a series of devices aimed at addressing a specific surface, see Fig. 5.1. We use NbTiN quarterwave coplanar waveguide resonators [1, 7] with varying geometry or composition. Resonance frequencies lie between 3-5 GHz. As a reference a 300 nm NbTiN film is DC sputtered on an HF-cleaned high resistivity (> 1 k Ω cm) $\langle 100 \rangle$ -oriented Si wafer. Patterning is done using SF₆/O₂ reactive ion etching. The critical temperature is $T_c=14.8$ K, the low temperature resistivity is $\rho=170$ $\mu\Omega$ cm and the residual resistance ratio is 0.94. To identify the importance of using hydrogen passivated Si, a 300 nm NbTiN film has been deposited on the native oxide of Si ($T_c = 15.5$ K, $\rho = 84$ $\mu\Omega$ cm and $RRR = 1.0$). We have also removed the exposed substrate surface from the region with large electric fields: fully straight, 50 nm thick, NbTiN resonators are made on Si, aligned along the $\langle 110 \rangle$ axis of the Si substrate ($T_c = 13.6$ K, $\rho = 142$ $\mu\Omega$ cm and $RRR = 0.96$). Using KOH wet etching, 0.9 μ m deep grooves (dashed lines in Fig. 5.1a) are

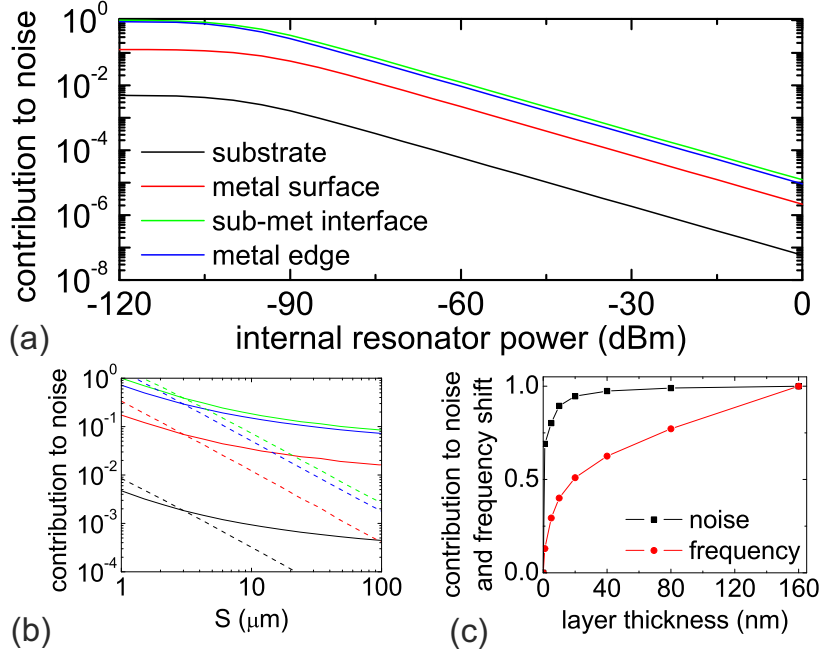


Figure 5.2: (a) The power dependence of the normalized contribution to noise using Eq. 5.2, for a TLS distribution placed on the exposed substrate surface, top metal surface, substrate-metal (sub-met) interface and etched metal edges ($E_s = 5$ kV/m, see Ref. [12]). (b) The normalized contribution to noise of the dielectric layers versus central line width S , for $W = 2 \mu\text{m}$ (solid) and $W = \frac{2}{3}S$ (dashed). (c) The normalized contribution to noise and frequency shift for a dielectric layer with finite thickness on top of the metal. Calculations are done for $\epsilon_h = 1$.

etched in the gaps along the full length of the resonators. As a reference for the latter sample as well as to clarify the influence of the metal edges, a straight, 50 nm thick NbTiN resonator is made where the Si substrate is not removed.

The frequency noise is measured using a homodyne detection scheme based on quadrature mixing [1, 13, 7]. The samples are cooled to a temperature of 310 mK using a He-3 sorption cooler placed in a 4.2 K liquid He cryostat. The sample stage is magnetically shielded with a superconducting shield. We use a low noise high electron mobility transistor amplifier with a noise temperature of 4 K [14].

The temperature dependence of the resonance frequency is shown in Fig. 5.3. For the NbTiN on SiO_x resonator we find a clear nonmonotonicity. The superposition (Eq. 5.1) of the complex conductivity and logarithmically temperature dependent permittivity describes the data. The logarithmic dependence is consistent with resonant interaction of TLS with the electric fields at $kT > hf$ [10]: $\delta\epsilon/\epsilon = -\ln(T/T_0) 2Np^2/\epsilon$ with N the TLS density of states, p the dipole moment

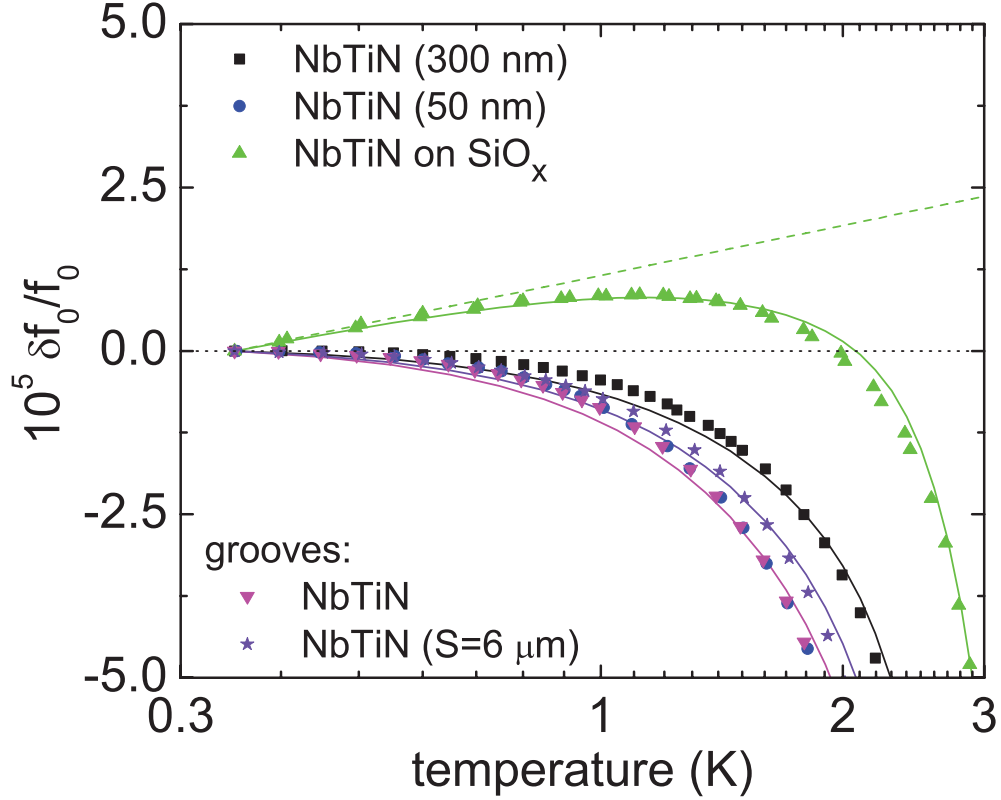


Figure 5.3: The temperature dependence of the fractional resonance frequency. The solid lines are fits using Eq. 5.1, using Mattis-Bardeen. The NbTiN on SiO_x data follow a superposition of a logarithmically temperature dependent permittivity (dashed line) and Mattis-Bardeen (Eq. 5.1). We choose $T_0 = 350$ mK.

and T_0 an arbitrary reference temperature. The temperature dependence of the other resonators follows Mattis-Bardeen [15], provided a broadening parameter [16] of $\Gamma = 15 - 20 \mu\text{eV}$ is included in the density of states [17].

The frequency noise spectra are shown in Fig. 5.4. The inset shows the dependence on the internal resonator power P_{int} . The noise spectra follow $S_{f_0}/f_0^2 \propto 1/f^{0.3-0.6}$, until a roll-off frequency on the order of 10 kHz. This roll-off arises from the resonator-specific response time, set by the loaded quality factor and resonator frequency. The NbTiN on SiO_x resonator has the highest frequency noise, at $P_{int} = -30$ dBm: S_{f_0}/f_0^2 (1 kHz) = -195 dBc/Hz. This is 3 dB noisier than the standard, 300 nm thick, NbTiN resonator which has a noise level of -198 dBc/Hz. The noise remains at -198 dBc/Hz when decreasing the metal thickness by a factor of 6 (8 dB), from 300 nm to 50 nm. Clearly, the noise is decreased with 7 dB for the resonator with grooves in the gaps, having S_{f_0}/f_0^2 (1 kHz) = -205 dBc/Hz. Moreover, the noise is reduced over the

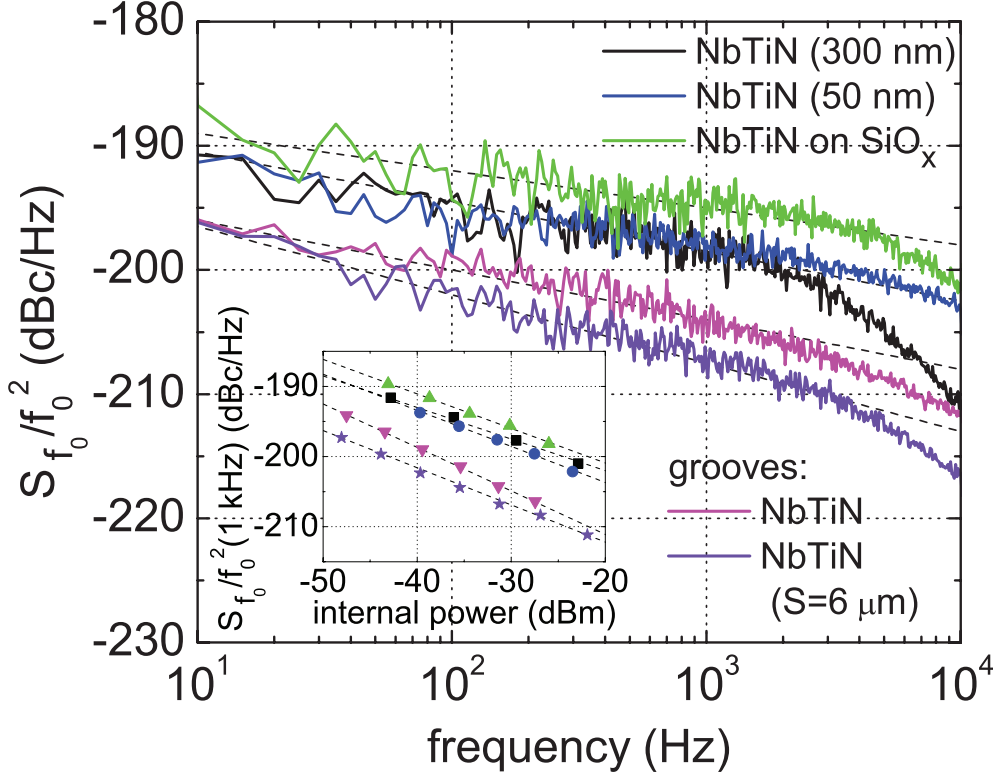


Figure 5.4: The normalized frequency noise spectra of NbTiN, NbTiN on SiO_x and NbTiN with grooves etched in the gaps. The widths are $S = 3 \mu\text{m}$, $W = 2 \mu\text{m}$ except for the wide resonator with grooves: $S = 6 \mu\text{m}$, $W = 2$. The bath temperature is 310 mK and the internal resonator power is $P_{int} \approx -30$ dBm. The inset shows the power dependence, see Fig. 5.3 for the legend. Dashed lines are fits to the spectral shape and power dependence.

whole range of spectral frequency and internal resonator power. For the wider resonator with $S = 6 \mu\text{m}$ the noise is 2 dB lower at -207 dBc/Hz. We find that the frequency noise follows $S_{f_0}/f_0^2 \propto 1/P_{int}^{0.4-0.6}$, up to powers of $P_{int} \sim -25$ dBm.

The data and analysis show that NbTiN is a clean material and point towards SiO_x as the dominant source of noise. First, the exposed Si surface dominates the noise as its removal decreases the noise considerably. Second, when placing SiO_x below or on top of NbTiN the noise increases (Fig. 5.4 and Ref. [7]). Third, the analysis in Fig. 5.2 indicates that the NbTiN surface is clean compared to that of Si, as the metal surfaces influence the noise more strongly than the exposed substrate. In addition, the monotonic temperature dependence of the resonance frequency down to 350 mK indicates that NbTiN has a minimal dielectric layer, in contrast to Nb, Ta and Al [7] as well as NbTiN on SiO_x . Moreover, the metal edges are not dominant, as the noise level is independent of the thickness of the

metal. Finally, the removal of dielectrics from the gaps leads to a decrease in the capacitance C in Eq. 5.2. Hence, if the metal surfaces dominate, the noise would *increase*. Quantitatively, we estimate $\kappa(1 \text{ kHz}) \approx 5 \cdot 10^{-27} \text{ 1/Hz}$ for SiO_x , assuming $t = 3 \text{ nm}$. Importantly, the noise reduction is significant: it is 7 dB below our standard NbTiN on Si resonators and 11 dB below the lowest values reported for coplanar waveguide resonators by Gao *et al.* [5]. In addition, the noise is 2 dB lower when widening to $S = 6 \text{ }\mu\text{m}$, which is consistent with our calculation (1.9 dB, see Fig. 5.2b) and shows that further improvements can be obtained by widening the resonator.

5.5 Optimized geometry for minimal frequency noise

A particular approach to remove the substrate was followed in Ref. [18] using Al on Si resonators. By etching the substrate isotropically, the noise was reduced to a level of $S_{f_0}/f_0^2 (1 \text{ kHz}) = -189 \text{ dBc/Hz}$ at maximum power. Due to the undercut the influence of the exposed substrate surface as well the substrate-metal interface on the noise could not be distinguished.

The data in Fig. 5.4 provide a clear guide to low noise superconducting resonators, by using NbTiN and removing the exposed substrate surface from the region with the largest electric fields. Importantly, we show that both the removal of dielectrics as well as the widening of the resonator leads to a significant decrease of the noise. Hence, both approaches can be considered to be additive to decreasing the noise. Our approach can be implemented for lumped element resonators [19, 8] as well: by using a $\langle 100 \rangle$ -oriented Si wafer and aligning the fingers and edges of the interdigitated capacitor along the two perpendicular $\langle 110 \rangle$ axes, grooves can be etched with a minimal amount of undercut. Interestingly, our resonators with grooves etched in the gaps also have higher quality factors at high internal power levels as well as at the single microwave photon levels needed for circuit quantum electrodynamics [12].

5.6 Conclusion

To conclude, we have reduced the frequency noise by using NbTiN and removing the substrate from the region with the highest electric fields. This indicates that the exposed Si substrate surface is the main source of the noise, hence the contribution to noise from the NbTiN surface is not dominant. The followed

approach is a straightforward route to low frequency noise in superconducting resonators.

References

- [1] P. K. Day, H. G. LeDuc, B. A. Mazin, A. Vayonakis, and J. Zmuidzinas, *A broadband superconducting detector suitable for use in large arrays*, *Nature* **425**, 817 (2003).
- [2] A. Monfardini et al., *NIKA: A millimeter-wave kinetic inductance camera*, *Astron & Astrophys.* **521**, A29 (2010).
- [3] J. Schlaerth, A. Vayonakis, P. K. Day, J. Glenn, J. Gao, S. Golwala, S. Kumar, H. LeDuc, B. A. Mazin, J. Vaillancout, and J. Zmuidmizas, *A millimeter and submillimeter kinetic inductance detector camera*, *J. of Low Temp. Phys.* **151**, 684 (2008).
- [4] S. J. C. Yates, A. M. Baryshev, J. J. A. Baselmans, B. Klein, and R. Güsten, *Fast Fourier transform spectrometer readout for large arrays of microwave kinetic inductance detectors*, *Applied Physics Letters* **95**, 042504 (2009).
- [5] J. Gao, J. Zmuidzinas, B. A. Mazin, H. G. LeDuc, and P. K. Day, *Noise properties of superconducting coplanar waveguide microwave resonators*, *Applied Physics Letters* **90**, 102507 (2007).
- [6] J. Gao, M. Daal, J. M. Martinis, A. Vayonakis, J. Zmuidzinas, B. Sadoulet, B. A. Mazin, P. K. Day, and H. G. LeDuc, *A semiempirical model for two-level system noise in superconducting microresonators*, *Applied Physics Letters* **92**, 212504 (2008).
- [7] R. Barends, H. L. Hortensius, T. Zijlstra, J. J. A. Baselmans, S. J. C. Yates, J. R. Gao, and T. M. Klapwijk, *Contribution of dielectrics to frequency and noise of NbTiN superconducting resonators*, *Appl. Phys. Lett.* **92**, 223502 (2008).
- [8] O. Nooroziyan, J. Gao, J. Zmuidzinas, H. LeDuc, and B. A. Mazin, *Two-level system noise reduction for Microwave Kinetic Inductance Detectors*, *AIP Conf. Proc.* **1185**, 148 (2009).
- [9] R. Barends, H. L. Hortensius, T. Zijlstra, J. J. A. Baselmans, S. J. C. Yates, J. Gao, and T. Klapwijk, *Noise in NbTiN, Al, and Ta Superconducting Resonators on Silicon and Sapphire Substrates*, *Applied Superconductivity, IEEE Transactions on* **19**, 936 (2009).

- [10] W. A. Phillips, *Two-level states in glasses*, Reports on Progress in Physics **50**, 1657 (1987).
- [11] J. Gao, M. Daal, A. Vayonakis, S. Kumar, J. Zmuidzinas, B. Sadoulet, B. A. Mazin, P. K. Day, and G. H. Leduc, *Experimental evidence for a surface distribution of two-level systems in superconducting lithographed microwave resonators*, Appl. Phys. Lett. **92**, 152505 (2008).
- [12] R. Barends, N. Verduyssen, A. Endo, P. J. de Visser, T. Zijlstra, T. M. Klapwijk, P. Diener, S. J. C. Yates, and J. J. A. Baselmans, *Minimal resonator loss for circuit quantum electrodynamics*, Applied Physics Letters **97**, 023508 (2010).
- [13] R. Barends, *Photon-detecting Superconducting Resonators*, PhD thesis, TU Delft, 2009.
- [14] N. Wadefalk, A. Mellberg, I. Angelov, M. Barsky, S. Bui, E. Choumas, R. Grundbacher, E. Kollberg, R. Lai, N. Rorsman, P. Starski, J. Stenarson, D. Streit, and H. ZIRATH, *Cryogenic wide-band ultra-low-noise IF amplifiers operating at ultra-low DC power*, Microwave Theory and Techniques, IEEE Transactions on **51**, 1705 (2003).
- [15] D. C. Mattis and J. Bardeen, *Theory of the Anomalous Skin Effect in Normal and Superconducting Metals*, Phys. Rev. **111**, 412 (1958).
- [16] R. C. Dynes, V. Narayanamurti, and J. P. Garno, *Direct Measurement of Quasiparticle-Lifetime Broadening in a Strong-Coupled Superconductor*, Phys. Rev. Lett. **41**, 1509 (1978).
- [17] *For 300 nm thick NbTiN, NbTiN on SiO_x, and 50 nm thick NbTiN we find for $\alpha\beta/4$: 0.18, 0.08 and 0.33, respectively. We infer a magnetic penetration depth λ of 400, 240 and 270 nm.*
- [18] B. A. Mazin, *Microwave kinetic inductance detectors*, PhD thesis, California Institute of Technology, 2008.
- [19] S. Doyle, P. Mauskopf, J. Naylon, A. Porch, and C. Duncombe, *Lumped Element Kinetic Inductance Detectors*, Journal of Low Temperature Physics **151**, 530 (2008).

Chapter 6

Substrate-dependent quasiparticle recombination time in superconducting resonators

We demonstrate an increased quasiparticle recombination time in superconducting resonators on a SiN_x membrane, compared to identical resonators on a SiN_x/Si wafer. An interpretation is given using a thermal model of the membrane. Using an array of tunnel junctions to cool or heat the membrane, we show that the resonators on the membranes are extremely sensitive to small changes of the phonon temperature, which renders them excellent phonon thermometers with a noise level equivalent to $5 \mu\text{K}/\sqrt{\text{Hz}}$. The experimental set-up is in principle an ideal platform to study the interplay of the quasiparticle and phonon populations in superconductors.

This chapter was published as N. Vercruyssen, R. Barends, T. M. Klapwijk, J. T. Muhonen, M. Meschke, and J. P. Pekola *Applied Physics Letters* 99, 062509 (2011).

6.1 Introduction

Superconducting devices for space astronomy and quantum computation are operated at temperatures below 300 mK. At those low temperatures it is usually assumed that the electronic system of the superconductor reaches the temperature of the environment, leading to a low density of quasiparticles - low enough to minimize loss and the recombination rate, and to maximize the coherence time in qubits. In practice it has been found that the quasiparticle density is higher than what can be expected based on the temperature alone [1]. In addition, in many experiments the recombination rate is influenced by the interaction with the phonons, as has been analyzed early on in the context of laser-pulse experiments by Rothwarf and Taylor [2]. We report on the development of a platform to study the interplay between phonons and electrons, which enables a comparison of resonators on different support structures as well as a possibility to add phonons (heating) or remove phonons (cooling) from the material interacting with the resonator.

6.2 Samples

A SiN_x membrane [3] of thickness 100 nm and macroscopic area of $1 \times 1 \text{ mm}^2$ is equipped with two Al quarterwave superconducting resonators (light square in Fig. 6.1a with resonators (yellow), schematic cross section in Fig. 6.1c). Four resonators are located on the full SiN_x/Si wafer, consisting of 100 nm SiN_x on 200 μm Si. The resonators are patterned by electron beam lithography (EBL) and a chlorine reactive ion etch, after sputter deposition of a 100 nm thick Al film.

The samples are measured in a He-3 sorption fridge with a base temperature of 300 mK. Measurements on all six resonators are performed simultaneously with a single feed line, to which the resonators are capacitively coupled. The transmission S_{21} is measured with a signal generator, a low noise cold amplifier, a quadrature mixer, and an analog to digital converter [4]. Through the kinetic inductance of the superconducting condensate, the resonant frequency f_0 of each resonator depends on the Cooper pair density and hence on variations in the number of quasiparticles δn_{qp} , ($kT \ll \Delta$):

$$\frac{\delta f}{f_0} = -\frac{\alpha\beta}{4} \frac{1}{\pi 2N_0 \sqrt{\hbar f \Delta/2}} \delta n_{qp} = R \delta n_{qp}, \quad (6.1)$$

where α is the fraction of the kinetic inductance to the total inductance, β a geometric factor characteristic for the superconducting surface resistance, Δ the

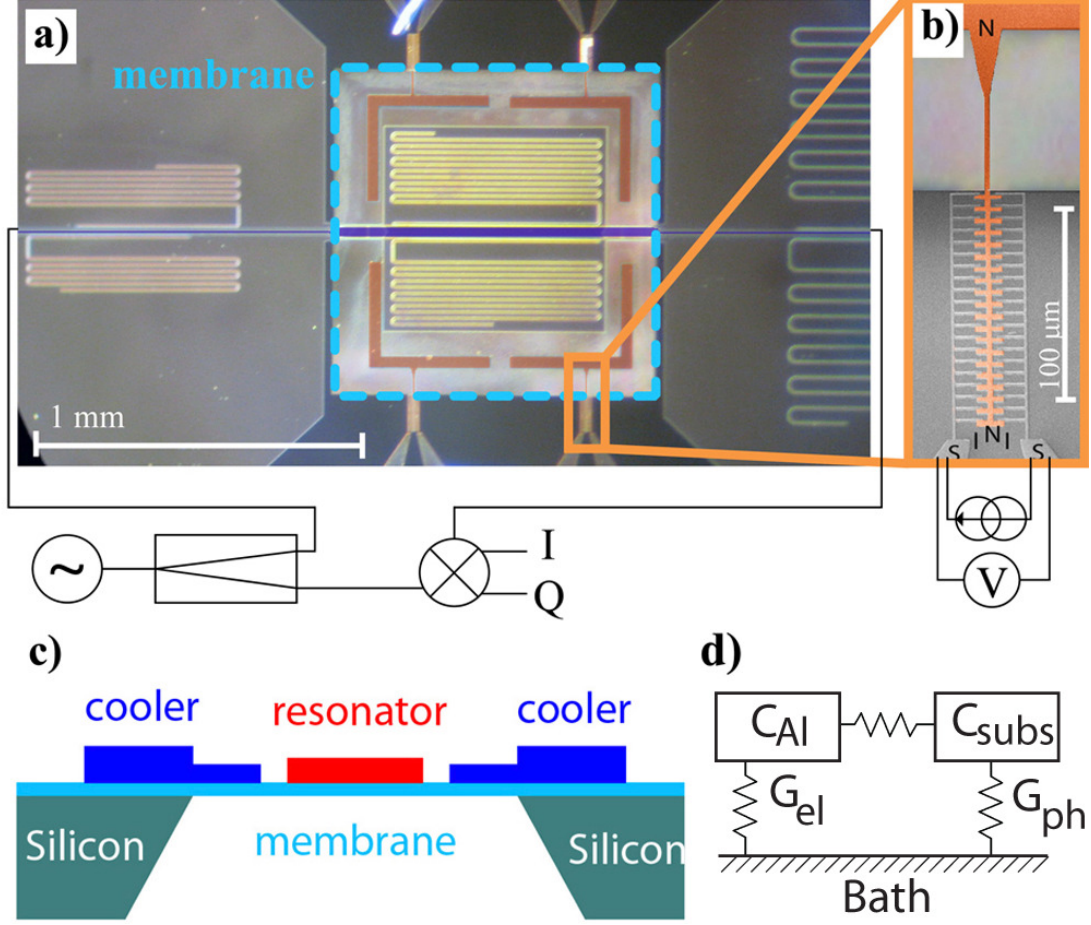


Figure 6.1: (a) Six Al superconducting resonators, of which four are located on the SiN_x/Si wafer and two on a 100 nm thick, 1x1 mm² SiN_x membrane. Four L shaped Cu slabs thermalize the membrane to four junction arrays, each consisting out of 20 SINIS tunnel junctions (b). (c) Schematic cross section of the device layout. (d) Thermal circuit diagram, C_{Al} and C_{subs} are the respective heat capacities of the Al film and the substrate. G_{el} and G_{ph} are the electronic and phononic heat conductances.

superconducting gap, and R the responsivity [4]. The phase θ of S_{21} is a direct measure for the number of quasiparticles through the relation $\delta\theta = -4Q_l \frac{\delta f}{f_0} = -4Q_l R \delta n_{qp}$, with Q_l the loaded quality factor.

6.3 Relaxation times

The inset of Fig. 6.2 shows the real time phase response of the different resonators after optical excitation with a 1.9 eV GaAsP light emitting diode (LED). For small excitations the response is linear and can be characterized by a single

exponential decay time τ_R . As shown in the figure the values of τ_R are an order of magnitude higher for the resonators on the membrane than for the ones on the SiN_x/Si wafer. In addition their dependence on temperature is strikingly different. The relaxation time of the resonators on the membranes increases with increasing temperature, where the resonators on the SiN_x/Si show the opposite temperature dependence.

In previous work [5, 6] relaxation times have been successfully explained in terms of quasiparticle recombination, which predicts a rate proportional to the quasiparticle density and which decreases exponentially at low temperatures [7]:

$$\tau_{rec} = \frac{\tau_0}{\sqrt{\pi}} \left(\frac{kT}{2\Delta} \right)^{5/2} \sqrt{\frac{T_c}{T}} \exp(\Delta/kT). \quad (6.2)$$

The data on the wafer show a similar tendency, although for a typical scattering time for Al of 480 nsec (dashed line Fig. 6.2) the observed times are too long and decay much more slowly with temperature. In this temperature range a similar deviation has been reported recently by De Visser et al. [1], who found a discrepancy between relaxation times inferred from generation-recombination noise measurements and those obtained with the technique used here. Furthermore Barends et al found [5] a similarly strong difference between Al resonators on silicon or on sapphire. It suggests that in using the LED technique at these temperatures the measured τ_R is influenced by the substrate phonons.

For the resonators on the membrane, the magnitude as well as the temperature dependence, make it unlikely that the relaxation is limited by quasiparticle recombination. Enhanced relaxation times can be attributed to reabsorption of 2Δ -phonons emitted during recombination, as described by Rothwarf and Taylor [2]. If the time τ_{esc} for a phonon to escape from the superconducting film exceeds the time τ_{pb} to break a Cooper pair, the quasiparticle recombination time becomes longer and given by $\tau_R = \tau_{rec} (1 + \tau_{pb}/\tau_{esc})$. As τ_{esc} and τ_{pb} are only weakly temperature dependent, the exponential increase of τ_R at low temperatures is preserved. To understand the observed opposite temperature dependence, we propose a thermal description of the resonator and the membrane, qualitatively sketched in Fig. 6.1d. The theoretically expected recombination time is much shorter than the relaxation times measured. Therefore we assume that the phonons in the membrane and the quasiparticles in the resonator are each in equilibrium at their respective temperatures. The relaxation time of the system, membrane and resonators thermally coupled to the support structure, is then given by the ratio of the total thermal capacitance to the thermal conductance: $\tau_R = \frac{C_{th}}{G_{th}}$.

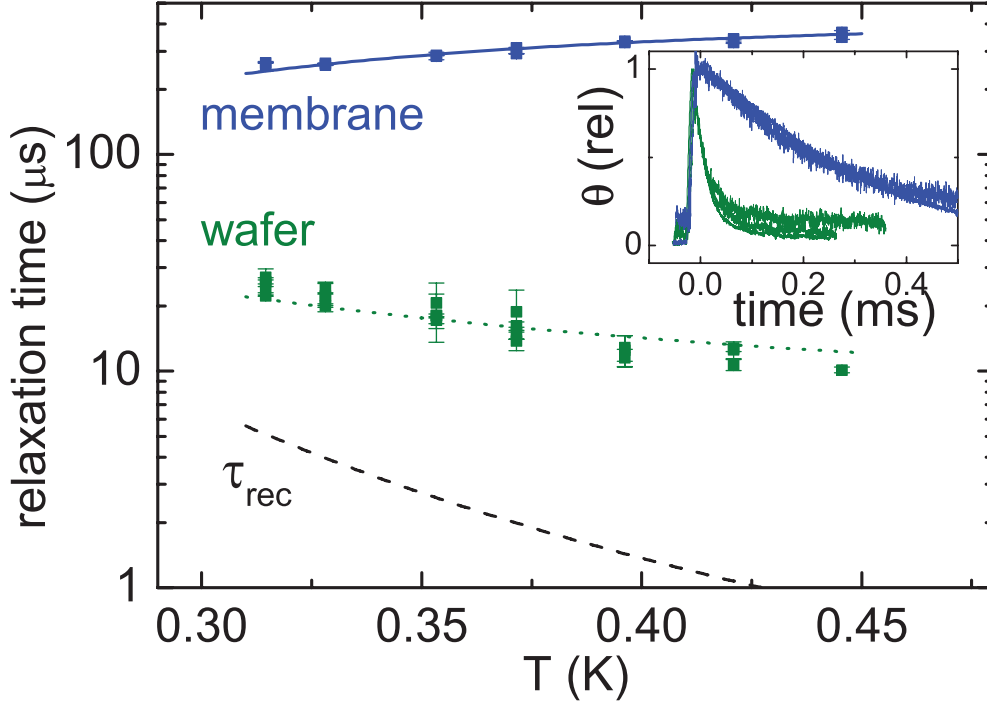


Figure 6.2: Relaxation times of resonators on the membrane and on the SiN_x/Si wafer, the full (blue) and dashed (magenta) lines correspond to a thermal model. The dashed (black) line shows τ_{rec} after Ref. 7 with $\tau_0 = 480$ ns. The relaxation of the resonators after an optical pulse is seen in the real time phase response of the resonators, at a bath temperature of 315 mK (inset).

The heat capacity is dominated by the electronic capacity C_{Al} of the Al film, taken from Phillips [8], which is at the given temperatures three orders of magnitude larger than the one of the Al and SiN_x crystal-lattices. Relaxation happens through two parallel channels: the electronic conductance G_{el} of the Al feed line and the phononic conductance G_{ph} of the membrane. Given the total cross section $S = 8 \mu\text{m}^2$, length $L = 150 \mu\text{m}$ and diffusion constant D of the feed line, we define $G_{el} = DC_{Al}S/A$. To facilitate the calculation of the thermal conductance of the membrane we assume a circular geometry. We find $G_{ph} = \frac{2\pi d}{\ln(r)}\kappa_m$, with $r = 1.35$, the ratio of the membrane radius to the part covered with Al. The heat conductance $\kappa_m = 4T^{2.1} \text{ mW/K}^2$ was measured from a similar membrane with the techniques described by Leivo and Pekola [9]. The result is given by $\tau_R = \frac{C_{Al}}{G_{el}+G_{ph}}$, and shown as a full blue line in Fig. 6.2. The only adjustable parameter is the diffusivity $D = 130 \text{ cm}^2/\text{s}$, in agreement with resistivity measurements of comparable films. Despite the simplicity of the model, the correct magnitude and temperature dependence of τ_R is retrieved, implying that the ther-

mal response of the membrane is the limiting factor in the measurements shown in Fig. 6.2.

We apply an analogous, thermal analysis to the relaxation times measured on the wafer. The heat capacity of the P-doped Si wafer consists of an electronic and a lattice component [10], and dominates over the electronic heat capacity of the Al film, as the wafer is much thicker. Relaxation occurs through the quasiparticles of the Al bondwires, and by phonons escaping through the interface between the wafer and the (cold) sample holder. The electronic contribution G_{el} of the bondwires is modeled as above, for the phononic contribution G_{ph} a Kapitza resistance is used. The resulting relaxation times $\tau_R = \frac{C_{Al} + C_{Si}}{G_{el} + G_{ph}}$ (dashed magenta line in Fig. 6.2) show the thermal model is consistent with the measured data.

6.4 Cooling of the resonator

The above discussion indicates that the phonons of the substrate play a role in the quasiparticle relaxation time of superconducting resonators, both on the membrane as on the SiN_x/Si wafer, though in different strengths. A distinction will have to be made between nonequilibrium phonons in the superconductor itself and phonons in the substrate. In a preliminary attempt we have included in the design the possibility to raise or lower the temperature of the membrane phonons, using an array of superconductor-insulator-normal metal-insulator-superconductor (SINIS) tunnel junctions [11]. We demonstrate that the response of the resonators is very sensitive to heating and cooling of the phonons.

Four arrays of 20 Al/AlO_x/Cu/AlO_x/Al SINIS tunnel junctions each (Fig. 6.1b) are deposited using shadow evaporation through a double resist layer, patterned by EBL. A 20 nm thick Al layer is oxidized *in situ* for 5 min in a pure oxygen atmosphere at a pressure of 4.6 mbar to create the tunnel barrier, and covered with a 50 nm Cu top layer. Four massive L-shaped Cu slabs are located on the membrane (orange in Figs. 6.1a and 6.1b) to thermalize the membrane phonons to electrons of the junction.

Using a battery-powered current bias we measure the current voltage characteristic (IV) of the junction array. Due to fast electron-electron interactions the Cu electrons are assumed to be in quasi-equilibrium with a temperature T_N . The current is then given by

$$2eR_n I = \int dE N(E) [f_N(E + eV/2, T_N) - f_N(E - eV/2, T_N)], \quad (6.3)$$

where R_n is the normal state resistance, f_N the superconducting density of states, and f_N the occupation number of the normal metal electrons. Due to the super-

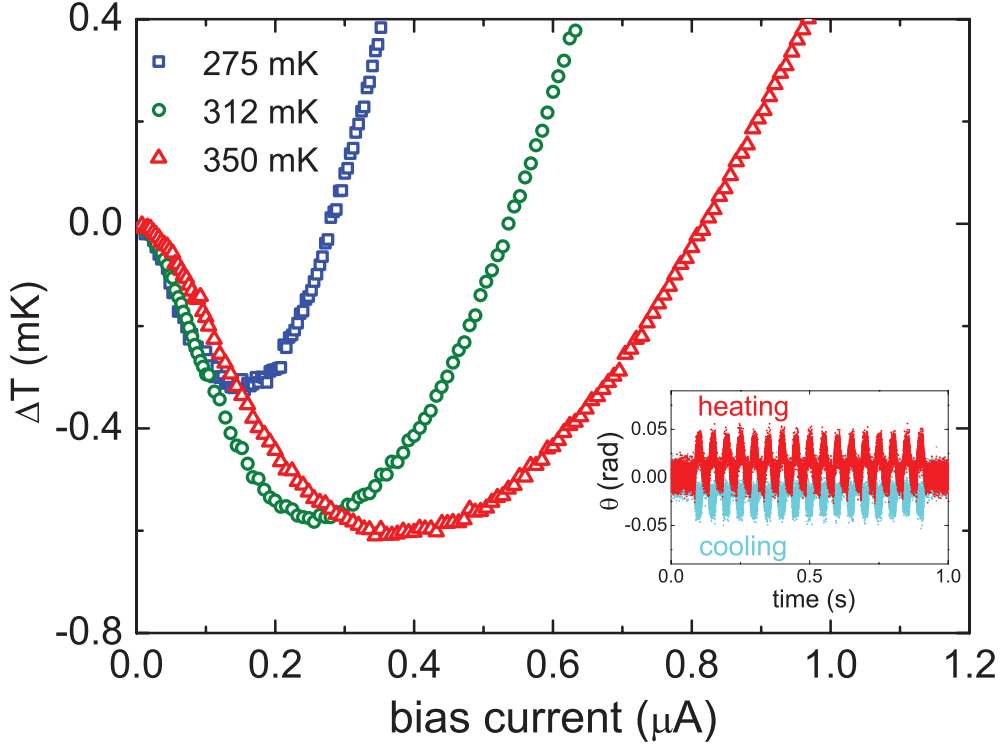


Figure 6.3: The temperature difference of the superconducting resonator versus the bias currents of the junction array, at three different bath temperatures. The inset shows the real time phase response θ of the resonator to two different biases, modulated with a 20 Hz square wave.

conducting gap, only electrons with an energy higher than $E > \Delta - eV/2$ can tunnel out of the normal metal. At low voltages $eV < 2\Delta$ this results in cooling of the normal metal electrons. At higher voltages pair breaking becomes possible with heating as a result. The temperature T_N can be obtained from the measured IV using Eq. 6.3, with $R_n = 18.3 \Omega$ and $\Delta = 205 \mu eV$.

Fig. 6.3 shows the temperature of the resonator on the membrane as a function of the bias current applied to the junctions, at three different bath temperatures. Cooling and heating of the resonator is clearly observed, with a maximum cooling of 0.6 mK (corresponding to 10 mK at the junction, at a voltage $V \approx 0.25$ mV [12]). The fact that we observe quasiparticle cooling of the resonators indicates that the membrane phonons mediate the cooling of the junction.

The temperature of the resonator is inferred from the phase response (inset Fig. 6.3), using $\delta\theta = -4Q_l R \delta n_{qp}$ and $n_{qp} = 2N^a(0) \sqrt{2\pi kT \Delta} e^{-\Delta/kT}$. The high quality factors $Q_l \approx 10^4 - 10^6$ make these resonators extremely sensitive, as can

be seen from the accuracy with which temperature differences smaller than a mK can be measured. To quantify this we calculate which temperature difference generates a signal equal to the system noise: $S_{\Delta T} = S_{Noise}$. For phase read out this is equivalent to $\frac{d\theta}{dT}\Delta T = \Delta\theta_{Noise}$. At an integration time of one second this gives an equivalent temperature difference of $\Delta T < 5 \mu\text{K}$. This demonstrates the potential of resonators as sensitive thermometers, suitable for time resolved measurements, analogous to recent results for detection of phonons generated by cosmic rays [13].

6.5 Conclusions

In conclusion, we experimentally studied the interplay between phonon and quasiparticle nonequilibrium in a superconducting resonator. We have demonstrated that the relaxation times of resonators on a SiN_x membrane are an order of magnitude higher than the ones on the SiN_x/Si wafer. We have also shown that the response of the resonators is very sensitive to the phonon bath of the membrane, of which we electronically changed the temperature. Ideally, it should also be possible to include SIS tunnel junctions to generate not just a thermal phonon distribution but also preferentially 2Δ -phonons from recombination [14]. This work has been supported by EPSRC grant EP/F040784/1 and the European Communitys FP7 Programme under Grant Agreements No. 228464 (MICROKELVIN, Capacities Specific Programme).

References

- [1] P. J. de Visser, J. J. A. Baselmans, P. Diener, S. J. C. Yates, A. Endo, and T. M. Klapwijk, *Number Fluctuations of Sparse Quasiparticles in a Superconductor*, Phys. Rev. Lett. **106**, 167004 (2011).
- [2] A. Rothwarf and B. N. Taylor, *Measurement of Recombination Lifetimes in Superconductors*, Phys. Rev. Lett. **19**, 27 (1967).
- [3] Low stress SiN_x membranes of high mechanical quality where purchased from Norcada Inc. Edmonton, Canada.
- [4] R. Barends, *Photon-detecting Superconducting Resonators*, PhD thesis, TU Delft, 2009.
- [5] R. Barends, J. J. A. Baselmans, S. J. C. Yates, J. R. Gao, J. N. Hovenier, and T. M. Klapwijk, *Quasiparticle Relaxation in Optically Excited High-Q Superconducting Resonators*, Phys. Rev. Lett. **100**, 257002 (2008).

-
- [6] A. V. Timofeev, C. P. García, N. B. Kopnin, A. M. Savin, M. Meschke, F. Giazotto, and J. P. Pekola, *Recombination-Limited Energy Relaxation in a Bardeen-Cooper-Schrieffer Superconductor*, Phys. Rev. Lett. **102**, 017003 (2009).
- [7] S. B. Kaplan, C. C. Chi, D. N. Langenberg, J. J. Chang, S. Jafarey, and D. J. Scalapino, *Quasiparticle and phonon lifetimes in superconductors*, Phys. Rev. B **14**, 4854 (1976).
- [8] N. E. Phillips, *Heat Capacity of Aluminum between 0.1° K and 4.0° K*, Phys. Rev. **114**, 676 (1959).
- [9] M. M. Leivo and J. P. Pekola, *Thermal characteristics of silicon nitride membranes at sub-Kelvin temperatures*, APL **72**, 1305 (1998).
- [10] P. H. Keesom and G. Seidel, *Specific Heat of Germanium and Silicon at Low Temperatures*, Phys. Rev. **113**, 33 (1959).
- [11] F. Giazotto, T. T. Heikkilä, A. Luukanen, A. M. Savin, and J. P. Pekola, *Opportunities for mesoscopics in thermometry and refrigeration: Physics and applications*, Rev. Mod. Phys. **78**, 217 (2006).
- [12] The limited cooling is probably due to imperfect thermalisation of the superconducting leads.
- [13] L. J. Swenson, A. Cruciani, A. Benoit, M. Roesch, C. Yung, A. Bideaud, and A. Monfardini, *High-speed phonon imaging using frequency-multiplexed kinetic inductance detectors*, APL **96**, 263511 (2010).
- [14] W. Eisenmenger, *Tunneling Phenomena in Solids*, Plenum Press, New York, 1969.

Chapter 7

Possibility of enhanced cooling by using uniform AlN tunnel barriers

We study the influence of the lateral uniformity of a tunnel barrier on the cooling performance of superconducting microrefrigerators. Even small variations in transparency deteriorate the cooling efficiency, primarily at low temperatures. We demonstrate reproducible fabrication of Nb based superconducting junctions, using highly transparent AlN barriers ($R_n A \approx 10 \Omega \mu\text{m}^2$). We observe signatures of a strong non-equilibrium distribution of the electrons in the normal island, due to the high current densities. We develop a theoretical framework to include the effect on the thermal behavior of the junction, which allows us to estimate the barrier uniformity based on our experimental results.

7.1 Introduction

Microrefrigeration based on normal-metal superconductor tunnel junctions (NIS) has developed into a mature field over the last decades [1, 2, 3]. A standing question in these junctions is the origin of subgap currents and its influence on the cooling performance of the junction. Possible causes for these subgap currents are subgap states in the superconductor [4], environment-assisted tunneling [5], and Andreev reflections [6].

To increase the cooling power at relatively high temperatures, highly transparent junctions are favorable [7]. However, commonly used AlO_x tunnel barriers are known to be laterally inhomogeneous, possibly due to the presence of defects or variations in the thickness of the barrier [8, 9, 10]. Although the average junction transparencies $D \approx 10^{-4}$ is low, the presence of small regions with a transparency close to $D \approx 1$ leads to Andreev reflection, a second order tunneling process proportional to D^2 , which deteriorates the cooling power of the junction. In superconductor insulator superconductor junctions, a sharp decrease in barrier quality is observed for highly transparent junctions (with a resistance area product below $R_n A \leq 15 \text{ } \Omega \mu\text{m}^2$) [11]. Therefore it might be advantageous to use the more uniform AlN as a barrier material [12].

In this chapter we study the influence of a real tunnel barrier on the charge and energy transport in NIS junctions. We include variations of the barrier width using a distribution of transparencies $\rho(D)$. We demonstrate that even for relatively thick tunnel barriers the presence of small variations in barrier thickness can suppress any cooling effect. The reason for this is the exponential dependence of the transparency on the barrier thickness. In highly transparent barriers these variations are most visible. We therefore address experimentally high-current-density Nb-based tunnel junctions, with AlN as barrier material. We study both planar and stacked junction configurations. The planar geometry gives the most reproducible results and allows us to assess the intrinsic quality of the barrier. The stacked configuration is technologically more challenging, and gives less reproducible results. In samples which show a good quality we obtain similar results to the planar junctions. Due to the reduced volume, we observe signatures of a strong non-equilibrium electron distribution of the normal island.

7.2 Influence of uniformity

The working principle of solid-state refrigerators (Fig. 7.1) is based on the fact that electrons not only carry charge, but also energy. This can result in a net energy current which cools one region, while heating another. In a biased normal

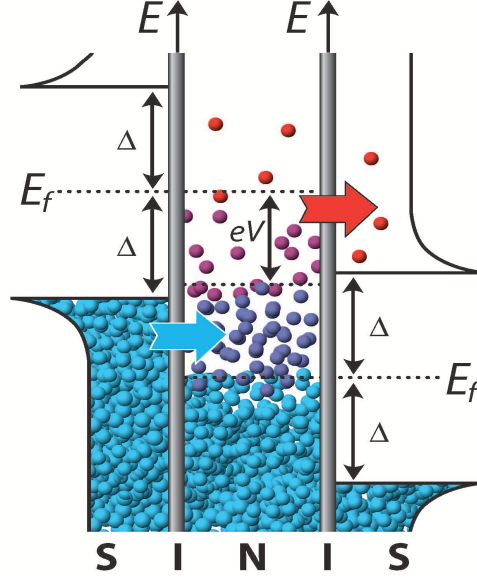


Figure 7.1: Schematic representation of the working principle of a SINIS microrefrigerator. Due to the spectral energy gap of the superconductor, only hot electrons can tunnel out of the normal island, effectively cooling it. The use of a double NIS junction enhances the efficiency of the cooler.

metal superconductor tunnel junction the voltage is assumed to drop over the barrier, and the charge current arises due to elastic tunneling of quasiparticles. The tunneling rate is proportional to the transmissivity D of the barrier and to the density of quasiparticle states (dos) in the electrodes. The presence of a gap Δ in the dos $N_s(E) = \text{Re}(|E|/\sqrt{E^2 - \Delta^2})$ of the superconductor inhibits tunneling at energies $E < \Delta$, while tunneling at energies just above the gap $E \geq \Delta$ is enhanced. The net charge current flowing through the barrier is determined by the difference in occupation numbers $f^{n,s}$ of the normal and superconducting electrodes, and is nonlinear due to the energy dependence of N_s :

$$I(V) = \frac{1}{R_n e^2} \int_{-\infty}^{\infty} N_s(E) [f^n(E - eV) - f^s(E)] dE, \quad (7.1)$$

where the combined effect of the density of states and the transmissivity is absorbed in the normal state resistance R_n . In equilibrium the occupation numbers $f^{n,s}$ are given by a Fermi distribution characterized by a temperature T :

$f(E, T) = 1/(1 + \exp(E/k_B T))$ with k_B the Boltzmann constant. Every electron tunneling from the normal metal carries a net energy of $E - eV$, resulting in a net heat flow from the normal metal:

$$\dot{Q}(V) = \frac{1}{R_n e^2} \int_{-\infty}^{\infty} (E - eV) N_s(E) [f^n(E - eV) - f^s(E)] dE. \quad (7.2)$$

At voltages $eV \leq \Delta$ only ‘hot’ electrons with an energy higher than the Fermi energy can tunnel into the superconducting electrode, effectively cooling the normal metal. Note that both the dissipated power $P = IV$ and the net extracted heat $\dot{Q}(V)$ are injected into the superconductor. The cooling power increases for increasing bias voltage, until the voltage is big enough to ‘break’ Cooper pairs $eV > \Delta$ and the normal metal starts to heat.

Based on Eq. (7.2) it seems that a higher transmissivity D automatically leads to a higher cooling power due to a reduced resistance R_n . For high transparencies however, higher order tunneling processes proportional to D^n become important. In contrast to quasiparticle tunneling which cools the normal metal for $eV < \Delta$, these higher order contributions heat the normal metal even at low voltages. This can be understood from Andreev reflection, a second order process in which a normal electron is retroreflected as a hole, while one Cooper pair is added to the superconductor. The Cooper pair is injected exactly at the Fermi energy of the superconductor, and no energy is transferred. In the normal metal, an electron with energy $E - eV$ is extracted and a hole with energy $E + eV$ is added giving a total added heat of $2eV$. To gain qualitative insight in this process we calculate the charge and heat current for barriers with an arbitrary transparency using the approach of Blonder, Tinkham and Klapwijk [13]:

$$\begin{aligned} I_D(V) &= \frac{1}{R_n e} \int_{-\infty}^{\infty} dE \\ & (1 - a - b)[f^n(E - eV) - f^s(E)] + a[f^n(E - eV) - f^n(E + eV)] \\ \dot{Q}_D(V) &= \frac{1}{R_n e} \int_{-\infty}^{\infty} dE (E - eV) \\ & \{(1 - a - b)[f^n(E - eV) - f^s(E)] + a[f^n(E - eV) - f^n(E + eV)]\}. \end{aligned} \quad (7.3)$$

The respective probabilities $a(E, D)$ and $b(E, D)$ for reflection and transmission through the tunnel barrier depend explicitly on the transmissivity of the barrier. The first term in Eq. (7.3) is proportional to $1 - a - b$, and represents the (heat) current associated with first order quasiparticle tunneling. The second term, proportional to a , is associated with the second order tunneling processes (Andreev reflection). In the limit of low transparencies $D \ll 1$ the factor proportional to $a(E, D)$ disappears, while $1 + a - b$ becomes proportional to the BCS

density of states $1 + a - b = DN_s(E)$ and Eqs. (7.1- 7.2) are obtained. In this regime the (energy) current and thus the cooling power does scale linearly with the transparency of the junction.

For higher transparencies Andreev reflection becomes more probable and will eventually dominate the transport. Even if only a small fraction of the charge current is carried by Andreev reflections, the associated heat current can completely suppress cooling. This stems from the fact that the efficiency of quasiparticle cooling is around 20% at best, while the heating through Andreev reflections is 100% effective. This means there is an optimum transparency at which the cooling power is maximized. For increasing bath temperatures this optimum transparency is higher, as the quasiparticle currents are strongly temperature dependent, while the Andreev contribution is not.

In principle one could design a tunnel junction with a transparency near the optimum cooling power. In practice it has become clear that amorphous AlO_x barriers are laterally inhomogeneous. This is not surprising as small variations of the thickness or potential of the barriers result in exponentially big variations of the transparency. In addition, the tunnel barriers have a thickness of only a few atomic layers, which means that the presence of defects or impurities can easily deteriorate the uniformity of the transmission. We take this into account by using a distribution of transparencies $\rho(D)$. The total current and voltage can be calculated by integrating Eq. (7.3) over the distribution of transparencies:

$$I(V) = \int_0^1 I_D(V)\rho(D)dD \quad (7.4)$$

$$\dot{Q}(V) = \int_0^1 \dot{Q}_D(V)\rho(D)dD \quad (7.5)$$

While quasiparticle tunneling is determined by the average transparency $\langle D\rho(D) \rangle$ of the barrier, the second order contribution $\langle D^2\rho(D) \rangle$ is dominated by the highest transparencies. This indicates that a tunnel barrier with a more uniform transparency, though having the same average transparency as a nonuniform barrier, will suffer much less from heating due to Andreev reflections.

To quantify this effect we adopt two different distributions of transparencies. The first is a universal distribution introduced by Schep et al. [14], valid for a short scattering region, and was used successfully to explain the current voltage characteristics of leaky superconducting junctions [15]:

$$\rho(D) = \frac{2\pi}{\hbar} \frac{1}{D^{3/2}(1-D)^{1/2}}. \quad (7.6)$$

The resulting current voltage characteristic and cooling power for a NIS junction is given by the full black lines in Fig. 7.2. This distribution can only be used in

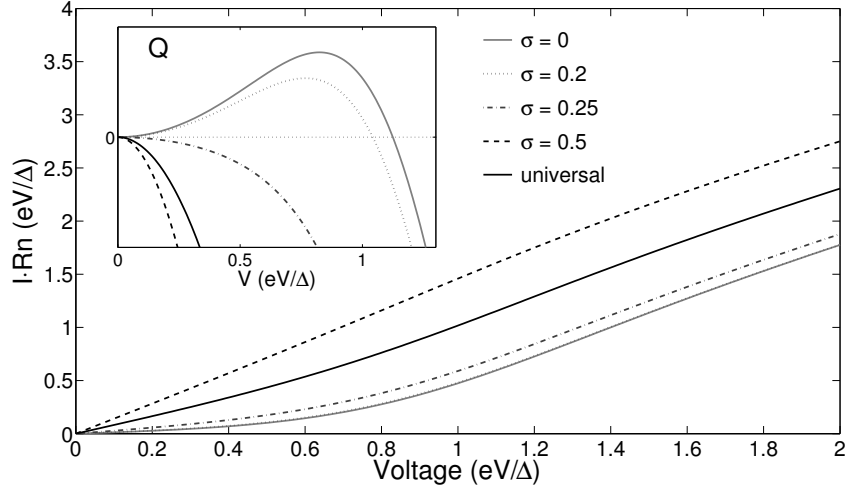


Figure 7.2: Charge and energy (inset) current as a function of applied voltage. The influence of Andreev reflections on the heat current is much more severe than on the charge current.

the limit of very thin tunnel junctions, a regime we wish not to consider as no cooling is observed. Therefore we assume an alternative, Gaussian distribution for the thickness of the tunnel junction:

$$\rho(t) = 1/\sqrt{2\pi} \exp(-(t - t_0)^2/2\sigma^2) + \frac{1}{2} \left[1 - \text{erf}\left(\frac{t_0}{\sqrt{2}\sigma}\right) \right] \delta(t) \quad (t \geq 0) \quad (7.7)$$

For small variations $\sigma \ll t_0$ one can obtain an analytic expression for the average probability for first and second order tunneling:

$$\langle D\rho(D) \rangle = \exp\left(-\alpha\sqrt{\varphi}t_0\left[1 - \frac{\alpha\sqrt{\varphi}}{2}\left(\frac{\sigma}{t_0}\right)^2\right]\right) = D(t_0) \cdot \exp\left(\frac{1}{2}\varphi\left(\frac{\alpha\sigma}{t_0}\right)^2\right) \quad (7.8)$$

$$\langle D^2\rho(D) \rangle = \exp\left(-2\alpha\sqrt{\varphi}t_0\left[1 - \alpha\sqrt{\varphi}\left(\frac{\sigma}{t_0}\right)^2\right]\right) = D(t_0)^2 \cdot \exp\left(2\varphi\left(\frac{\alpha\sigma}{t_0}\right)^2\right) \quad (7.9)$$

where we used $\rho(D)dD = \rho(t)dt$. This results indicates that the barrier can be described with an effective thickness t^* which is somewhat thinner than the average thickness. For the second order processes the thickness is however reduced much more severely than for first order tunneling. The average probability for Andreev reflection is enhanced much stronger in the presence of a non-uniform barrier, compared to quasiparticle tunneling. For arbitrary values of σ, t_0 we calculate the energy and charge currents using Eqs. (7.5) and (7.7).

The effect on the charge and energy transport through the junction is plotted in Fig. 7.2 for different values of σ/t_0 . It can clearly be seen that while the

influence on the IV is quite limited for small σ , the cooling efficiency deteriorates fast. The above discussion neglects the (inverse) proximity effect of the junction. A similar calculation for dirty metals will give qualitatively the same results, though Andreev reflections are enhanced even more in this case due to coherent backscattering near the interface [16, 17, 7].

7.3 Influence of high current densities on the cooling power

In equilibrium the electron occupation numbers of the normal island $f^n(E)$ are given by a Fermi function, and are completely determined by a single temperature T . When the junction is biased, quasiparticles are extracted from the normal island (Fig. 7.1) at a rate $\Gamma(E)$ and the distribution function $f^n(E)$ is modified. Inelastic scattering processes redistribute the energy among the quasiparticles, and tend to restore equilibrium at a timescale $\tau(E)$.

The deviation from equilibrium is characterized by the ratio between the injection rate $\Gamma(E)$ and the relaxation rate $1/\tau(E)$ at a certain energy level. We use a kinetic rate equation to describe the competition between these different processes [18, 19, 20]:

$$\frac{df(E)}{dt} + I_T(E, f(E)) = I_{e-e}^{coll}(E, f(E)) + I_{e-ph}^{coll}(E, f(E)), \quad (7.10)$$

where the spectral injection rate from quasiparticle tunneling I_T is given by the integrand Eq. (7.3). $I_{e,e}^{coll}$ and $I_{e,ph}^{coll}$ are respectively the electron-electron and electron-phonon inelastic collision integrals, which give the energy dependent rates at which electrons are scattered into a certain energy level. The distribution function in the normal island is the result of a detailed balance between the different terms of Eq. (7.10):

$$f^n(E) = \frac{qp_+ f_+^s + qp_- f_-^s + a_+ f_{++}^n + a_- f_{--}^n + I_{e,e}^{coll}(E, \{f^n\}) + I_{e,ph}^{coll}(E, \{f^n\})}{qp_+ + qp_- + a_+ + a_-}, \quad (7.11)$$

where we used short notations qp^\pm for $qp = 1 - a(E \pm eV, D) - b(E \pm eV, D)$, a_\pm for $a(E \pm eV, D)$, and $f_{++,-}^{n,s}$ for $f^{n,s}(E \pm 2eV)$.

To gain insight in Eq. (7.11) we consider some limiting cases. (1) In the case of strong injection (or weak interactions, $\Gamma\tau \gg 1$) the collision terms can be neglected. If second order processes are also neglected qp reduces to DN_s and

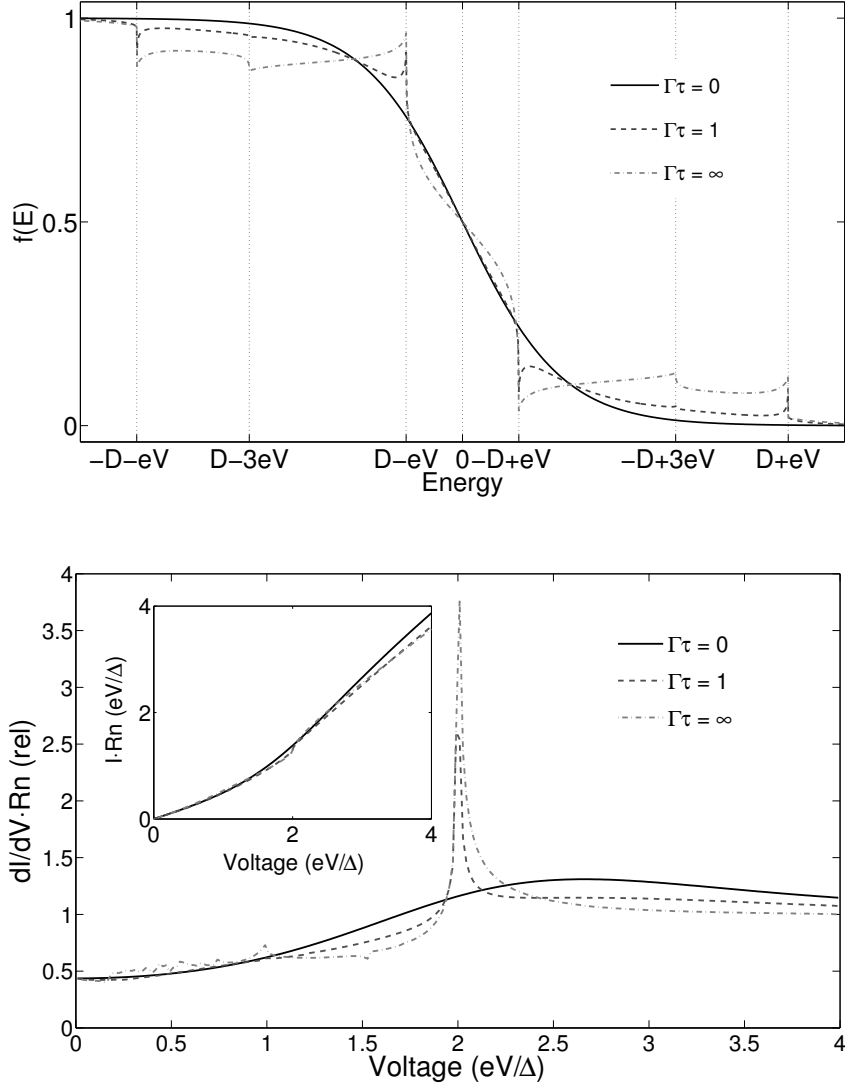


Figure 7.3: (a) The electron distribution function of the normal island for strong ($\Gamma\tau = 0$), intermediate ($\Gamma\tau \approx 1$), and weak ($\Gamma\tau = \infty$) electron-phonon interaction. (b) The effect of the non-equilibrium electron distribution function on the current voltage characteristic.

Eq. (7.11) can be solved exactly:

$$f^n(E) = \frac{N_s(E + eV) \cdot f^s(E + eV) + N_s(E - eV) \cdot f^s(E - eV)}{N_s(E + eV) + N_s(E - eV)}. \quad (7.12)$$

The quasiparticles distribution function is the average of the distribution functions of the superconducting banks, weighted by their density of states. The injection from one bank is exactly balanced by the extraction of the other bank at every energy level. (2) For very strong electron-phonon interaction ($\Gamma\tau \ll 1$)

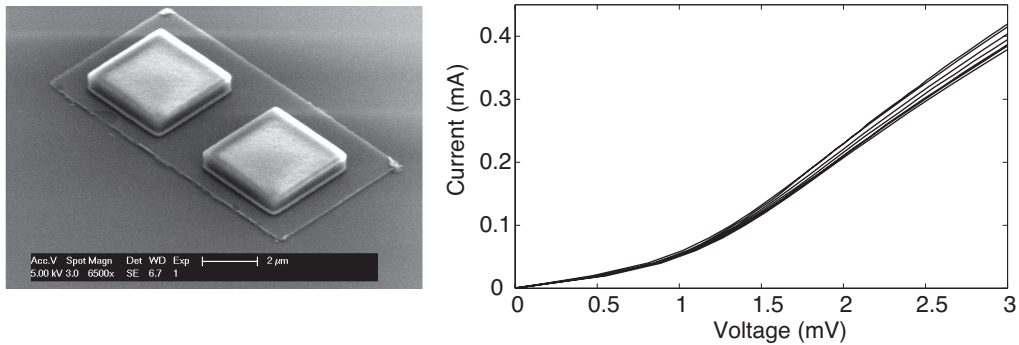


Figure 7.4: (a) SEM picture of a typical device after the definition of the junctions. (b) The current voltage characteristics of six nominally identical junctions

the quasiparticle system stays at the bath temperature. The energy which is extracted or injected from the normal island is compensated by an energy current from the phonons. (3) For strong electron-electron interaction there is no net energy flow into the quasiparticle system. The energy is however redistributed and the quasiparticles adopt a Fermi distribution with a temperature T_n different from the bath temperature. This is referred to as a quasi-thermal distribution.

For arbitrary situations it is necessary to solve Eq. (7.11) numerically. As the injection current depends on the electron occupation numbers of the normal island f^n , this has to be done self-consistently. We adopt a relaxation time approximation for the electron-phonon interaction kernel, in which the electrons relax to the bath temperature on a timescale τ : $I_{eph}^{coll} = (f^n - f_0^n)/\tau$. The results are shown in Fig. 7.3, for a junction biased at $2eV = 1.4\Delta$. When the injection rate is increased compared to the relaxation rate, one observes a depletion of certain electron levels while others are populated with excess quasiparticles. This leads to a deficiency in the current through the junction, compared to the equilibrium case. Peaks in the differential conductance show the onset of (multiple) Andreev reflection at $2eV = \Delta/n$ and quasiparticle tunneling at $2eV = 2\Delta$.

The high current densities might also heat the superconducting electrodes, suppressing the cooling power. This effect has been addressed both theoretically [21] and experimentally [22], and we will not consider it here. The use of normal quasiparticle traps could mitigate the problem [23].

7.4 Planar junctions

Fig. 7.4 shows a typical sample layout. The devices are fabricated using electron beam lithography (EBL) and sputter deposition. First a 20 nm thick Al layer is

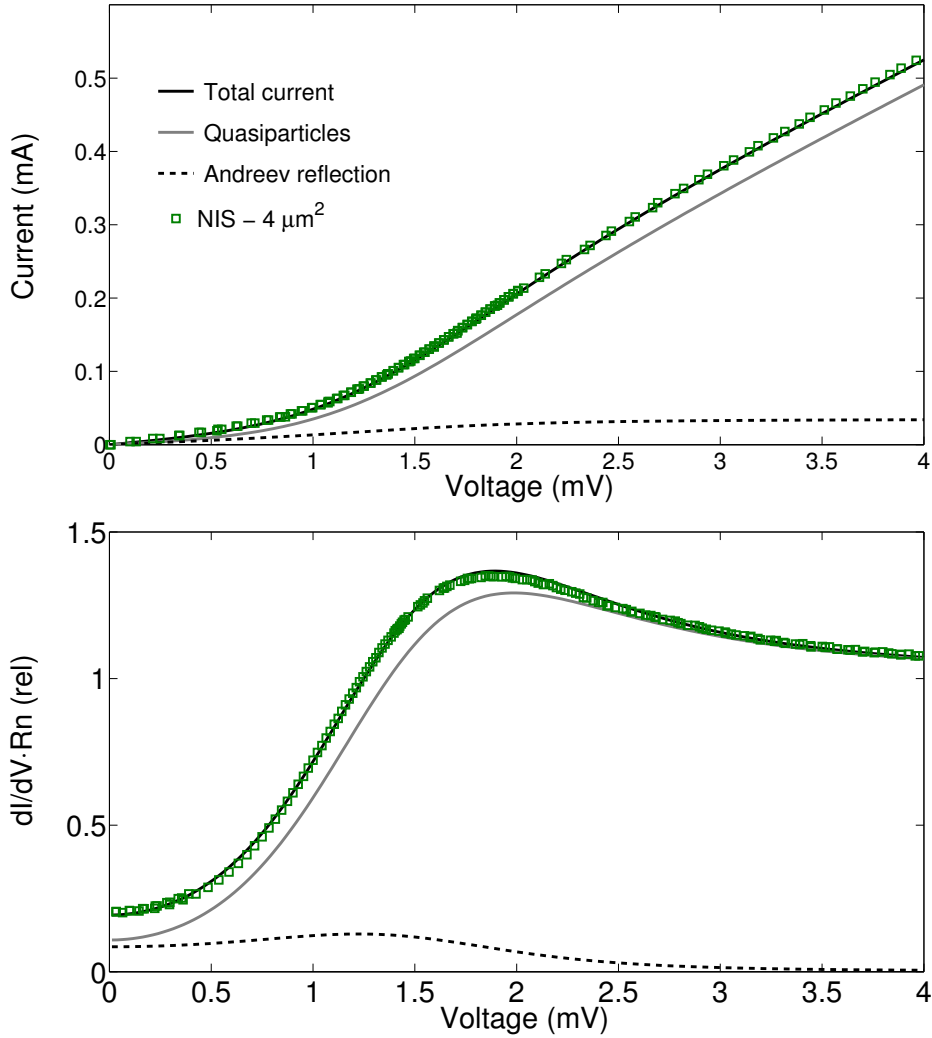


Figure 7.5: The current (a) and differential (b) resistance as a function of the voltage of a single planar NIS junction with a nominal area $A = 4\mu\text{m}^2$, and resistance of $R_n = 7.4\Omega$. The simulations is based on a non-uniform barrier with a relative variance of $\sigma/t = 0.23$.

sputter deposited through a PMMA lift-off mask, after which it is exposed for 24 min. to the afterglow regime of a N-plasma for nitridation [12]. A 100 nm thick Nb layer finishes the trilayer. After lift-off the junctions are patterned by EBL of a SAL resist mask, and a SF_6/O_2 reactive ion etch (RIE). Subsequently a 250 nm thick SiO_2 self-aligned layer is sputtered prior to the deposition of the 400 nm thick Nb topwire. The definition of the topwire is again done using EBL and a SF_6/O_2 RIE.

We fabricated junctions with areas ranging from 1 to 25 μm^2 . The different junctions show a reproducible resistance area product of $R_n A \approx 12 \Omega\mu\text{m}^2$. We measure the current voltage characteristic of the junctions using a four probe configuration, while simultaneously measuring the differential resistance with a standard lockin technique. Fig. 7.4b shows the current voltage characteristics of six nominally identical junctions, proving the reproducibility of the fabrication.

A detailed look at the current and differential conductance of the junction shows a subgap current which is higher than expected (Fig. 7.5). The grey line represents a junction with only first order quasiparticle tunneling, and a thermal distribution at the bath temperature. This model clearly underestimates the zero bias conductance of the junction, while at higher biases there is a current deficit. This indicates that part of the current is carried by second order processes. The full black line shows a simulation with a variable thickness according to Eq. (7.7) with $\sigma/t_0 = 0.23$, and agrees reasonably well with the data. The dashed black line corresponds to the contribution of second order tunneling. Given a typical barrier thickness of 1.5 to 2 nm (inferred from high resolution transmission electron microscopy measurements *Chapter 3*), this corresponds to a variance of the thickness of one or two atomic layers. This supports a picture of a polycrystalline AlN barrier, consisting of different areas with slightly different thicknesses [12].

7.5 Stacked junctions

To fabricate stacked junctions we use a similar fabrication recipe as for the planar junctions. However we start with the deposition of stack consisting of Nb(100 nm)/Al(5 nm)/AlN/Al(20(nm))/AlN/Nb(200 nm). To define the junctions we tried two different recipes. In the first case we anodize the thin Al layer after etching the upper Nb layer (SNAP,[24, 25, 26]). In the second case we use Ar milling to etch through the Al/AlN/Al/AlN layers, followed by a short anodization step. We found the latter recipe gave more consistent results, though both recipes did not give the same reproducibility obtained for the planar junctions. The $R_n A$ values for these junctions show big variations, in addition the IVs are very different for different area junctions. The subgap current scales with the square root of the junction size, we therefore suspect that the edges of the junctions are poorly defined.

Fig. 7.6 shows the current and differential resistance of a well-behaving double barrier junction. At double the gap voltage, a kink in the current is observed, and a corresponding peak in the differential conductance. These were absent for the planar junctions, and we attribute them to a non-equilibrium electron

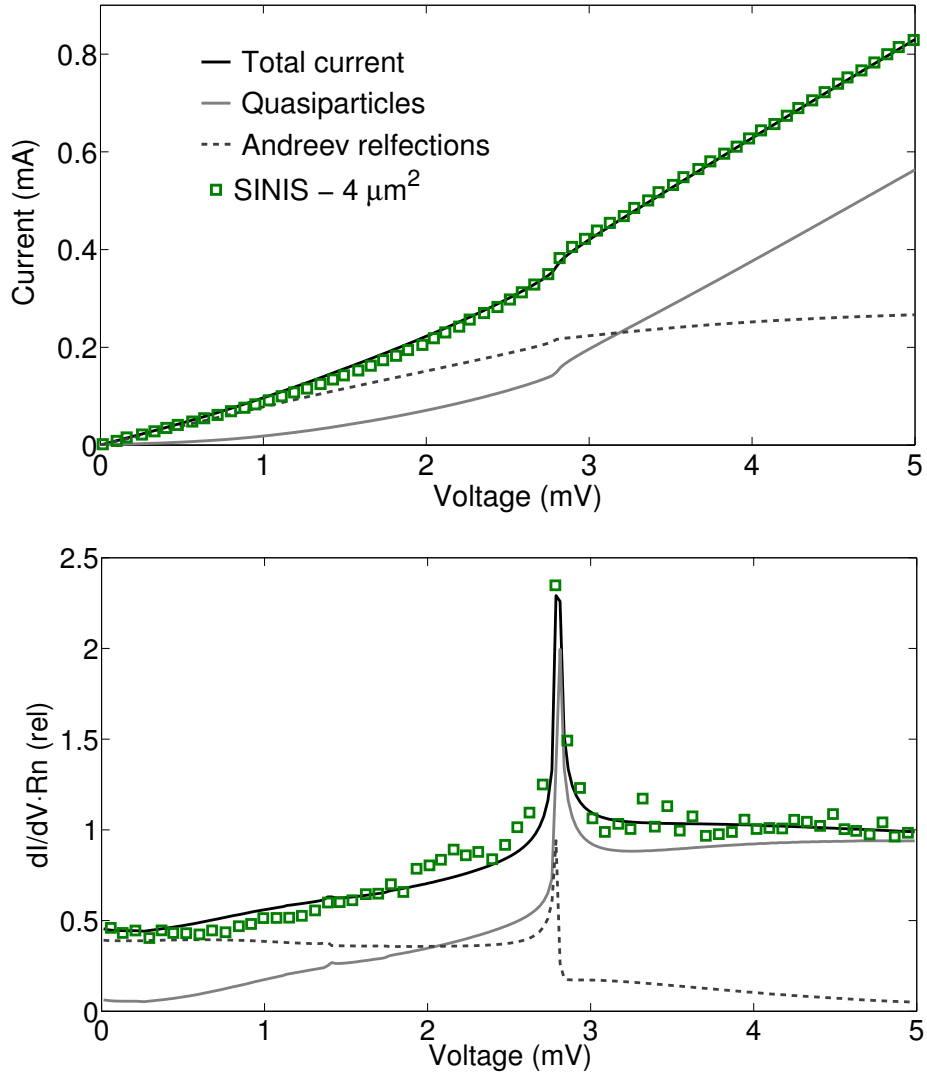


Figure 7.6: Current (a) and differential resistance (b) of a stacked double barrier junction. The high subgap conductance is due to higher order processes (grey dotted line), while the sharp peak at the gap voltage is due to a strong non equilibrium of the normal island.

distribution. This is due to the volume of the normal island, which is severely reduced with respect to the planar junction geometry. We take this into account using Eq. (7.10), where we use only electron phonon interaction with a relaxation time of $\tau = 3$ ns. The result is shown by the full black lines, while the dashed, black and the full, grey line show the respective contributions from first and second order tunneling.

7.6 Conclusions

In conclusion, we addressed both experimentally and theoretically the influence of non-uniform barriers on the thermal and charge transport of NIS microrefrigerators. We demonstrate that even for highly resistive tunnel barriers, small variations in the barrier thickness can have a decisive influence on the cooling performance. We fabricated highly transparent AlN barriers reproducibly in planar geometries. The high current densities involved necessitate an analysis in terms of a non thermal electron distribution functions. Based on the experimental results we show that the thickness variations of the AlN barriers are of the order of one atomic layer.

References

- [1] M. Nahum, T. Eiles, and J. Martinis, *APL* **65**, 3123 (1994).
- [2] F. Giazotto, T. T. Heikkilä, A. Luukanen, A. M. Savin, and J. P. Pekola, *Opportunities for mesoscopies in thermometry and refrigeration: Physics and applications*, *Rev. Mod. Phys.* **78**, 217 (2006).
- [3] P. J. Lowell, G. C. O’Neil, J. M. Underwood, and J. N. Ullom, *Macroscopic refrigeration by nanoscale electron transport*, *Appl. Phys. Lett.* **102**, 082601 (2013).
- [4] J. P. Pekola, T. T. Heikkilä, A. M. Savin, J. T. Flyktman, F. Giazotto, and F. W. J. Hekking, *Limitations in Cooling Electrons using Normal-Metal-Superconductor Tunnel Junctions*, *Phys. Rev. Lett.* **92**, 056804 (2004).
- [5] J. P. Pekola, V. F. Maisi, S. Kafanov, N. Chekurov, A. Kemppinen, Y. A. Pashkin, O.-P. Saira, M. Möttönen, and J. S. Tsai, *Environment-Assisted Tunneling as an Origin of the Dynes Density of States*, *Phys. Rev. Lett.* **105**, 026803 (2010).
- [6] P. J. Lowell, G. C. O’Neil, J. M. Underwood, and J. N. Ullom, *Andreev Reflections in Micrometer-Scale Normal Metal-Insulator-Superconductor Tunnel Junctions*, *J. of Low Temp. Phys.* **167**, 392 (2012).
- [7] A. Bardas and D. Averin, *Peltier effect in normal-metal \sim superconductor microcontacts*, *Phys. Rev. B* **52**, 12873 (1995).
- [8] K. Gloos, P. Koppinen, and J. Pekola, *Properties of native ultrathin aluminium oxide tunnel barriers*.
- [9] W. H. Rippard, A. C. Perrella, F. J. Albert, and R. A. Buhrman, *Ultrathin Aluminum Oxide Tunnel Barriers*, *Phys. Rev. Lett.* **88**, 046805 (2002).

- [10] W. H. Rippard, A. C. Perrella, F. J. Albert, and R. A. Buhrman, *Ultrathin Aluminum Oxide Tunnel Barriers*, Phys. Rev. Lett. **88**, 046805 (2002).
- [11] W. Miller, R.E. and Mallison, A. Kleinsasser, K. Delin, and E. Macedo, *Niobium trilayer Josephson tunnel-junctions with ultrahigh critical-current densities*, Appl. Phys. Lett. **63**, 1423 (1993).
- [12] T. T. Zijlstra, C. F. J. Lodewijk, N. Vercruyssen, F. D. Tichelaar, D. N. Loudkov, and T. M. Klapwijk, *Epitaxial aluminum nitride tunnel barriers grown by nitridation with a plasma source*, Appl. Phys. Lett. **91**, 233102 (2007).
- [13] G. E. Blonder, M. Tinkham, and T. M. Klapwijk, *Transition from metallic to tunneling regimes in superconducting microconstrictions: Excess current, charge imbalance, and supercurrent conversion*, Phys. Rev. B **25**, 4515 (1982).
- [14] K. M. Schep and G. E. W. Bauer, *Universality of Transport through Dirty Interfaces*, Phys. Rev. Lett. **78**, 3015 (1997).
- [15] Y. Naveh, V. Patel, D. V. Averin, K. K. Likharev, and J. E. Lukens, *Universal Distribution of Transparencies in Highly Conductive Nb/AlO_x/Nb Junctions*, Phys. Rev. Lett. **85**, 5404 (2000).
- [16] B. J. van Wees, P. de Vries, P. Magnée, and T. M. Klapwijk, *Excess conductance of superconductor-semiconductor interfaces due to phase conjugation between electrons and holes*, Phys. Rev. Lett. **69**, 510 (1992).
- [17] F. W. J. Hekking and Y. V. Nazarov, *Subgap conductivity of a superconductor / normal-metal tunnel interface*, Phys. Rev. B **49**, 6847 (1994).
- [18] M. G. Blamire, E. C. G. Kirk, J. E. Evetts, and T. M. Klapwijk, *Extreme critical-temperature enhancement of Al by tunneling in Nb/AlO_x/Al/AlO_x/Nb tunnel junctions*, Phys. Rev. Lett. **66**, 220 (1991).
- [19] T. M. Klapwijk, D. R. Heslinga, and M. G. Blamire, *Current-voltage characteristics of nonequilibrium double-barrier superconducting tunnel-junctions*, Physica B **165**, 1579 (1990).
- [20] A. Brinkman, A. A. Golubov, H. Rogalla, F. K. Wilhelm, and M. Y. Kupriyanov, *Microscopic nonequilibrium theory of double-barrier Josephson junctions*, Phys. Rev. B **68**, 224513 (2003).
- [21] J. Jochum, Mears, C. Golwala, B. S. Sadoulet, J. P. Castle, M. F. Cunningham, O. Drury, M. Frank, S. E. Labov, F. P. Lipschultz, H. Netel, and B. Neuhauser, *Modeling the power flow in normal conductor-insulator-superconductor junctions*, J. Appl. Phys. **83**, 3217 (1998).

-
- [22] S. Rajauria, H. Courtois, and B. Pannetier, *Quasiparticle-diffusion-based heating in superconductor tunneling microcoolers*, Phys. Rev. B **80**, 214521 (2009).
- [23] J. J. P. Pekola, D. V. Anghel, T. I. Suppala, J. K. Suoknuuti, A. J. Manninen, and M. Manninen, *Trapping of quasiparticles of a nonequilibrium superconductor*, Appl. Phys. Lett. **76**, 2782 (2000).
- [24] H. Kroger, L. N. Smith, and D. W. Jillie, *Selective niobium anodization process for fabricating Josephson tunnel junctions*, Appl. Phys. Lett. **39**, 280 (1981).
- [25] S. Imamura, T. and Hasuo, *Characterization of Nb/AlO_xAl/Nb Josephson junctions by anodization profiles*, J. Appl. Phys. **66**, 2173 (1989).
- [26] I. P. Nevirkovets, *Fabrication and DC characteristics of vertically stacked SIS-type structures for use as low-temperature detectors*, Superconductor Science and Technology **8**, 575 (1995).

Chapter 8

Evanescent states and non-equilibrium in driven superconducting nanowires

We study the non linear response of current-transport in a superconducting diffusive nanowire between normal reservoirs. We demonstrate theoretically and experimentally the existence of two different superconducting states appearing when the wire is driven out of equilibrium by an applied bias, called global and bimodal superconducting state. The different states are identified by using two probe measurements of the wire, and measurements of the local density of states with tunneling probes. The analysis is performed within the framework of the quasiclassical kinetic equations for diffusive superconductors.

This chapter was published as N. Vercruyssen, T. G. H. Verhagen, M. G. Flokstra, J. P. Pekola, and T. M. Klapwijk, *Physical Review B* 85, 224503 (2012).

8.1 Introduction

Superconducting nanowires are often part of objects to study the Josephson-effects in graphene, carbon nanotubes or semiconducting nanowires. In addition in many cases superconducting nanowires themselves are used to study their response to radiation. In most cases the electron back-scattering resistance is assumed to be located at the interfaces and in the normal metal part. An interesting question is to what extent the superconducting mesoscopic or (nano)wires themselves contribute to the resistance of a device due to the conversion from normal current to supercurrent and *vice versa*. For superconducting nanowires between superconducting contacts a common assumption is that the applied power leads to dissipation and to an increased temperature varying over the wire length [1]. In quite a few experiments with a nanowire between normal or superconducting pads, a parabolic temperature profile $T(x)$ is assumed to control the local superconducting properties [2, 3, 4]. The definition of a temperature however requires that the electrons are in local equilibrium, a condition not easily met for wires of mesoscopic length scales. In the case of a biased normal wire [5] the diffusion time, $\tau_D = L^2/D$, with L the wire length and D the diffusion constant, can be much shorter than the inelastic relaxation time τ_{in} . In this case the electron distribution is highly non-thermal and given by a two step function $f(E, x) = (1-x)f_0(E-eV/2)+xf_0(E+eV/2)$, with $f_0(E, T) = 1/(\exp(E/kT)+1)$ a Fermi-Dirac distribution, V the applied bias, k Boltzmann's constant, E the energy of the electrons measured from the Fermi energy, T the bath temperature and x the coordinate along the wire. A general, non-thermal (or non-equilibrium) electron distribution in a superconductor influences almost all aspects of that superconductor. It affects the local Cooper pair density and the current-carrying capacity, but it can also produce a voltage-drop in the superconductor, i.e. a DC resistance of the superconductor. To discuss the various contributions it is advantageous to separate the non-equilibrium distribution function, $f(E)$, into an energy (or longitudinal) mode, f_L , acting primarily on the amplitude of the superconducting gap, and a charge (or transverse) mode, f_T , which lead to a shift in the pair chemical potential μ_{cp} [6]. The latter mode f_T describes an imbalance between electron and holes in the excitation-spectrum, leading to a net charge Q^* in the (decaying) excitations. This contribution can be dominant in experiments probing electrical transport in superconducting heterostructures at subgap energies.

In this paper we report on an experimental and theoretical study of nonlinear electrical transport in a well-defined model system [7, 8], in which a superconducting wire is connected to two large normal contact pads (Fig. 8.1). The normal

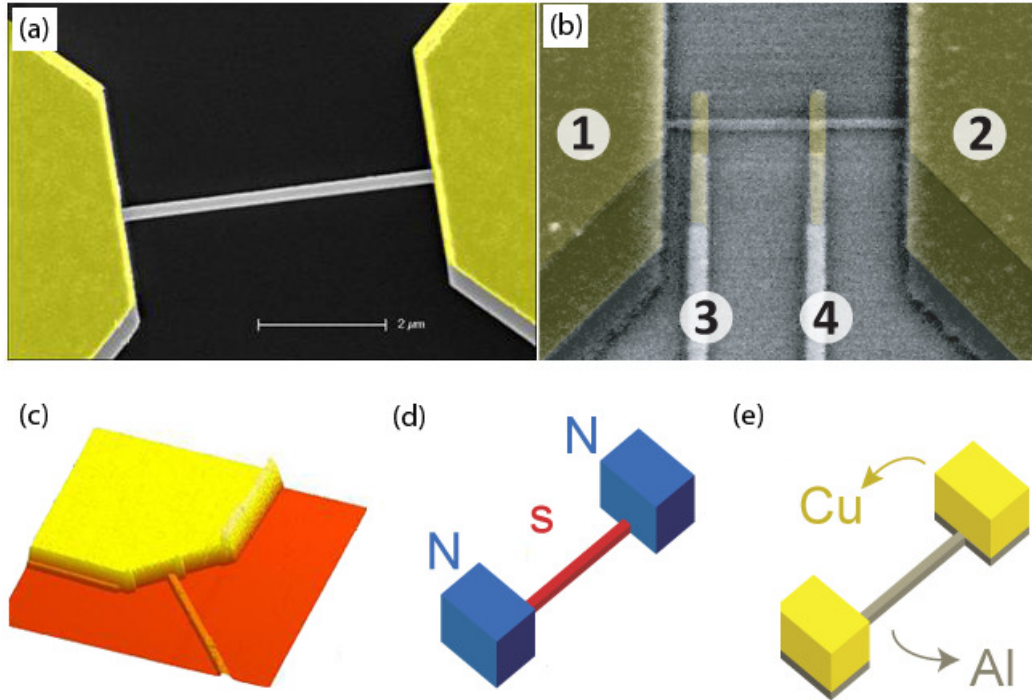


Figure 8.1: A superconducting Al nanowire connected to two massive normal reservoirs, consisting of the same Al, covered by a normal metal Cu layer: (a) SEM-picture, (c) AFM-picture, (d, e) schematic representation. The thin Al of the pads is driven normal by the inverse proximity effect of the thick normal Cu. Normal tunneling probes are attached for local measurements (b).

electrodes induce evanescent subgap states in the superconducting wire. In addition they act as equilibrium electron reservoirs to fill and empty the states in the superconducting wire. When a bias eV is applied, evanescent electrons and holes are injected from the reservoirs into the superconducting wire, and the resulting non-equilibrium distribution function consists of both an energy mode f_L and a charge mode f_T . The well defined boundary conditions and simplicity of this system make it a natural choice to study the superconducting state in the presence of a general non-equilibrium.

We address these microscopic properties of the wire experimentally using two point measurements of the nanowire, which are a sensitive probe for the resistive properties originating in f_T . Measurements with tunneling probes allow to measure the local density of states and the different chemical potentials involved. We demonstrate that two distinct metastable superconducting states exist when the wire is driven (Fig. 8.2). The first superconducting state extends

over the complete length of the wire, and has been reported in the linear regime by Boogaard et al [9]. The second state exists only under driving, and consists of two, geometrically separated superconducting domains, both at the ends of the wire. We show that the superconductivity nucleates in the vicinity of the normal reservoirs, because the local electron distribution is closer to the equilibrium state. The existence of metastable states has been identified in previous work using phenomenological models [10, 11], based on a normal resistive domain. We analyze these states using the quasiclassical Green's functions, and show how the energy mode controls the existence of these states, whereas the charge mode controls the resistance. Hence, the full non-linear response is found to be the result of a complex interplay between both the charge and the energy mode non-equilibrium.

8.2 Theoretical framework

We consider a model system consisting of a superconducting one dimensional diffusive wire connected to two normal, equilibrium reservoirs (Fig. 8.1d). Electrons are injected into and extracted from the superconducting wire by the reservoirs with equilibrium Fermi distributions $f_0(E \pm eV, T)$, with relative Fermi-levels determined by the applied voltage V . Within the wire the electrons are distributed over the energies with a position and energy dependent non-equilibrium distribution function $f(E, x)$ determined by a diffusion equation. In addition the electronic states concerned are decaying states, evanescent modes, as their energy is smaller than the energy gap ($eV \leq 2\Delta$). Therefore it is necessary to include the interplay between these short-lived states and the superconducting condensate, which goes beyond a two-fluid description, in which a sharp distinction between long-living quasiparticle states and the condensate is assumed. Such an analysis is performed using the quasiclassical Green's functions theory for superconductivity, which treats the electronic properties of the excitations and the condensate on the same footing [12]:

$$\check{G} = \begin{pmatrix} \hat{G}^R & \hat{G}^K \\ 0 & \hat{G}^A \end{pmatrix}, \hat{G}^R = \begin{pmatrix} G & F_1 \\ F_2 & G^\dagger \end{pmatrix}. \quad (8.1)$$

The retarded (advanced) functions $\hat{G}^{R(A)}$ consist of normal and anomalous propagators G and F , which describe the single electron spectrum and the coherence between electrons respectively. The occupation numbers of the electronic excitations are contained in the Keldysh component \hat{G}^K .

In general these Green's functions are dependent on the time, energy, position and momentum of the particle: $G = G(E, t, r, p)$. However typical variations occur on a much slower length scale than the Fermi wavelength. The Green's functions are sharply peaked around the Fermi momentum $p = p_F$, and a considerable simplification can be obtained by integrating G over all momenta. A second simplification arises from the short mean free path in dirty superconducting films, which averages out any dependence on the momentum direction. The resulting equations were obtained by Usadel [13] and they only contain what is called the quasiclassical Green's functions, $g(E, x, t)$ and $f(E, x, t)$. Our experimental observations indicate that relevant solutions are stationary, so in addition we neglect all time dependences in the equations. This choice is partially supported by theoretical work of Snyman et al [14] who demonstrate for a simplified system that the solutions for a DC bias are always stationary. To parametrize $g(E, x)$ and $f(E, x)$ we use a complex pairing angle $\theta(E, x)$ describing correlation between electrons and holes, and a complex phase χ : $g = \cos(\theta)$, $f_{1,2} = \sin(\theta)e^{\pm i\chi}$ [15]. The normalization condition $g^2 + f_1^\dagger f_2 = 1$ is automatically fulfilled, while the variations of $\theta(E, x)$ and $\chi(E, x)$ are determined by the following diffusion equations:

$$\begin{aligned}
& \hbar D \{ \nabla^2 \theta - \sin \theta \cos \theta (\nabla \chi)^2 \} \\
& = -i2E \sin \theta - \cos \theta (\Delta e^{-i\chi} + \Delta^* e^{i\chi}), \\
& \quad \hbar D \nabla \{ \sin^2 \theta (\nabla \chi) \} \\
& = i \sin \theta (\Delta e^{-i\chi} - \Delta^* e^{i\chi}), \tag{8.2}
\end{aligned}$$

with D the normal state diffusion constant. The first equation describes how the presence of a local superconducting order parameter $\Delta(x)$ generates pair correlations $\theta(E, x)$, which allows to calculate the local density of states (dos) $N(E, x) = \text{Re} \cos(\theta)$. The second equation relates the phase gradient of the gap to the presence of supercurrents.

A convenient description of a non-equilibrium superconductor is obtained by introducing a generalized distribution function $h(E)$, defined as $G^K = G^R h(E) - h(E) G^A$. To disentangle the influence of the distribution function on the amplitude and the phase of the order parameter, $h(E)$ is split in the even part (energy mode) in particle-hole space $f_L(E, x)$, and the odd part (charge mode) $f_T(E, x)$. The total electron distribution functions $f(E, x)$ is then obtained from $2f(E, x) = 1 - f_L(E, x) - f_T(E, x)$. The presence of a charge mode is related to the presence of a charge Q^* integrated over all excitations, and the consequence of inhomogeneity in the superconducting system, leading to conversion of quasi-particle current to supercurrent. Charge imbalance has been studied thoroughly

at temperatures close to T_c , *i.e.* for long lived quasiparticle excitations [16, 17]. However, the concept of charge imbalance also applies to short-lived evanescent states [18], for small injection voltages and at low temperatures [19, 20].

Conservation of energy E and charge Q result in two coupled diffusion equations for f_L and f_T :

$$\hbar D \nabla J_E = 0, \hbar D \nabla J_Q = 2R_L f_L + 2R_T f_T, \quad (8.3)$$

with

$$\begin{aligned} J_E &= \Pi_L \nabla f_L + \Pi_X \nabla f_T + j_\epsilon f_T, \\ J_Q &= \Pi_T \nabla f_T - \Pi_X \nabla f_L + j_\epsilon f_L \\ \Pi_{L,T} &= 1 + |\cos \theta|^2 \mp |\sin \theta|^2 \cosh(2\chi_2), \\ \Pi_X &= -|\sin \theta|^2 \sinh(2\chi_2), \\ j_\epsilon &= 2\text{Im}(\sin^2 \theta \nabla \chi), \\ R_{L,T} &= \text{Re}(\sin \theta (\Delta e^{-i\chi} \mp \Delta^* e^{i\chi})), \end{aligned} \quad (8.4)$$

where $\Pi_{L,T,X}$ are generalized diffusion constants, j_ϵ is the spectral supercurrent and $R_{L,T}$ determine the magnitude of the source term on the right hand side of Eq. (8.3). The energy current is dominated by the diffusion of the energy mode f_L . Our Al wires are relatively short which means we can neglect inelastic processes, as the inelastic electron-electron and electron-phonon interaction lengths are of the order of $10 \mu\text{m}$ at a temperature of 1 K [21]. For long wires or materials with a strong electron-phonon interaction this is not necessarily true. However, this case has been recently assessed by Serbyn and Skvortsov [22], using the time-dependent Ginzburg-Landau equations. The stronger electron-phonon coupling of Nb results in a inelastic mean free path of roughly $0.1 \mu\text{m}$ [23]. The charge current consists partly of a normal current driven by a gradient of the charge mode, $I_n = \Pi_T \nabla f_T$, and partly of a supercurrent related to a gradient of the phase $I_s = f_L j_\epsilon$. Conversion of a normal current into a supercurrent implies a change of ∇f_T , and is proportional to $R_T \approx \Delta$ in Eq. (8.3).

The position dependent potential in the superconductor $e\phi(x)$ is obtained by integrating the charge of the quasiparticle excitations over all energies:

$$e\phi(x) = \int_{-\infty}^{\infty} N(E) f_T^S(E, x) dE \quad (8.5)$$

In order to conserve charge neutrality, the presence of the net charge in the excitations is compensated by a shift in the pair chemical potential $\delta\mu_{cp}(x)$. This means that the static electric field $E = \nabla\phi$ which drives the normal current

I_n , does not influence the condensate, since it is exactly balanced by $\delta\mu_{cp}(x) = -e\phi(x)$. If this were not the case, the Cooper pairs would accelerate.

The retarded and kinetic equations (8.2, 8.3) are completed with the self consistency relation for $\Delta(x)$:

$$\Delta(x) = \frac{N_0 V_{eff}}{4i} \int_{-\hbar\omega_D}^{\hbar\omega_D} dE$$

$$(\sin\theta e^{i\chi} - \sin\theta^* e^{i\chi^*}) f_L - (\sin\theta e^{i\chi} - \sin\theta^* e^{i\chi^*}) f_T. \quad (8.6)$$

The charge mode is directly related to the observed potential drop over the superconductor through Eq. (8.5), the energy mode f_L only appears implicitly in the gap Eq. (8.6).

8.3 Possible solutions

In this section we present the numerical solutions of Eqs. (8.2 - 8.6) for the model system shown in Fig. 8.1. The wire can be considered to be one dimensional, as the width and thickness are smaller than the dirty superconducting coherence length $w, t \leq \xi = \sqrt{\frac{\hbar D}{2\Delta_0}}$. The normal equilibrium reservoirs act as boundary conditions, both for the superconducting pairing-angles $\theta = \nabla\chi = 0$ and the distribution functions $f_{L,T}$. Temperature enters the problem only through the boundary conditions for f_L and f_T , while all non-equilibrium processes in the wire itself are contained in the distribution functions. After an initial guess for $\Delta(x)$, the superconducting angles θ and χ are calculated from the retarded equations (8.2). Subsequently the kinetic equations (8.3) can be solved to obtain f_L and f_T . Finally the value of $\Delta(x)$ is updated using Eq. (8.6), and this process is repeated until all values converge. We find two distinct superconducting solutions for the problem: (a) one global superconducting state (Fig. 8.2a) and (b) a bimodal superconducting state separated by a normal valley (Fig. 8.2b).

8.3.1 One global superconducting state

The first solution is characterized by one coherent superconducting state which extends over the full length of the wire, though the strength of the superconducting gap, Δ , is suppressed at the edge of the wire by the presence of the normal reservoirs (Fig. 8.2a). Though fully superconducting, the wire has a finite resistance due to the conversion of a normal current into a supercurrent, as shown by the position-dependent voltage V . Normal electrons which are injected from the metallic reservoirs, decay into Cooper pairs over roughly one coherence length ξ .

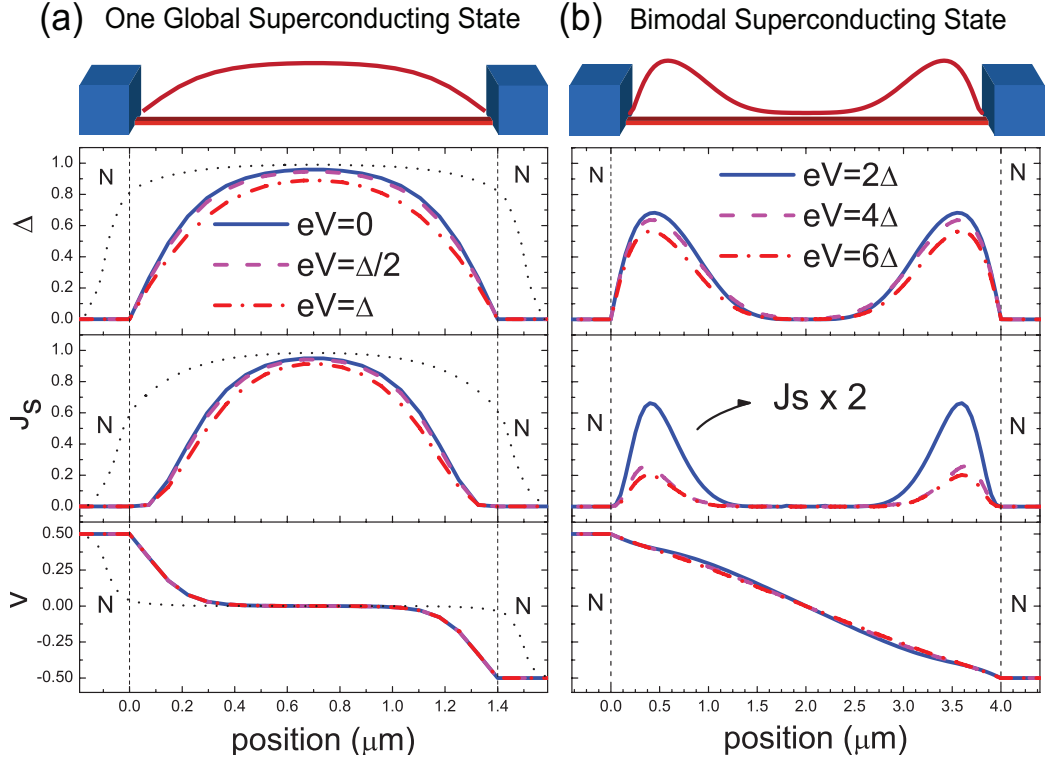


Figure 8.2: (a) The complete wire is in a single superconducting state with order parameter $\Delta(x)$. However near the normal reservoirs the condensate carries only a small fraction J_s of the current as a supercurrent, which results in a resistance and a voltage drop at the ends of the wire, over roughly a coherence length. At the lowest temperatures a small proximity effect can occur at the connection of the bilayer reservoirs to the wire (schematically illustrated by dotted black lines). (b) Two distinct superconducting domains at the ends of the wire are separated by a normal region in the centre of the wire. Due to the small supercurrent, the voltage profile is almost equal to the normal state.

The excess charge Q^* associated with the charge mode f_T of these evanescent quasiparticle states results in the presence of an electric field in the superconductor, and hence a potential drop over the same length the supercurrent increases. These processes correlate with the picture of electrons being injected at energies $E \approx eV$, leading to a two-step distribution f_L , as shown previously by Keizer et al [7]. While the charge mode non-equilibrium f_T relaxes over a length scale of ξ , because of interaction with the condensate, the energy mode f_L remains constant over the length of the wire due to the absence of inelastic interactions (Fig. 8.3a).

For increasing voltages there is hardly any change in the profiles of Δ , ϕ , $J_{s,n}$, $f_{L,T}$, until the wire switches to the normal state. For example there is no gradual ex-

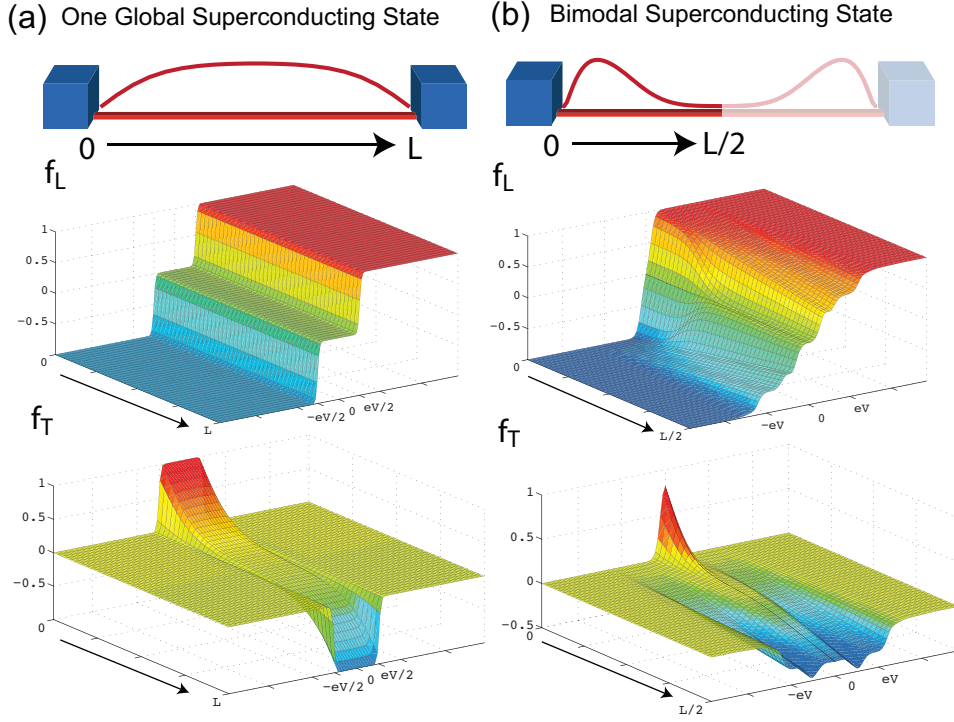


Figure 8.3: The even mode f_L and odd mode f_T of the non-equilibrium distribution function $f(E, x)$. (a) For the global superconducting state, a two step distribution is present through the full wire, while the charge mode is only present at the edges. (b) A strong, non-thermal energy mode non-equilibrium f_L suppresses superconductivity at the centre of the wire.

pansion of the voltage-carrying parts at the end of the wires, as one would guess qualitatively. A careful analysis [7] indicates that the energy mode f_L triggers this transition, while the current is still far below the critical pair breaking current I_{c0} .

In performing these numerical calculations we assumed that the reservoirs are fully normal down to the lowest temperatures. The dashed lines in Fig. 8.2a however show a schematic picture of a situation where the reservoirs are proximitized by the wire, which in fact is a situation we encounter in the experiments. The conversion and voltage drop occurs primarily in the contact pads, and the measured resistance is largely a spreading resistance of the contact pad. We will show experimentally that the latter contribution can be quenched by the bias and by a magnetic field.

8.3.2 Bimodal superconducting state

A second solution was inspired by our experimental results. It consists of two separate superconducting domains located at each end of the wire (Fig. 8.2b). A strong energy mode f_L suppresses superconductivity in the middle of the wire, while the presence of the cold reservoirs near the ends of the wire favors locally the emergence of a gap.

Modeling this state is complicated, as the presence of two superconducting regions gives potentially rise to time-dependent processes. We can however avoid this complication by assuming that the centre of the wire is fully normal. In that case it is possible to proceed numerically by splitting the wire in two half-wires and treat them independently, using $\theta = \nabla\chi = 0$ as boundary conditions. While the distributions at the end of the wire are again given by the equilibrium reservoirs, in the middle of the wire we match the distribution functions f_L and f_T and their derivatives. The occupation of electronic states with energies $E + eV, E - eV$ are coupled by the applied voltage, while previously they were independent. In addition the superconducting potential mixes particle and hole states, and one retrieves relatively complex solutions for $f_{L,T}(E, x)$ (Fig. 8.3b). At the centre of the wire the energy mode non-equilibrium is close to a thermal one, but at an elevated temperature similar to a parabolic temperature profile. The remaining structure is in essence due to energy-conserving Andreev reflection processes, similar to the electron distribution in a SNS structure [24].

The emerging superconducting blobs at the end of the wire are relatively small, both in magnitude $|\Delta| \approx |\Delta_0|/2$ and in size $L_S \approx 4\xi$. Due to their limited size only a tiny fraction of the total current is converted into a supercurrent, and the voltage profile is almost identical to the normal state. While the local microscopic properties at the end of the wire show a strong superconducting signature, the global properties of the wire are hardly influenced. This is true for the current (which is almost completely normal) and the voltage profile, but also for the density of states and the distribution functions. Apart from some small modifications, the distribution function in the wire is given by a two-step function. The non-equilibrium energy mode f_L is the strongest in the centre of the wire, and is the main reason why the superconducting state nucleates near the equilibrium reservoirs. The influence of f_T is limited as the condensate carries almost no (super)current.

8.4 Sample design, fabrication and characterization

Figure 8.1a shows a typical superconducting Al nanowire contacted by two massive normal reservoirs, consisting of the same thin Al layer covered by a thick Cu layer. For reasonably clean interfaces the inverse proximity effect of the thick Cu drives the Al normal down to the lowest temperatures. The massive volume of the contacts guarantees that they act as equilibrium reservoirs from which electrons are injected into the wire. When a bias is applied however, the temperature of the reservoirs electron distribution function $f_0(E, T)$ might for increasing voltage deviate from the bath temperature according to [25]:

$$T^2 = T_0^2 + b^2 V^2, \quad (8.7)$$

$$b^2 = \frac{1}{\pi L} \frac{R_{\square}}{R_{wire}} \ln \left(\frac{r_0}{r_1} \right), \quad (8.8)$$

where L is the Lorenz number, R_{\square} the sheet resistance of the contact, and r_0 and r_1 respectively the electron-electron and electron-phonon inelastic mean free path. The temperature increase can be considerable, and the most obvious way of decreasing it is to minimize the ratio R_{\square}/R_{wire} by using thick reservoirs, which we have implemented in our sample design.

The samples are realized by three angle shadow evaporation through a suspended resist mask (PMMA/LOR double layer), in a system with a base pressure of 0.5 - 1.5 x 10⁻⁷ mbar. The parameters of the different samples are summarized in Table 8.1. First 50 - 90 nm of 99.999% purity Al is deposited through a slit in the suspended mask to create the superconducting wire and the thin bottom layer of the pads. Evaporation of a thick (200 - 500 nm) copper layers under an angle, which avoids deposition through the slit, completes the normal bilayers forming the reservoirs. The time between the two steps is kept to a minimum (< 10 min) to ensure a clean and transparent interface. Subsequently the Al is oxidized during 5 minutes in a pure O₂ atmosphere with a pressure of 4.6 mbar to create an AlO_x tunnel barrier of $R_n A \approx 300 \Omega \mu\text{m}^2$. The Cu probes are deposited during the last evaporation step under a second angle. The size of the wires is measured using scanning electron microscopy. The thickness was obtained from a quartz crystal monitor used during the deposition of the Al film, and calibrated by atomic force microscopy.

#	L	w	t	R_n	ρ	D	T_c	ξ	R_s
#	(μm)	(nm)	(nm)	(Ω)	($\mu\Omega\text{cm}$)	(cm^2s^{-1})	(K)	(nm)	(Ω)
1a	1.4	100	90	2.8	1.8	98	1.23	131	1.0
1b	2.0	100	90	4.5	2.0	87	1.23	124	0.81
2	3.0	200	50	3.7	1.23	143	1.35*	152	0.7
3a	2.0	100	50	6.2	1.54	115	1.35	135	1.7
3b	4.0	100	50	13.3	1.66	106	1.35	131	1.7
4	1.5	100	50	5.1	1.70	104	1.35*	129	1.7
5	2.0	100	50	4.8	1.20	147	1.35*	154	1.5

Table 8.1: Overview of the properties of the different samples: L - length, w - width, t - thickness, R_n - normal state resistance, ρ - resistivity, D - diffusion constant, $\xi = \sqrt{\hbar D/2\Delta}$ - coherence length, T_c - critical temperature, R_s - low temperature resistance in the superconducting state. For samples indicated with an asterisk, there is no measurement available for T_c . We assumed the same value for T_c as for sample 3 which was fabricated under the same conditions.

8.4.1 Linear response of the nanowire

Figure 8.6a shows a typical current voltage curve (IV). The linear regime extends up to a critical current designated by I_{c1} . This initial slope has been measured as a function of temperature with an AC technique leading to the results shown in Fig. 8.4. We used a bias current I_{12} of 1 μA modulated at 342 Hz (terminals labels are shown in Fig. 8.1b). The two point resistance of this 1.4 μm long wire (sample 1a) as a function of temperature displays a well-defined pattern (open squares). The spreading resistance of the contact pads adds a small but finite contribution of approximately 20 m Ω to the measured two point resistance. Clearly, at high temperatures the wire is normal and has a resistance R_n . When the temperature is decreased below $T_c = 1.05$ K the resistance of the wire drops considerably as it becomes superconducting. This critical temperature is depressed compared to the intrinsic critical temperature of the aluminum due to the proximity-effect, as discussed by Boogaard et al [9]. For intermediate temperatures (500-800 mK) the resistance appears to saturate at a value $R_s \approx 1 \Omega$. As we will analyze further, this is the result of a normal current penetrating into the wire over roughly one coherence length ξ , yielding a $R_s \approx 2\rho\xi/A$, with A the crosssection.

Further lowering of the temperatures leads to a further drop in resistance to almost zero, suggesting that the bilayer contacts are becoming superconducting, due to a low transparency of the interface between the Al and Cu layers. To check this hypothesis we measured the resistance of identical Al/Cu bilayer strips down to the lowest temperatures, and find that they stay normal. Instead we attribute

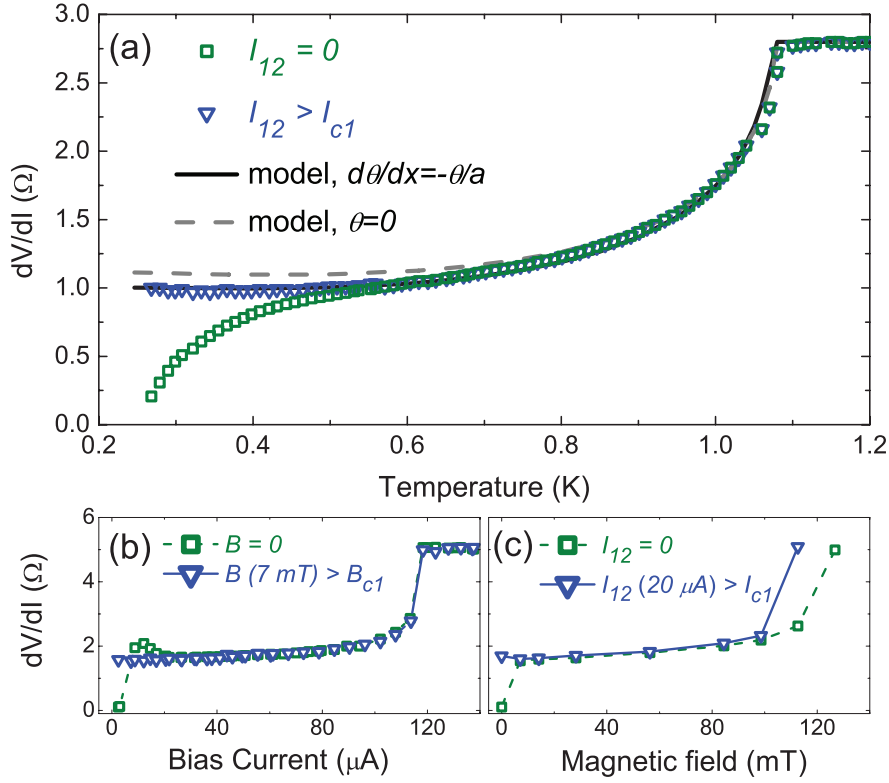


Figure 8.4: (a) The two probe resistance versus temperature of a $1.4 \mu\text{m}$ long wire (sample 1a). Due to the proximity effect of the wire on the normal reservoirs, the resistance becomes negligible at low temperatures. This weak proximity effect can be suppressed by applying a small bias current (b) or small magnetic field (c) (sample 4, 200 mK). This 'corrected' wire resistance is constant down to the lowest temperatures (green squares of panel a). A model (dashed line) with rigid normal boundary conditions for the pairing angle $\theta = 0$ slightly overestimates the observations. A weaker boundary condition (full line), in which θ decays gradually to zero over a characteristic length a shows excellent agreement with the experiment.

the vanishing resistance due to the proximity effect by the nanowire on the contact point between the normal reservoir and the superconducting wire itself. The superconductivity gradually spreads out into the bilayer, leading to a normal-superconducting boundary which moves from the nanowire into the contact pads (Fig. 8.2a). Consequently, the current conversion resistance in the wire itself becomes gradually less relevant. As the cross-section for the conversion moves into the contacts it becomes larger, reducing its resistive contribution. Hence, only a part of the spreading resistance ($\approx 20 \text{ m}\Omega$) is measured.

This observed pattern changes if we measure the resistance for a small DC bias current, larger than I_{c1} . Then superconductivity in the weakly proximitized

region in the pads is suppressed, and the differential resistance stays constant down to the lowest temperatures (blue triangles Fig. 8.4a). To further test this hypothesis we measured the IV of the wire while we apply a small magnetic field of 7 mT, parallel to the pads but perpendicular to the wire (Fig. 8.4b). The vanishing resistance at zero bias is no longer observed, while the differential resistance at higher biases is identical to the one without magnetic field. This indicates that such a small field does not influence the properties of the wire, and only quenches the weakly proximitized region in the pads. Only at a much higher field $B \approx 100$ mT we observe a change in the differential resistance of the wire (Fig. 8.4c).

The dashed gray line in Fig. 8.4 shows the calculated two point resistance. The bulk critical temperature $T_{c0} = 1.23$ K was the only free parameter in the fit, while the diffusion constant $D = 98$ cm²/s was obtained through the relation $D = \rho/N_0e^2$. The resistivity ρ is deduced from the normal state resistance R_n , using $N_0 = 2.2 \cdot 10^{47}$ J⁻¹m⁻³ for the density of states at the Fermi level [26]. The superconducting coherence length is obtained from $\xi = \sqrt{\frac{\hbar D}{2\Delta}}$. Although the numerical calculation agrees quite well with the data (for $I > I_{c1}$), the model overestimates the residual resistance at low temperatures. This indicates that the assumption of completely normal contact pads is too rigid, as also observed by Boogaard et al [9]. To include the geometric out-diffusion of coherent electrons into the normal pads, we adjust the boundary conditions at the ends of the wire to: $\nabla\theta = -\theta/a$, which indicates the dilution of superconductivity into the normal pads over a characteristic length scale a . With $a \approx 18$ nm (full line in Fig. 8.4) we find excellent agreement with the observations. The key parameters are listed in Table 8.1 for the different samples. It demonstrates that the linear response of the wires is well understood, but that the boundary conditions are a sensitive part of the problem even for the thick and wide contact pads used. However for bias currents $I \geq I_{c1}$ the system is in a well defined state, which can be connected to the theoretical predictions.

8.4.2 Characterization of the tunnel probe

To measure locally the density of states, the electrostatic potential $e\phi(x)$ and the chemical potential of the condensate μ_{cp} we use a normal tunneling probe. The current flowing from a normal tunnel probe contacted to a non-equilibrium superconductor at a position x is given by:

$$I_T(V, x) = \frac{1}{eR_n} \int_{-\infty}^{\infty} \text{Re}\{\cos(\theta(E, x))\} \{f_T^S(E, x) - f_T^N(E + eV)\} dE, \quad (8.9)$$

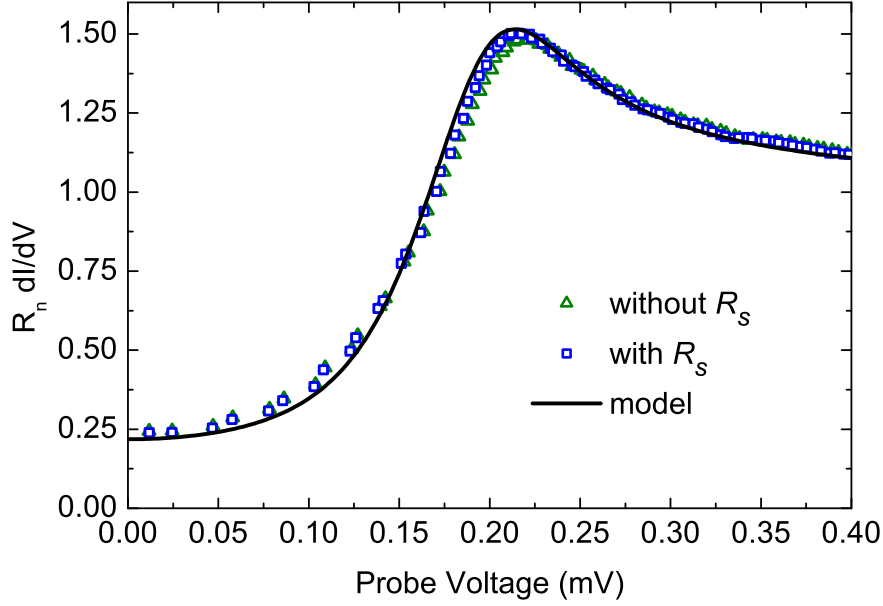


Figure 8.5: The differential conductance of the local tunnel probe as a function of applied voltage (magenta triangles). Good agreement between experiment and theory (full line) is obtained when the series resistance of the set-up is included (blue squares).

with $\theta(E, x)$ the pairing angle, $f_T^S(E, x)$ the charge mode non-equilibrium distribution in the superconductor, and $f_T^N = 1 - f_0(E + eV) - f_0(-E + eV)$ the distribution function in the normal probe. Using Eq. (8.5) we can rewrite this to:

$$I_T(x) = \frac{1}{eR_n} \left\{ e\phi(x) + \int_{-\infty}^{\infty} N(E, x) f_T^N dE \right\}. \quad (8.10)$$

The tunnel current consists of two contributions, the first one does not depend on the applied voltage, but is completely determined by the charge imbalance in the superconductor, leading to the local electrostatic potential $\phi(x)$. The second contribution is given by the convolution of the local dos $N(E, x)$ of the superconductor and the distribution function $f_T^N(E + eV)$ in the normal metal. At low temperatures the differential conductance of the tunnel contact is a direct measure for the density of states in the superconductor. The condensate chemical potential of the superconductor can be obtained from $N(E, x)$, which is symmetric around $E = \mu_{cp}$.

Figure 8.5 shows a typical measurement of the differential resistance for a tunnel probe located at a distance of $320 \text{ nm} = 2.4\xi$ from the normal reservoir of a $4 \mu\text{m}$ long wire. The nanowire is biased just above I_{c1} , to ensure it is in a well defined state. The bias current needed to drive the probe is typically four

orders of magnitude smaller than the bias current of the nanowire, due to the high normal resistance of the tunnel junction ($R_T = 43 \text{ k}\Omega$). Hence it is safe to assume that the properties of the nanowire are not influenced by the measurement of the probe. One recognizes the coherence peaks at the gap voltage, however the subgap dos is increased in comparison to the BCS values due to the presence of the normal banks, and the driving of the nanowire. The simulated local dos, for the set of parameters, is in good agreement with the data, but near the gap voltage a small discrepancy exists. We attribute this to a series resistance in the wiring of the tunnel probe and can correct our data for this contribution. We obtain a good agreement between the data and the theory using a series resistance of $R_S = 1.2 \text{ k}\Omega$, which is the estimated wiring resistance of the experimental set-up.

8.5 Two-state analysis and discussion

We have realized and studied a total of 7 samples with parameters shown in Table 8.1. All displayed similar behavior. The non linear current voltage characteristic of a typical sample is shown in Fig. 8.6a, with two clearly distinguished branches. Before discussing the details we first indicate the various signatures for processes, which dominate the various regimes. Increasing the current from zero bias we pass I_{c1} the current at which the proximitization in the banks is quenched as discussed in Section IV.A. Beyond I_{c1} until I_{c2} , we claim that the wire remains in the global superconducting state, characterized by a low and almost constant differential resistance R_s (Fig. 8.6b). This resistance reflects the conversion of a normal current into a supercurrent and is located at the edges of the wire. At the current $I = I_{c2}$ the wire switches into the normal state, leading to an abrupt switch of both the voltage and the differential resistance, followed by a constant differential resistance equal to the normal state resistance.

Decreasing the current from the normal state, a kink in the measured voltage signals a more subtle transition at $I = I_{c3}$. The measured voltage shows a small deficit with respect to its normal state value (black dashed line) suggesting the nucleation of superconductivity. We claim that superconductivity nucleates here at the ends of the wires close to the contact pads in agreement with Fig. 8.2b. The sudden transition at $I = I_{c4}$ is due to the transition from the bimodal to the global superconducting state.

A first experimental indication to support this interpretation is provided by Fig. 8.6c, which compares local measurements with measurements over the full wire. It shows the two-point resistance of the wire V_{12}/I_{12} (squares) as a function of bias current I_{12} , together with the apparent resistance V_{13}/I_{12} (triangles) at

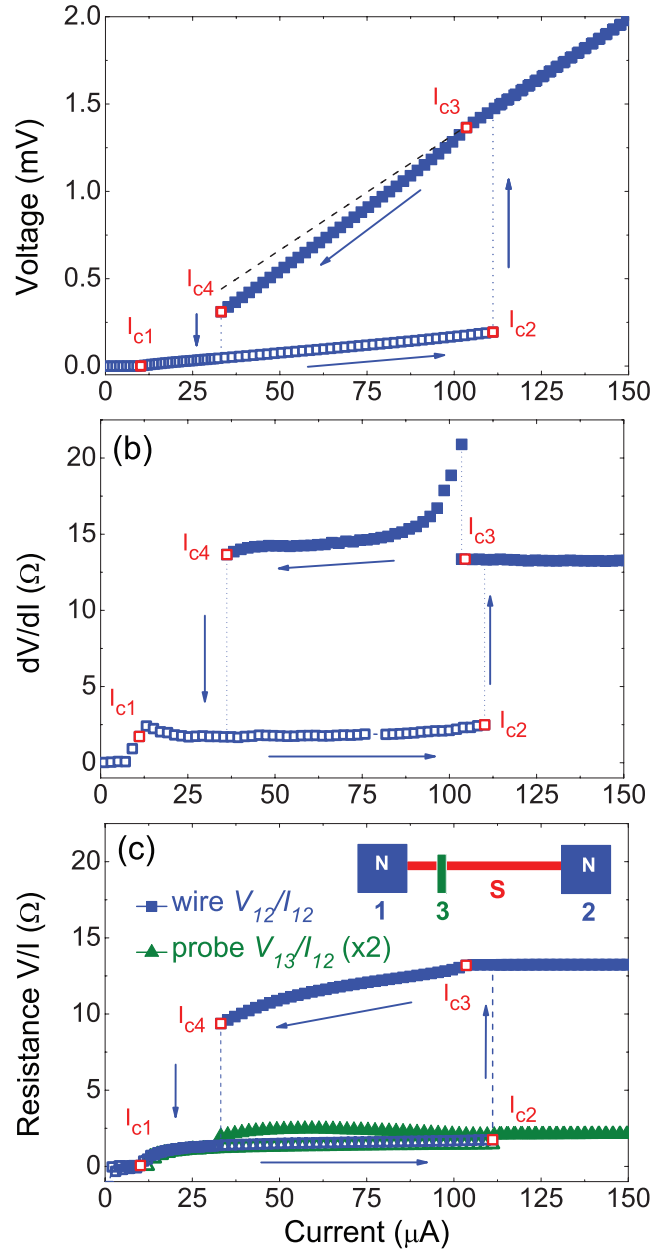


Figure 8.6: The voltage V_{12} (a) and differential resistance (b) of a $4 \mu\text{m}$ long wire (3b) as a function of bias current I_{12} , measured at 200 mK. We define four different regimes with boundaries labeled $I_{c1} - I_{c4}$, each characterized by a nearly constant differential resistance. The critical currents I_{c2} and I_{c4} are defined as the currents where the wire switches between the two hysteretic voltage branches. I_{c1} and I_{c3} are the transition points between the two different states of one branch. (c) The apparent resistance of the complete wire V_{12}/I_{12} , and of the edge of the wire V_{13}/I_{12} as measured with a voltage probe, multiplied by two for the ease of comparison.

the ends of the wire (see inset for the probe-position and terminal labels). The probe voltage is multiplied by two for comparison, as a similar contribution is present at the other edge of the wire. For the lower branch, the assumed global superconducting state, one observes that the voltage drop V_{13} over the end of the wire is almost identical to half of the complete voltage drop over the wire-length, a direct proof that this resistance is located at the ends of the wire.

In contrast, in the normal state, the voltages V_{12} and V_{13} are, as expected, proportional to their respective lengths along the wire, $V = \rho L/A$. Upon decreasing the bias below I_{c3} , where we assume the bimodal state exists, one observes over the full length of the wire a decreasing resistance for decreasing bias, signaling the growing strength of superconductivity somewhere. The measured resistance over the end of the wire, however, increases compared to the normal state $V_{13}/I_{12} \geq R_n$. Though counter-intuitive this is consistent with the general non-equilibrium present in the superconductor. In the following we make a detailed analysis of both superconducting states, and place the experimental results in the context of the theoretical model.

8.5.1 Global superconducting state

Figure 8.7 shows two-point measurements of the lower branch of a $1.4 \mu\text{m}$ long nanowire (Sample 1a) at three different bath temperatures. In view of the analysis shown Section 8.4.1 we assume that the resistance of the wire is primarily determined by the charge mode of the distribution function $f_T(E, x)$, which depends on the position dependent density of states and the order parameter $\Delta(x)$. The weak dependence of the differential resistance on the current indicates that the superconducting properties of the wire hardly change with increasing bias (open symbols). Though numerical simulations (filled symbols Fig. 8.7) show the same qualitative behavior, the simulations seem to overestimate the bias current at which the differential resistance begins to increase. Hence the observed switching current I_{c2} is also slightly lower than predicted. Ignoring this small discrepancy, the simulated data show good agreement with the experiment over the complete temperature range (inset Fig. 8.7). At the same time the observed values for the critical current (or critical voltage) are much smaller than what one would expect for a pair-breaking current, experimentally [27, 28], as well as theoretically [29, 30]. This demonstrates that the non-equilibrium processes should be taken into account in evaluating the parameters. The remaining deviations between theory and experiment suggest, most likely, that the temperature of the reservoirs deviate from the bath temperature for higher driving currents, as expected from Eq. (8.8).

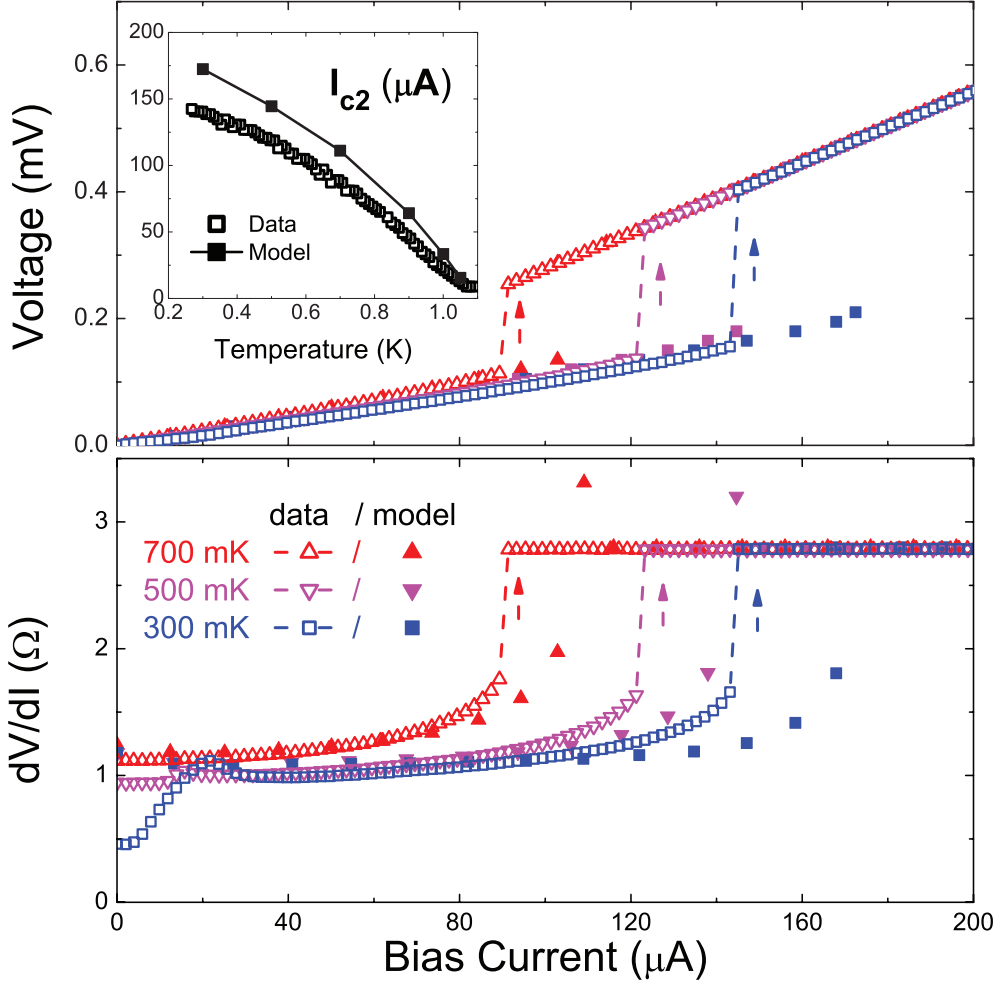


Figure 8.7: Two probe voltage (a) and differential resistance (b) as a function of bias current, for a $1.4 \mu\text{m}$ wire, at three different bath temperatures. Open symbols: experimental data. Filled symbols: numerical simulations. The critical current as a function of temperature (inset).

Figure 8.8a shows the differential conductance dI_{13}/dV_{13} of a tunnel probe, located at a distance of 320 nm ($=2.4 \xi$) from the normal reservoir of a $4 \mu\text{m}$ long wire (Sample 3b). The wire is biased at a fixed current I_{12} with a corresponding voltage V_{12} . At the same time the probe current I_{13} is varied while measuring the probe voltage V_{13} (Fig. 8.1b). The evolution of the local dos for increasing bias is shown on the right side in Fig. 8.8a. The conductance at zero bias $V_p = 0$ increases slightly for increasing bias, while the coherence peaks get further smeared out. The dependences are however weak, and even right before the switching current I_{c2} the dos is hardly affected by the drive current. These observations are in close agreement with the theoretical predictions and confirm the idea that the

superconducting state remains globally stable. For increasing bias the resistance remains located at the ends of the wire and the dos does not change either. Unfortunately, we have not been able to directly measure $f_L(x)$. Nevertheless we believe that this energy-mode non-equilibrium triggers the transition at I_{c2} as analyzed by Keizer et al [7].

8.5.2 Bimodal superconducting state

The continuous transition, with decreasing bias, from the normal into a superconducting state at I_{c3} (Fig. 8.6) indicates that the emerging superconducting state is initially very close to the normal state. For lower bias currents the absolute resistance gradually decreases (Fig. 8.6c), which suggests that an increasing fraction of the current is carried by the emerging condensate (Fig. 8.2b). A similar picture is observed for the local density of states, plotted in Fig. 8.8b for different bias currents I_{12} of the nanowire. Below I_{c3} a gradually increasing gap is found, unambiguously showing the emergence of superconducting order. Close to I_{c3} the dos at the position of the probe evolves in a continuous way from a flat spectrum into a spectrum with a gap. However at I_{c4} one observes an abrupt transition to a situation with a stronger gap. The abruptness indicates that it is a transition from two distinct superconducting states, which directly proves that at least two microscopically distinct superconducting states exist. Though the simulations for the local dos agree well at currents close to I_{c4} , they do not account in detail for the gradual evolution between the normal and superconducting state at I_{c3} . At this point we assume that the reservoirs start to heat up, and can no longer be treated as equilibrium reservoirs with $T = T_0$. Overall, the model supports the picture of the emergence of the superconducting state quite nicely, with the strongest non-equilibrium in the wire occurring at I_{c4} , with the reservoirs most closely to equilibrium at $T = T_0$.

The electro-chemical potential of the superconducting condensate, μ_{cp} , is determined from the minimum of the measured dos $\mu_{cp} = eV|_{\min(dos)}$. It is found that at this probe-position μ_{cp} is equal to the electrostatic potential V_1 of the adjacent reservoir. Measurements with a probe in the middle of the wire show that, in the same bias regime, the voltage is equal for both sides of the wire, which means that the state is symmetric, and a similar superconducting region should exist near the other reservoir at a potential V_2 . If these two regions were part of one global superconducting state, there would be a voltage drop $\Delta V = V_1 - V_2$ over the superconducting potential μ_{cp} of this state, and a superconducting phase-slip process should occur. However, according to the Josephson relation $2eV = \partial\chi/\partial t$ it would be at a frequency $\nu \approx 8\hbar/\Delta$, which is too high

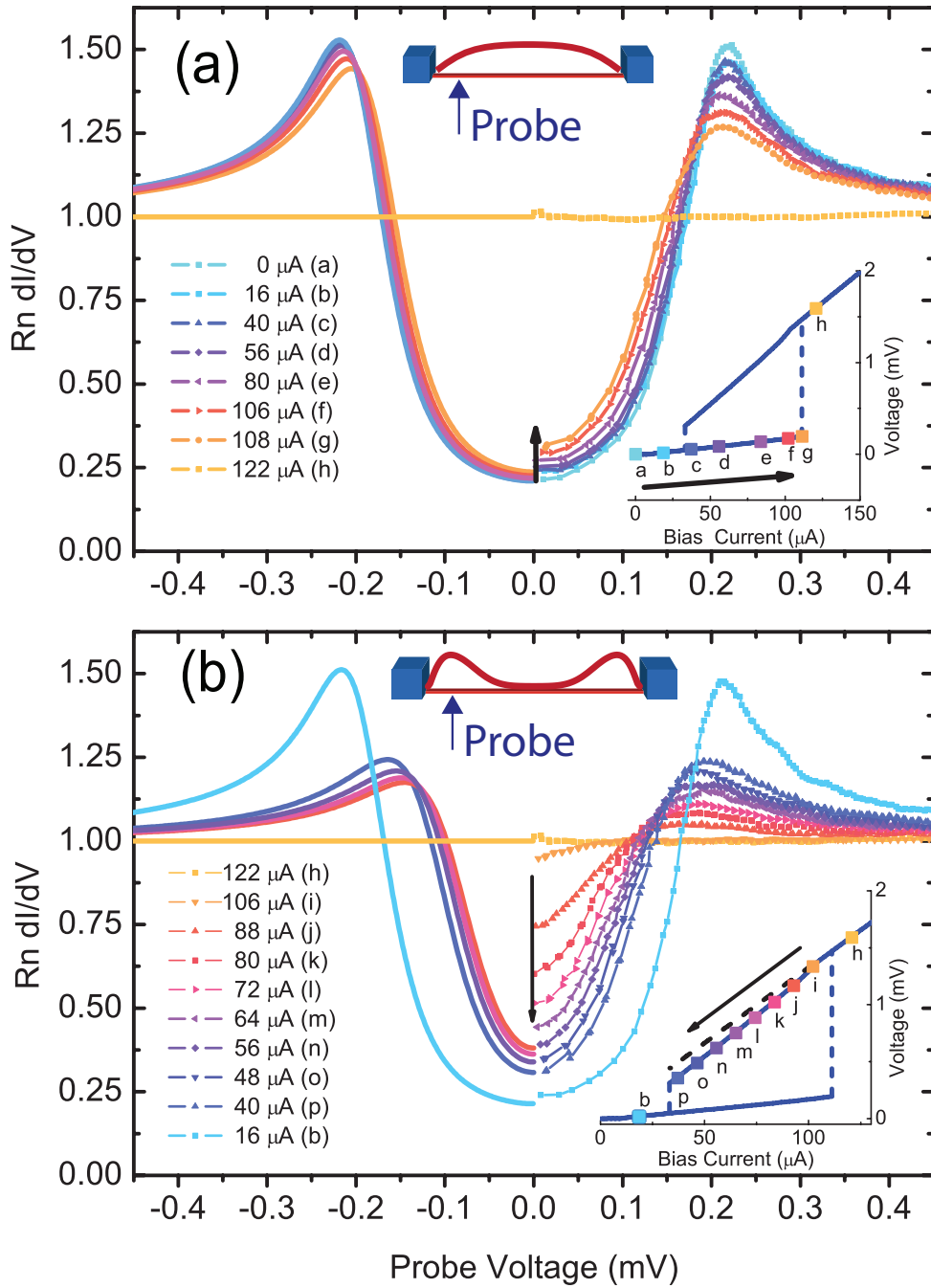


Figure 8.8: The local density of states for (a) the global superconducting state and (b) the bimodal state, for different bias currents I_{12} of the nanowire, measured at 200 mK. For the global superconducting state the gap is only weakly dependent on the bias current, while for the bimodal state one observes a dos gradually changing from a normal into a superconducting state.

compared to the energy-gap.

The fact that the two-point resistance is so close to R_n , the gradual increase of the dos at the position of the probe, and the electro-chemical potential of the condensate demonstrate that two separate superconducting regions emerge at the edges of the wire. The physical reason is the energy mode non-equilibrium, as discussed by Keizer et al [7] for the lower branch, but similarly for this upper branch. At the bias I_{c4} the wire is still largely normal and f_E is given by the two step distribution-function. In the middle of the wire the width of the step is several times bigger than the superconducting gap. Through relation Eq. (8.6) it is seen that this suppresses fully the nucleation of a gap, while the cold equilibrium reservoirs favor the emergence of a gap at the edges of the wire. Simply put, the ends are cold where the centre of the wire is hot. Therefore we conclude that the results are most easily understood as due to two distinct superconducting domains, separated by a normal central region, what we have called the bimodal state.

Finally, we discuss the voltage V_{13} measured by the probe when the wire is biased into the bimodal state (triangles Fig. 8.6c). Close to T_c the voltage measured by such a normal probe is equal to the electrochemical potential of the quasiparticle bath [17]. At low temperatures [16] and for short-lived quasiparticles [18] it is impossible to define a quasiparticle bath with a well-defined chemical potential, however the measured voltage is still related to the local electrostatic potential $e\phi$ (using Eq. 8.10):

$$e\phi = - \int_{-\infty}^{\infty} N(E) f_T^N(E + eV) dE. \quad (8.11)$$

For a relatively small charge imbalance $e\phi(x) \ll \Delta$, the measured voltage equals the local electrostatic potential $e\phi(x)$ divided by the local dos in the superconductor at zero energy: $V \approx \phi/N(0)$. Hence the voltage measured with the tunnel probe can be larger than the local potential $e\phi(x)$.

8.6 Conclusion

We have analyzed a well-defined model-system of a superconducting wire between two massive normal contact pads. We demonstrate that this NSN system, when driven by a current, has two distinct metastable superconducting states.

For low bias we find a global superconducting state with most of the resistance occurring as a current-conversion resistance at the ends of the superconducting wires where normal current enters. Although resistive we demonstrate that the

whole wire including the edges continues to be in one coherent superconducting state. This state does hardly change for increasing current, until the wire switches abruptly to the full normal state at a current, which is much lower than the critical pair-breaking current. On a microscopic level the distribution function changes considerably and is strongly different from the commonly used parabolic temperature profile. A numerical analysis based on the non-equilibrium quasi-classical Green's functions shows that the switching current is determined by the non-equilibrium electron distributions, in good agreement with the experimental results.

For high bias, decreasing the current from a fully normal state, we find that the superconducting state emerges as two decoupled domains at the ends of the wire. The vicinity of the cool equilibrium reservoirs favors the nucleation of the superconducting state at these ends, while strong non-equilibrium at the center of the wire continues to suppress the superconductivity. Upon further lowering of the bias current the two domains grow in strength until the wire switches back to the low resistive, globally superconducting state. We speculate, that the transition from one state to the other, is triggered by a condition in which the Josephson coupling energy between the two domains exceeds the thermal energy at that bias point.

This work is also relevant for normal metal-superconductor-normal metal mixing devices, called hot-electron bolometer (HEB) mixers [31]. In most practical cases the superconducting material is thin NbN and gold (Au) normal pads are used as antenna. Under the condition that no radiation is applied to an HEB, the present analysis is helpful to understand the observed current-voltage characteristics, which are analogous to the one shown in Fig. 8.6a [32]. The resistive properties for low bias and temperature will be dominated by the conversion resistance at the interfaces (controlled by f_T). This regime will extend to a critical current, analogous to I_{c2} reported here, but with a value which may depend on the electron-phonon relaxation which is present in a material like NbN, but is negligible in our experiment with Al. Beyond this critical value the device is most likely either fully in the normal state (beyond I_{c3} as identified here), or in the bimodal state (for lower biases between I_{c3} and I_{c4}). The stronger electron-electron and electron-phonon interaction in NbN as compared to Al, will bring the longitudinal non-equilibrium, f_L , closer to a local thermal profile. In case radiation is applied to an HEB an overall increase in electron temperature occurs, which brings the superconductor close to its transition point where thermally activated phase slip events contribute to the resistivity. Hence, for a full understanding of the HEB mixers one needs to take into account two contributions to the observed resistance: first the static conversion resistance inside the super-

conductor near the interface between the normal metal and the superconductor, described here, dominating for the unexposed devices, and second the resistance due to time-dependent phase-slip events occurring at electron temperatures close to the critical temperature of the superconductor, which dominates under actual mixer operation [4].

We would like to acknowledge Nanofridge (Nanosci-ERA), Microkelvin (No. 228464, Capacities Specific Programme) and the Foundation for fundamental research on matter (FOM).

References

- [1] A. V. Gurevich and R. G. Mints, *Self-heating in normal metals and superconductors*, Rev. Mod. Phys. **59**, 941 (1987).
- [2] M. Tinkham, J. U. Free, C. N. Lau, and N. Markovic, *Hysteretic $I - V$ curves of superconducting nanowires*, Phys. Rev. B **68**, 134515 (2003).
- [3] N. Shah, D. Pekker, and P. M. Goldbart, *Inherent Stochasticity of Superconductor-Resistor Switching Behavior in Nanowires*, Phys. Rev. Lett. **101**, 207001 (2008).
- [4] R. Barends, M. Hajenius, J. R. Gao, and T. M. Klapwijk, *Current-induced vortex unbinding in bolometer mixers*, Appl. Phys. Lett. **87**, 263506 (2005).
- [5] H. Pothier, S. Guéron, N. O. Birge, D. Esteve, and M. H. Devoret, *Energy Distribution Function of Quasiparticles in Mesoscopic Wires*, Phys. Rev. Lett. **79**, 3490 (1997).
- [6] A. Schmid and G. Schön, *Linearized kinetic equations and relaxation processes of a superconductor near T_c* , J. of Low Temp. Phys. **20**, 207 (1975).
- [7] R. S. Keizer, M. G. Flokstra, J. Aarts, and T. M. Klapwijk, *Critical Voltage of a Mesoscopic Superconductor*, Phys. Rev. Lett. **96**, 147002 (2006).
- [8] A. Sanchez-Canizares and F. Sols, *Self-Consistent Theory of Transport in QuasiOne-Dimensional Superconducting Wires*, J. of Low Temp. Phys. **122**, 11 (2001).
- [9] G. R. Boogaard, A. H. Verbruggen, W. Belzig, and T. M. Klapwijk, *Resistance of superconducting nanowires connected to normal-metal leads*, Phys. Rev. B **69**, 220503 (2004).
- [10] W. J. Skocpol, M. R. Beasley, and M. Tinkham, *Self-heating hotspots in superconducting thin-film microbridges*, J. Appl. Phys. **45**, 4054 (1974).

-
- [11] A. F. Volkov and S. M. Kogan, *Temperature domains in superconductor films*, JETP Lett **19**, 4 (1974).
- [12] N. Kopnin, *Theory of Nonequilibrium Superconductivity*, International Series of Monographs on Physics Vol. 110, Oxford University Press, New York, 2001.
- [13] K. D. Usadel, *Generalized Diffusion Equation for Superconducting Alloys*, Phys. Rev. Lett. **25**, 507 (1970).
- [14] I. Snyman and Y. V. Nazarov, *Bistability in voltage-biased normal-metal / insulator / superconductor / insulator / normal-metal structures*, Phys. Rev. B **79**, 014510 (2009).
- [15] T. H. Stoof and Y. V. Nazarov, *Kinetic-equation approach to diffusive superconducting hybrid devices*, Phys. Rev. B **53**, 14496 (1996).
- [16] J. Clarke, *Experimental Observation of Pair-Quasiparticle Potential Difference in Nonequilibrium Superconductors*, Phys. Rev. Lett. **28**, 1363 (1972).
- [17] C. J. Pethick and H. Smith, *Relaxation and collective motion in superconductors - 2-fluid description*, Ann. of Phys. **119**, 133 (1979).
- [18] J. B. Nielsen, C. J. Pethick, J. Rammer, and H. Smith, *Pair breaking and charge relaxation in superconductors*, J. of Low Temp. Phys. **46**, 565 (1982).
- [19] F. Hübner, J. C. Lemyre, D. Beckmann, and H. v. Löhneysen, *Charge imbalance in superconductors in the low-temperature limit*, Phys. Rev. B **81**, 184524 (2010).
- [20] R. Yagi, *Charge imbalance observed in voltage-biased superconductor-normal tunnel junctions*, Phys. Rev. B **73**, 134507 (2006).
- [21] P. Santhanam and D. E. Prober, *Inelastic electron scattering mechanisms in clean aluminum films*, Phys. Rev. B **29**, 3733 (1984).
- [22] M. Serbyn and M. A. Skvortsov, *Onset of superconductivity in a voltage-biased normal-superconducting-normal microbridge*, Phys. Rev. B **87**, 020501 (2013).
- [23] S. B. Kaplan, C. C. Chi, D. N. Langenberg, J. J. Chang, S. Jafarey, and D. J. Scalapino, *Quasiparticle and phonon lifetimes in superconductors*, Phys. Rev. B **14**, 4854 (1976).
- [24] F. Pierre, A. Anthore, H. Pothier, C. Urbina, and D. Esteve, *Multiple Andreev Reflections Revealed by the Energy Distribution of Quasiparticles*, Phys. Rev. Lett. **86**, 1078 (2001).

- [25] M. Henny, S. Oberholzer, C. Strunk, and C. Schönenberger, *1/3-shot-noise suppression in diffusive nanowires*, Phys. Rev. B **59**, 2871 (1999).
- [26] N. W. Ashcroft and N. D. Mermin, *Solid State Physics*, Saunders College, New York, 1976.
- [27] J. Romijn, T. M. Klapwijk, M. J. Renne, and J. E. Mooij, *Critical pair-breaking current in superconducting aluminum strips far below T_c* , Phys. Rev. B **26**, 3648 (1982).
- [28] A. Anthore, H. Pothier, and D. Esteve, *Density of States in a Superconductor Carrying a Supercurrent*, Phys. Rev. Lett. **90**, 127001 (2003).
- [29] M. Y. Kupriyanov and V. F. Lukichev, *Sov. J. Low Temp. Phys.* **6**, 210 (1980).
- [30] J. Bardeen, *Critical Fields and Currents in Superconductors*, Rev. Mod. Phys. **34**, 667 (1962).
- [31] D. E. Prober, *Superconducting terahertz mixer using a transition-edge microbolometer*, Appl. Phys. Lett. **62**, 2119 (1992).
- [32] M. Hajenius, Z. Q. Yang, J. R. Gao, J. J. A. Baselmans, T. M. Klapwijk, B. Voronov, and G. Goltsman, *Optimized sensitivity of NbN hot electron bolometer mixers by annealing*, IEEE Trans. on Appl. Supercond. **17**, 399 (2007).

Chapter 9

Spin-dependent current conversion in a superconducting wire

We have measured two probe transport properties of superconducting aluminum wires between ferromagnetic cobalt pads. We observe a resistance, which is due to the conversion of a spin polarized current into a supercurrent and depends on the orientation of the magnetization of the cobalt pads. Compared to the normal state the spin dependence of the conversion resistance is strongly enhanced, even though the resistance of the wire is reduced. A similar dependence is seen in the critical current of the wires. The spin dependence of the superconducting state makes it possible to investigate induced magnetism in these Al wires, for example using local ferromagnetic tunneling probes.

9.1 Superconducting proximity effect in ferromagnets

Superconductivity and ferromagnetism are two different, electronic phases exhibiting long range order, which are seemingly incompatible. In a superconductor, electrons of opposite spin and momentum condense to form spin-neutral (singlet) Cooper pairs. In contrast, the electron spins in a ferromagnet align due to an effective exchange interaction. The magnetic exchange field h induces a Zeeman splitting between the energy bands of spin-up and spin-down electrons, which results in a spin dependent shift in the electronic wave vectors $k_{F\uparrow}, -k_{F\downarrow}$ at the Fermi-level. This means that in the presence of an exchange field, Cooper pairs acquire a net momentum $\delta k = k_{F\uparrow} - k_{F\downarrow}$ which causes the phase of the pairs to oscillate in space. Dephasing between spin-up and spin-down electrons results in a suppression of the pair amplitude.

However, already in 1964 a state was proposed in which superconductivity and ferromagnetism could coexist [1, 2, 3]. In this state the magnetization would rotate over a length scale which is small compared to the superconducting coherence length ξ . Therefore the Cooper pairs sample different magnetic domains and do not suffer from the paramagnetic pair breaking. Experimentally, this state has not been observed until today. Ferromagnet superconductor hybrid structures in contrast, allow to study the coexistence of both states in a controlled environment. The spatial oscillation of the pairing amplitude has been observed in SFS trilayers, where the thickness of the sandwiched ferromagnet was varied. Both a predicted sign change in the supercurrent as a nonmonotonic dependence of the superconducting critical temperature have been confirmed experimentally [4, 5].

The discovery of a long range proximity effect in ferromagnetic wires [6, 7] revived the idea of spin triplet superconductivity [8], inspired by a model for superfluid He3 [9]. These triplet Cooper pairs consist of electrons with a parallel spin which do not suffer from dephasing in an exchange field. To survive in a disordered environment, it is required that their wave function is even in space, but odd in frequency [10]. In 2006, strong indications for the existence of odd triplet superconductivity were given by the observation of long range supercurrents through the 100 % spin-polarized half metal CrO₂ by Keizer et al [11].

Initially the generation of the triplet components was attributed to the presence of a rotating magnetization, such as can be found in a magnetic domain wall. However it became clear that the interface between the ferromagnet and the superconductor can play a major role [12, 13]. It can contain spin active scatterers,

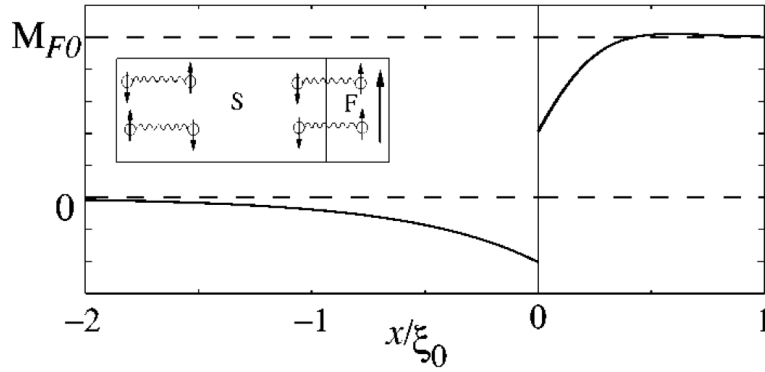


Figure 9.1: The magnetization of a superconductor-ferromagnet bilayer [16]. The induced magnetization in the superconductor can be paramagnetic or diamagnetic, depending on the microscopic properties of the interface [17].

or break time reversal symmetry. The triplet component can be generated near the interface, in the ferromagnet (weak magnetization) or in the superconductor (strong ferromagnet). Experimentally, reproducible control over the generation of a triplet supercurrent has been achieved by the inclusion of a misaligned Co layer in a SFS multilayer stack [14]. More recently, the use of the helical ferromagnet Holmium serves as a generator of triplet superconductivity [15].

9.2 Induced magnetism in superconductors

The theoretical and experimental efforts to understand the superconducting proximity effect in a ferromagnet, have led to a variety of unanticipated effects and rich physics. The inverse effect, an induced magnetization in a superconductor by the proximity of a ferromagnet, has been proposed theoretically but has hardly been studied experimentally. Theoretically, a superconductor can acquire a magnetization which is parallel or anti-parallel to the one of the ferromagnet, depending on the transparency of the interface [16, 17]. An open question is how the inverse proximity effect would be affected by the presence of triplet pair correlations, e.g. on the density of states or (spin dependent) Andreev reflection. Experimentally, the effect of a ferromagnet on a superconductor is mainly studied from a perspective in which the main focus lies on spin injection in evanescent or long-lived quasi-particle states [18, 19] or crossed Andreev reflection and entanglement [20, 21]. Only in a recent paper, an induced magnetization in a superconductor is explicitly assessed by use of the polar Kerr effect [22].

In this experiment we focus on the influence of ferromagnetic Co contacts on the superconducting properties of Al nanowires (Fig. 9.2). Our main interest

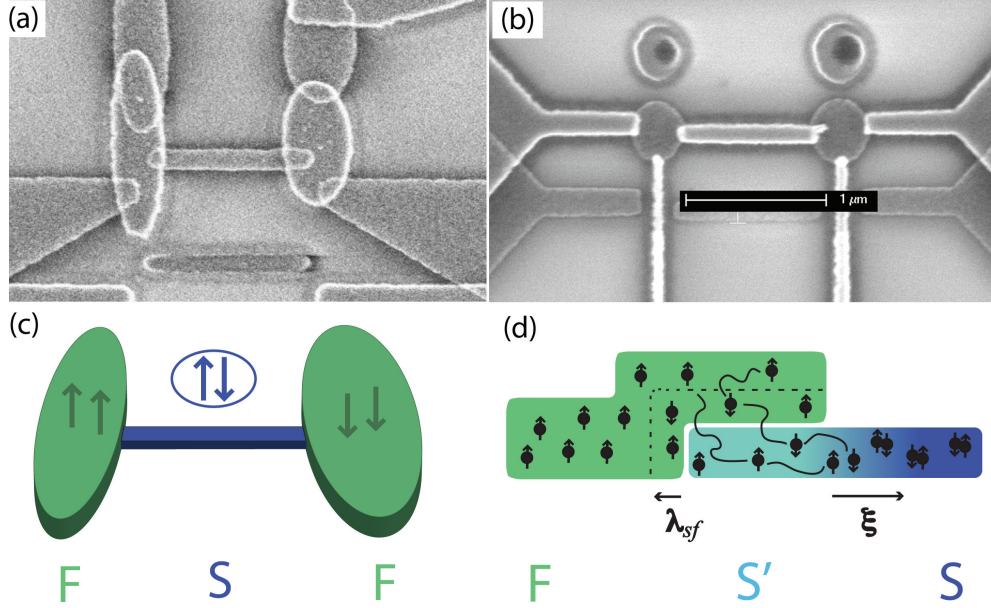


Figure 9.2: A superconducting Al nanowire connected to two ferromagnetic pads. SEM pictures of two different designs (a) and (b). Schematic model of the structure (c) and the current conversion process (d).

is the interaction between the ferromagnetic and superconducting ground state, rather than the injection of long-lived quasiparticles. Therefore we use samples with a clean interface, and measure at low temperatures and voltages, $k_B T, eV \ll \Delta$. We demonstrate that the two-point resistance of the Al wire is a sensitive probe for the conversion processes near the interface, from a normal spin-polarized current into a supercurrent.

In addition, the different geometry of the Co contacts allows us to change their relative magnetization by applying a parallel magnetic field. We demonstrate that the linear two-point resistance of the superconducting wires depends strongly on the local spin polarization of the Co contacts. Although the resistance of the superconducting wires is much smaller than in the normal state, this spin dependent contact resistance is much bigger in the superconducting case, even in absolute numbers.

We observe a similar behavior in the magnetic field dependence of the critical current. A higher resistance results in a lower critical current, as both the dissipation as the bias voltage for a fixed current scale with $R(H)$. At slightly larger fields we observe a strong enhancement of the critical current. This effect has been observed before in various superconducting wires, and has been attributed both to suppression of spin flip scattering [23, 24].

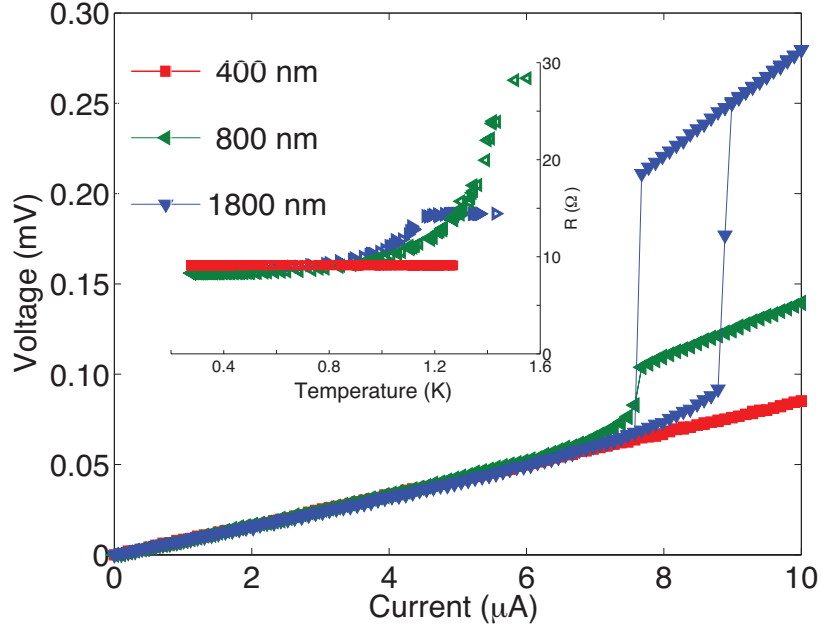


Figure 9.3: The current voltage characteristic of samples 2a-2c, measured at a bath temperature of 300 mK. (inset) At low temperature, the longer wires (800 & 1800 nm) have the same current conversion resistance (symbols: data, lines: model). The shortest wire (400 nm) does not become superconducting.

9.3 Current conversion resistance and nonlinear response

Figs. 9.2a and 9.2b show the two sample geometries measured. They consist of a 100 nm wide Al superconducting wire, contacted by two elliptic Co ferromagnetic pads. The structures are realized using shadow evaporation through a PMMA/PGMI double resist layer, at a base pressure of 1×10^{-7} mbar. First 20 nm Al is evaporated under an angle of 30° to create the superconducting wire. In a second step a 35 nm Co layer is deposited under an angle of -30° to form the contacts. The time between the two depositions is kept to a minimum (circa 10 min) to ensure a clean interface. The samples measured are fabricated in two runs (1 and 2), the properties are listed in Table 9.1.

The resistance of three wires with a length between 400 and 1800 nm is shown as a function of temperature in the inset of Fig. 9.3. The onset of superconductivity is observed as a steep drop in the resistance, as the temperature is decreased below 1.4 K for the 1800 nm wire and 1.1 K for the 800 nm wire. In the shortest, 400 nm long wire no transition is measured. All of the three wires keep a finite

#	L (μm)	A (nm^2)	R_n (Ω)	ρ ($\mu\Omega\text{cm}$)	T_c (K)	ξ (nm)	R_s (Ω)
1a	1.0	100 x 20	25	4.42	-	80	12
1b	2.0	100 x 20	40	3.61	-	88	11
2a	0.4	100 x 20	8	2.87	<0.3	99	8.75
2b	0.8	100 x 20	14	2.75	1.2	101	8.5
2c	1.8	100 x 20	28	2.77	1.4	101	8

Table 9.1: Overview of the properties of the different samples: L - length, A - cross-section ($w \times t$ - width times thickness), R_n - normal state resistance, ρ - resistivity, T_c - critical temperature, $\xi = \sqrt{\hbar D / 2\Delta}$ - coherence length, R_s - low temperature resistance in the superconducting state.

resistance down to the lowest temperature. This resistance has two contributions: (a) a contact resistance R_c located in the contact pads and (b) a current conversion resistance R_s in the superconducting wire. The value of the contact resistance R_c can be estimated as $R_c \approx 2 \times 1.5\Omega$ from the length dependence of the normal resistance $R_n = \rho L / A + R_c$. The remaining resistance R_s is due to current conversion processes in the superconducting wire, near the interfaces with the ferromagnetic contacts. In the superconductor, only a fraction of the current in the superconductor is carried by evanescent normal electrons, which can carry spin. These states, and thus the spin current in a superconductor, decay exponentially on a length scale of a superconducting coherence length ξ as the normal current is converted into a supercurrent. This conversion process results in a dc electric field in the superconductor, and hence a resistance.[25, 26] The conversion of a spin polarized current into an almost spinless current on the other hand occurs mainly in the ferromagnet, as the spin flip length in our Co pads is much shorter than in the Al wire. This leads to a spin accumulation at the interface, and a potential drop $\Delta\mu$.

The response of the nanowires to driving with a current bias is shown in Fig. 9.3, measured at 300 mK when the wire is in the superconducting state. For increasing current, the resistance of the wire is relatively constant until the wire switches abruptly to the normal state at a critical current I_c . This current is well below the pair breaking current expected for these wires. In the previous chapter, we discussed how I_c can be suppressed, because the injection of evanescent quasiparticle states creates a non-thermal non-equilibrium throughout the driven nanowire. In this case however, the reduction of I_c is considerably larger. This might indicate an influence of the spin-polarization of the reservoirs, although heating effects in the reservoirs can not be excluded in this particular geometry.

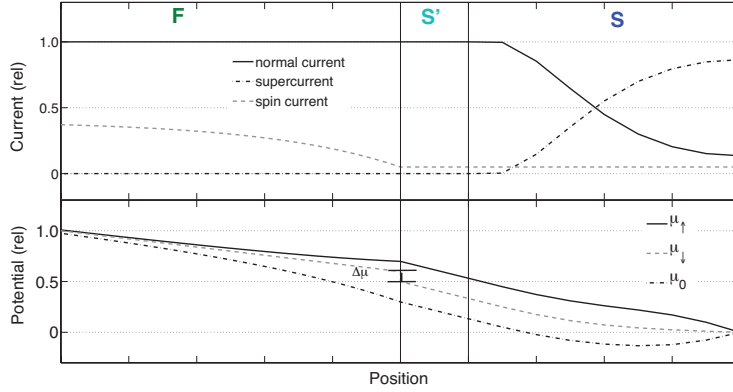


Figure 9.4: (a) The conversion of a spin-polarized normal current into a supercurrent leads to spin accumulation in the ferromagnet, and to charge accumulation in the superconductor (b). Both processes contribute to the total current conversion resistance but in our structures the potential drop in the superconducting wire is dominant.

9.4 Model for spin transport in superconductors

To include spin effects into the model used in Refs. [25] and [26], we model the sample as depicted in Fig. 9.2c. Given the short elastic mean free path l_e we assume the transport is diffusive, and adopt a two channel (spin-up and spin-down) model [27]. We divide the structure in three different diffusive regions (Fig. 9.2d), and match the spin dependent currents and potentials at the interfaces between them. The transport properties in the ferromagnet (region I) are determined by a spin dependent conductivity $\sigma_{\uparrow,\downarrow}$, which relate the current of each spin channel to its spin specific potential: $j_{\uparrow,\downarrow} = \sigma_{\uparrow,\downarrow} \nabla \mu_{\uparrow,\downarrow}$. An imbalance between spin-up and spin-down electrons relaxes through spin flip processes over a length $\lambda_{sf} = \sqrt{D\tau_{sf}}$:

$$D \frac{\partial^2 (\mu_{\uparrow} - \mu_{\downarrow})}{\partial x^2} = \frac{\mu_{\uparrow} - \mu_{\downarrow}}{\tau_{sf}}, \quad (9.1)$$

with D the spin averaged diffusion constant, and τ_{sf} the spin relaxation time. The second region consists of the edge of the Al wire, and is driven normal by the presence of the overlapping ferromagnetic pad. The superconducting wire (region III) is described using the Usadel equations for dirty superconductors [28, 29], with spin dependent distribution functions [30]. We assume our Al wires are one dimensional, and short enough to ignore inelastic relaxation [31].

The resulting currents and potentials are schematically drawn in Fig. 9.4. Deep in the ferromagnet the current is fully normal and has a spin polarization

$\alpha_F = \frac{\sigma_{\uparrow} - \sigma_{\downarrow}}{\sigma_{\uparrow} + \sigma_{\downarrow}}$. In contrast, almost all current in the superconductor is carried by spinless singlet Cooper pairs as a supercurrent. This means two conversion processes are taking place; a change in spin current and a conversion from a normal into a supercurrent. The conversion of a normal current into a supercurrent requires the presence of a superconducting gap Δ and can only happen in the superconducting wire itself (region III). The conversion occurs over roughly a coherence length ξ and leads to dc electric field in the superconducting wire $R_s \approx \xi\rho/A$, with ρ the resistivity and A the crosssection of the wire. The spin current in the superconductor is carried by the small normal fraction of the current and is proportional to $\exp(\xi/L)$.

This means we can apply the analysis of Refs. [25] and [26] to the temperature dependence of the zero bias resistance of the different wires. The resistance which follows from this analysis is consistent with the measurements. However, the used superconducting critical temperature T_{c0} differs from wire to wire, while they were fabricated in the same batch. This is also apparent from the resistance versus temperature characteristic, where one would expect that the different curves would overlap below the superconducting transition. The change in spin current $J_s = j_{\uparrow} - j_{\downarrow}$ leads to spin accumulation near the interface between the different regions, over a material specific spin relaxation length λ_{sf} . For the Co pads this length ($\lambda_{sf} \approx 5\text{-}50$ nm) is much shorter than for the Al wire ($\lambda_{sf} \approx 1$ μm). Therefore the major part of the spin current conversion occurs in the ferromagnet, leading to an extra resistance:

$$R_{conv} = \frac{\alpha_F^2 (R_s A)^{-1}}{(1 - \alpha_F^2) \sigma_f \lambda_{sf}^{-1} + (R_{spin} A)^{-1}} R_s, \quad (9.2)$$

The fact that the ‘total’ resistance of the superconductor is very low, while the ‘spin’ resistance is high means an increase in spin accumulation at the interface. In addition a long spin flip length λ_{sf} or higher spin polarization α_F will also give rise to an increased spin conversion resistance.

In linear response this leads to a decoupled total current J and spin current J_{spin} in the superconductor:

$$\begin{aligned} J &= j_{\uparrow} + j_{\downarrow} = \frac{\mu_{\uparrow} + \mu_{\downarrow}}{R_s}, R_s \approx \frac{\xi\rho}{A}, \\ J_{spin} &= j_{\uparrow} - j_{\downarrow} = \frac{\mu_{\uparrow} - \mu_{\downarrow}}{R_{spin}}, R_{spin} \approx \frac{\exp(\xi/L)\rho}{A}. \end{aligned} \quad (9.3)$$

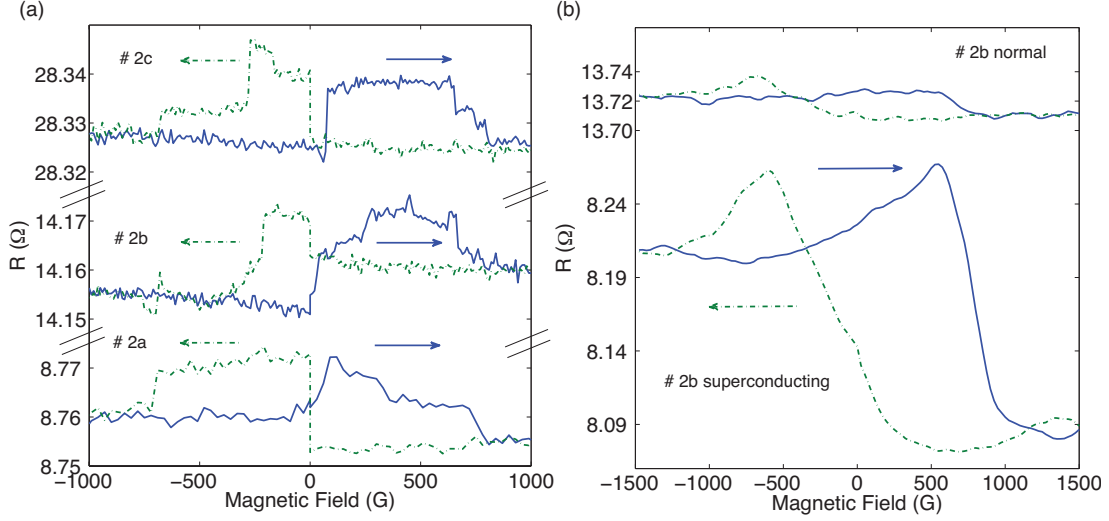


Figure 9.5: (a) The normal state resistance shows hysteretic switching in a parallel magnetic field. (b) The spin dependence of the resistance in the superconducting (lower) state correlates with the one in the normal (upper) state, but is much stronger.

9.5 Magnetic field dependence and spin switching

To study spin-polarized transport in the superconducting state of the Al nanowires, we measure the dependence of the conversion resistance R_s and the critical current I_c on the relative spin orientation of the Co contacts (parallel or anti-parallel). Because of the difference in width, the pads have different coercive fields. In a parallel magnetic field, the wider contact pad will switch its magnetization first, creating a situation in which the Co pads are oriented anti-parallel. If the field is increased further, the more narrow pad will also switch and the magnetizations are again parallel.

Fig. 9.5a shows the magnetic field dependence of the normal resistance R_n of the Al wires at 4.2 K. Abrupt changes in R_n are observed for each of the samples, indicating switches in the magnetization of the Co contacts. The size of the switching effect is roughly $\Delta R_n = R_{\uparrow\uparrow} - R_{\uparrow\downarrow} \approx 10 \text{ m}\Omega$ and seems not to depend on the length of the wire, while one expects an inverse or even exponential dependence:

$$\begin{aligned} \Delta R_n &\sim 1/L, L \ll \lambda_{sf} \\ \Delta R_n &\sim \exp(-L/\lambda_{sf}), L \gg \lambda_{sf} \end{aligned} \quad (9.4)$$

Possibly this discrepancy is related to magnetoresistance effects in the ferromag-

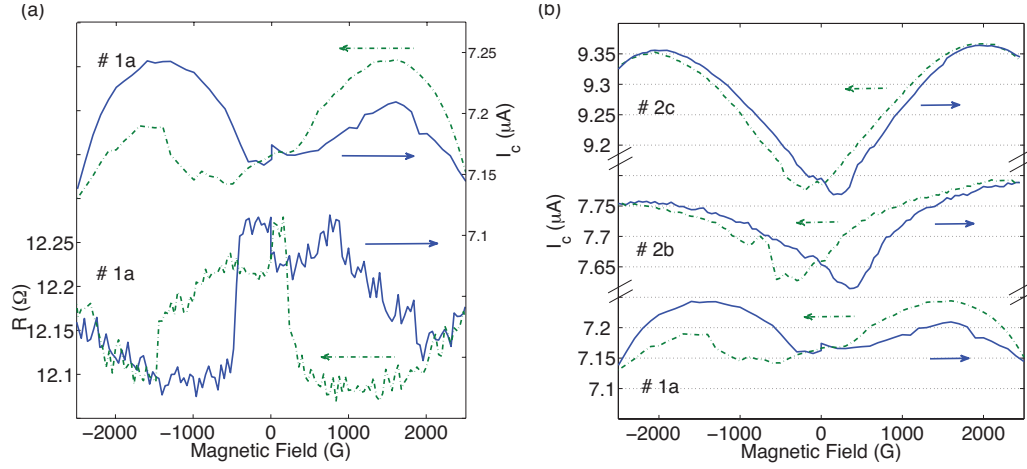


Figure 9.6: (a) The hysteretic behavior of the current conversion resistance R_s is also observed in the critical current I_c . (b) In the magnetic field dependence of the critical current three different regions are observed. At low magnetic fields spin switching is observed, similar to the effects observed in the two-point resistance. At intermediate fields the critical current is enhanced, before superconductivity is suppressed at high fields.

netic contact pads (changes in magnetic domains at the interface). In principle these can be excluded by performing nonlocal spin detection, but in this sample geometry such a measurement is not possible.

In the superconducting state we observe a similar dependence of the conversion resistance R_s on magnetic field. Fig. 9.5b compares the magnetic field dependence of R_n and R_s of wire 2b. Although the resistance changes ΔR are much bigger in the superconducting state, the transitions are less abrupt than in the normal state. In addition there is a relatively large asymmetry in the resistance at positive and negative magnetic fields, which is much less pronounced in the normal state.

The magnetic field dependence of the critical current is shown in Fig. 9.6. We distinguish three different effects : (a) at relatively low magnetic fields (0-500 mT), the critical current changes abruptly (b) at intermediate fields we observe an enhancement of I_c , and (c) at high magnetic fields the critical current is suppressed. The suppression at high fields can be understood as depairing of the Cooper pairs due to a paramagnetic field effect. The upper critical fields measured are of the order of a few Tesla, which is in agreement with our film properties. An enhancement of the critical current has been observed in previous measurements on thin Al wires and is attributed to the presence of spin flip scatterers at the surface [23, 24].

9.6 Conclusions and recommendations

We studied the current conversion resistance of a ferromagnet-superconductor interface. We found the resistance to be dependent on the local polarization of the ferromagnetic pads, and the effect is strongly enhanced in the superconducting state compared to the normal state. The same dependencies are observed in the critical current of the wires. At intermediate fields we observe an enhancement of the critical current, an effect which we do not observe in the resistance. This indicates the nature of the effect is different from charge imbalance relaxation in the superconductor. The consistent behavior of the two probe resistance, together with the spin dependence of the superconducting state, proves this system is promising to improve the understanding of induced magnetism in superconductors. Therefore it would be attractive to measure the magnetization and the density of states of the wires locally with respectively ferromagnetic and normal tunneling probes in a future experiment.

We would like to acknowledge Nanofridge (Nanosci-ERA), Microkelvin (No. 228464, Capacities Specific Programme) and the Foundation for fundamental research on matter (FOM) for financial support.

References

- [1] A. Larkin and Y. Ovchinnikov, *Zh. Eksp. Teor. Fiz.* **47**, 1136 (1964).
- [2] A. Larkin and Y. Ovchinnikov, *Inhomogeneous State of Superconductors*, *Sov. Phys. JETP* **20**, 762 (1965).
- [3] P. Fulde and R. A. Ferrell, *Superconductivity in a Strong Spin-Exchange Field*, *Phys. Rev.* **135**, A550 (1964).
- [4] F. S. Bergeret, A. F. Volkov, and K. B. Efetov, *Odd triplet superconductivity and related phenomena in superconductor-ferromagnet structures*, *Rev. Mod. Phys.* **77** (2005).
- [5] A. I. Buzdin, *Proximity effects in superconductor-ferromagnet heterostructures*, *Rev. Mod. Phys.* **77**, 935 (2005).
- [6] M. Giroud, H. Courtois, K. Hasselbach, D. Mailly, and B. Pannetier, *Superconducting proximity effect in a mesoscopic ferromagnetic wire*, *Phys. Rev. B* **58**, R11872 (1998).
- [7] V. T. Petrashov, I. A. Sosnin, I. Cox, A. Parsons, and C. Troadec, *Giant Mutual Proximity Effects in Ferromagnetic/Superconducting Nanostructures*, *Phys. Rev. Lett.* **83**, 3281 (1999).

-
- [8] F. S. Bergeret, A. F. Volkov, and K. B. Efetov, *Long-Range Proximity Effects in Superconductor-Ferromagnet Structures*, Phys. Rev. Lett. **86**, 4096 (2001).
- [9] V. Berezinskii, *New model of the anisotropic phase of superfluid He3*, JETP Lett. **20**, 287 (1975).
- [10] M. Eschrig, T. Lfwander, T. Champel, J. C. Cuevas, J. Kopu, and G. Schön, *Symmetries of Pairing Correlations in Superconductor-Ferromagnet Nanostructures*, J. of Low Temp. Phys. **147**, 457 (2007).
- [11] R. S. Keizer, M. G. Flokstra, J. Aarts, and T. M. Klapwijk, *Critical Voltage of a Mesoscopic Superconductor*, Phys. Rev. Lett. **96**, 147002 (2006).
- [12] M. Eschrig, *Spin-polarized supercurrents for spintronics*, Phys. Today **64**, 43 (2011).
- [13] M. Eschrig and T. Lfwander, *Triplet supercurrents in clean and disordered half-metallic ferromagnets*, Nat. Phys **4**, 138 (2008).
- [14] T. S. Khaire, M. A. Khasawneh, W. P. Pratt, and N. O. Birge, *Observation of Spin-Triplet Superconductivity in Co-Based Josephson Junctions*, Phys. Rev. Lett. **104**, 137002 (2010).
- [15] J. W. A. Robinson, J. D. S. Witt, and M. G. Blamire, *Controlled Injection of Spin-Triplet Supercurrents into a Strong Ferromagnet*, Science **329**, 59 (2010).
- [16] F. S. Bergeret, A. F. Volkov, and K. B. Efetov, *Induced ferromagnetism due to superconductivity in superconductor-ferromagnet structures*, Phys. Rev. B **69**, 174504 (2004).
- [17] F. S. Bergeret, A. L. Yeyati, and A. Martín-Rodero, *Inverse proximity effect in superconductor-ferromagnet structures: From the ballistic to the diffusive limit*, Phys. Rev. B **72**, 064524 (2005).
- [18] P. S. Luo, T. Crozes, B. Gilles, S. Rajauria, B. Pannetier, and H. Courtois, *Spin-valve effect of spin-accumulation resistance in a double ferromagnet/superconductor junction*, Phys. Rev. B **79**, 140508 (2009).
- [19] P. Cadden-Zimansky, Z. Jiang, and V. Chandrasekhar, *Charge imbalance, crossed Andreev reflection and elastic co-tunnelling in ferromagnet / superconductor / normal-metal structures*, New Journal of Physics **9**, 116 (2007).
- [20] D. Beckmann, H. B. Weber, and H. v. Löhneysen, *Evidence for Crossed Andreev Reflection in Superconductor-Ferromagnet Hybrid Structures*, Phys. Rev. Lett. **93**, 197003 (2004).

-
- [21] J. Y. Gu, J. A. Caballero, R. D. Slater, R. Loloee, and W. P. Pratt, *Direct measurement of quasiparticle evanescent waves in a dirty superconductor*, Phys. Rev. B **66**, 140507 (2002).
- [22] J. Xia, V. Shelukhin, M. Karpovski, A. Kapitulnik, and A. Palevski, *Inverse Proximity Effect in Superconductor-Ferromagnet Bilayer Structures*, Phys. Rev. Lett. **102**, 087004 (2009).
- [23] A. Rogachev, T.-C. Wei, D. Pekker, A. T. Bollinger, P. M. Goldbart, and A. Bezryadin, *Magnetic-Field Enhancement of Superconductivity in Ultranarrow Wires*, Phys. Rev. Lett. **97**, 137001 (2006).
- [24] A. Bezryadin, *Quantum suppression of superconductivity in nanowires*, Journal of Physics: Condensed Matter **20**, 043202 (2008).
- [25] G. R. Boogaard, A. H. Verbruggen, W. Belzig, and T. M. Klapwijk, *Resistance of superconducting nanowires connected to normal-metal leads*, Phys. Rev. B **69**, 220503 (2004).
- [26] N. Vercruyssen, T. G. A. Verhagen, M. G. Flokstra, J. P. Pekola, and T. M. Klapwijk, *Evanescent states and nonequilibrium in driven superconducting nanowires*, Phys. Rev. B **85**, 224503 (2012).
- [27] T. Valet and A. Fert, *Theory of the perpendicular magnetoresistance in magnetic multilayers*, Phys. Rev. B **48**, 7099 (1993).
- [28] K. D. Usadel, *Generalized Diffusion Equation for Superconducting Alloys*, Phys. Rev. Lett. **25**, 507 (1970).
- [29] N. Kopnin, *Theory of Nonequilibrium Superconductivity*, International Series of Monographs on Physics Vol. 110, Oxford University Press, New York, 2001.
- [30] J. P. Morten, A. Brataas, and W. Belzig, *Spin transport and magnetoresistance in ferromagnet / superconductor / ferromagnet spin valves*, Phys. Rev. B **72**, 014510 (2005).
- [31] P. Santhanam and D. E. Prober, *Inelastic electron scattering mechanisms in clean aluminum films*, Phys. Rev. B **29**, 3733 (1984).

Summary

In this thesis we study the electronic properties of driven heterostructures. We focus on small, hybrid devices because they offer a unique playground to look at the fundamental properties of solids. They consist of different materials with distinct electronic phases which depend on interactions between electrons and between electrons and the atomic lattice. Electrons in a *normal metal* behave as free, independent particles, scattering on lattice vibrations, impurities or defects in the atomic structures of the solid. In a *superconductor*, electrons attract each other and form a collective state of bound Cooper pairs. This leads to a wealth of intriguing phenomena such as infinite electrical conductivity, perfect magnetic screening, and macroscopic coherence. In a *ferromagnet*, the electron spins align due to the presence of an exchange interaction and the material acquires a net magnetization.

Mesoscale devices are big enough for the emergence of such a collective *macroscopic* states as superconductivity or ferromagnetism. At the same time they are small compared to relevant physical length scales and therefore depend on the *microscopic* properties of the sample. The influence of interfaces and surfaces becomes increasingly more important and the intuitive picture in which different materials with bulk properties are connected by interfaces breaks down. Instead the structure has to be considered as one whole with electronic properties which change gradually on a microscopic level. Near interfaces, ordered electron states compete and interfere, leading to unanticipated phenomena and rich physics. On both sides of the interfaces, currents are carried by different charged carriers. In a superconductor for example, a dissipationless current is carried by Cooper pairs while in a ferromagnet a spin-polarized current is carried by normal electrons. Current conversion processes near the interface lead to a resistance, spin or charge imbalance, and relaxation. Due to their small size, the samples are easily driven out of equilibrium. Even weak electric fields can heat the electron system considerably. This leads to nonlinear behavior because collective states such as superconductivity are affected by an electronic non-equilibrium and at the same time drastically alter the thermal transport.

The samples are deposited on a dielectric substrate. Although the electronic transport occurs in the metal structures only, the dielectric environment has a twofold influence. The electrical energy which is dissipated in the structures is relaxed through the substrate. Hence the electro-thermal behavior of a device can be dominated by the coupling to the substrate and its properties. In addition the driving fields extend beyond the metallic components and interact with the dielectrics.

Reality is complex and the conceptual framework to interpret experiments necessarily includes considerable simplifications. Luckily, the fabrication of the devices leads to certain limitations but also to an enormous freedom to explore a variety of geometries, materials and techniques. This gives us the opportunity to engineer *model systems*, which enhance the physical processes or properties. However, in every experiment it is necessary to assess the validity of the conceptual framework used.

In *Chapters 4, 5, and 6* of this thesis we study the influence of the substrate on the properties of driven superconducting resonators. They consist of coplanar waveguides along which gigahertz electromagnetic fields can travel. When the length L of the superconducting line matches the wavelength λ of the signal, the system becomes resonant. The associated resonant frequency $f_0 = \lambda/v_{ph}$ probes the properties of the superconducting state because of its dependence on the phase velocity v_{ph} . The losses in superconducting resonators are extremely low; a signal can bounce back and forth around a million times before it is dissipated. This makes superconducting resonators extremely sensitive. However, the electromagnetic fields extend beyond the superconducting waveguide and penetrate into the dielectric substrate, the vacuum, and the interfaces between them. Interactions of the fields with dipole moments of two level systems (TLS) lead to increased losses and fluctuations in the phase of the field. The origin of the two level systems is most probably the presence of different atomic configurations in amorphous dielectrics. By carefully engineering the dielectric environment of the resonators, we severely reduce the influence of TLS. This leads to lower losses (*Chapter 4*) and reduce phase noise (*Chapter 5*) in NbTiN resonators. At the same time we identify pieces of bare Si substrate in between the superconducting lines as the region with TLS that dominates the behavior of the resonators.

Because of their excellent sensitivity, superconducting resonators are used as radiation detectors. Photons with energies above the superconducting gap break Cooper pairs into excess quasiparticles. After excitation, the excess quasiparticles recombine over a typical timescale τ_{rec} . Their energy is converted into vibrations of the atomic lattice (phonons). If the generated phonons quickly escape into the substrate, this leads to an effective cooling of the resonator. In practice

however, the hot phonons can transfer their energy again to the electron system by breaking Cooper pairs before they escape to the substrate. In *Chapter 6* we demonstrate how this retrapping effect leads to a tenfold enhanced recombination time for resonators on a thin dielectric SiN_x membrane. In addition we use microrefrigerators based on normal metal superconductor tunnel junctions to heat or cool the phonon temperature of the membrane, while we use the resonator as a sensitive thermometer.

Microrefrigeration in normal metal superconducting tunnel junctions (NIS) is based on the presence of an energy gap Δ in the density of states of the superconductor. Therefore, it is impossible for ‘cold’ electrons with a low energy to tunnel from the normal metal into the superconductor, while ‘hot’ electrons can. By extracting only hot electrons from the normal region, the electron bath is cooled. In *Chapter 6* arrays of 22 parallel Al/ AlO_x /Cu/ AlO_x /Al junctions are used to cool a SiN_x membrane with Aluminum superconducting resonators. Because only the electrons of the Cu island are cooled, we use large Cu cooling fins to thermalize the membrane phonons to the cold Cu electron bath. Subsequently the electron bath of the resonator is cooled because of the thermal coupling to the phonons in Aluminum thin film. As we pointed out, this change in electron temperature of the resonator can be conveniently measured as a change in its resonance frequency. To increase the cooling power of NIS microrefrigerators it would be favorable to move to more transparent tunnel barriers. However, commonly used AlO_x barriers are laterally inhomogeneous, which degrades the cooling performance. In *Chapter 7* we analyze theoretically and experimentally the influence of the uniformity of highly transparent barriers on the charge and energy transport. We demonstrate that AlN barriers have only small lateral variations, comparable to a variance in the barrier thickness of roughly one atomic layer. Furthermore, the high current densities lead to a strong, non-thermal electron distribution in the normal island of stacked Nb(Al)/AlN/Al/AlN/Nb tunnel structures.

In *Chapter 8* we focus on the interplay between electronic non-equilibrium and the superconducting properties in a driven Aluminum nanowire. Normal electrons are injected into the superconducting wire from two massive Cu reservoirs. We demonstrate that this system has two distinct superconducting states under current-driving, which we call a global and a bimodal state. For low bias we find a global superconducting state with most of the resistance occurring as a current-conversion resistance at the ends of the superconducting wires where normal current enters. Although resistive we demonstrate that the whole wire including the edges continues to be in one coherent superconducting state. This state hardly changes for increasing current, until it switches abruptly to the nor-

mal state. On a microscopic level the distribution function changes considerably and is strongly different from the commonly used parabolic temperature profile. For high bias, decreasing the current from a fully normal state, we find that the superconducting state emerges as two decoupled domains at the ends of the wire. The vicinity of the cool equilibrium reservoirs favors the nucleation of the superconducting state at these ends, while strong non-equilibrium at the center of the wire continues to suppress the superconductivity. Upon further lowering of the bias current, the two domains grow in strength until the wire switches back to the low resistive, globally superconducting state.

In *Chapter 9* we study, in a similar system, the inverse proximity effect of a strong ferromagnet on a superconductor. The presence of the ferromagnet locally suppresses superconductivity, but might also induce a magnetization in the superconductor which depends on the nature of the interface. We explore experimentally how a spin-polarized current from ferromagnetic contacts alters the state of a superconducting nanowire. We measure a spin dependence of the two-point resistance of the wire, which is associated with the conversion of a spin-polarized normal current into a supercurrent. In addition we observe similar dependencies in the critical current of the wires. The consistent behavior of the two-probe resistance, together with the spin dependence of the superconducting state, proves this system is promising to improve the understanding of induced magnetism in superconductors. Therefore it would be advantageous to measure the magnetization and the density of states of the wires locally with respectively ferromagnetic and normal tunneling probes.

Nathan Vercruijsen
Delft, May 2013

Samenvatting

In deze thesis bestuderen we de eigenschappen van elektronen in vaste stoffen. Daartoe beschouwen we elektronentransport in kleine, hybride structuren. Deze laatste bestaan uit verschillende materialen, met verschillende atoomroosters, interacties en daarom ook verschillende elektronische grondtoestanden. Elektronen in een *normaal metaal* gedragen zich als vrije, individuele deeltjes die botsen op roostertrillingen, onzuiverheden en defecten in het materiaal. In een *supergeleider* vormen de elektronen een collectieve, macroscopische toestand van gebonden Cooperparen. Dit leidt tot exotische materiaaleigenschappen zoals het totaal verdwijnen van elektrische weerstand, maar ook een perfecte afscherming van magnetische velden. In een *ferromagneet* ontstaat er een spontaan magneetveld doordat de spins van de elektronen uitlijnen.

Mesoscopische structuren zijn groot genoeg voor het ontstaan van dergelijke spontaan geordende elektronische toestanden zoals supergeleiding of ferromagnetisme. Tezelfdertijd zijn de structuren klein ten opzichte van relevante fysische lengteschalen, waardoor de structuur als één geheel beschouwd moet worden in plaats van een aaneenschakeling van aparte entiteiten. Microscopische processen worden zichtbaar en de grens- en oppervlakken van de materialen domineren het gedrag. Competitie en interferentie tussen de elektronische toestanden van verschillende materialen in een hybride structuur, leidt tot onverwachte fenomenen en nieuwe fysische inzichten. Zo wordt aan een supergeleidend-ferromagnetisch contact een weerstandsloze superstroom omgezet in een spin-gepolarizeerde normale stroom. Deze omzetting gebeurt over een lengteschaal die afhangt van de microscopische fysische processen en leidt tot een extra conversieweerstand. Het kleine volume van de structuren zorgt ervoor dat de elektronen gemakkelijk uit thermisch evenwicht gebracht worden. Zo kan zelfs een klein elektrisch stroompje een grote temperatuursverandering teweegbrengen. Het elektronische en thermische transport hangt af van de elektronische grondtoestand, maar deze grondtoestand is op zijn beurt afhankelijk is van de temperatuur, wat leidt tot niet-lineair gedrag.

De structuren worden steeds op een substraat gedeponerd. Hoewel het elek-

tronentransport uitsluitend in de metalen, geleidende structuren plaatsvindt, oefent de diëlektrische omgeving een tweevoudige invloed uit. Ten eerste wordt de energie die vrijkomt door elektrische dissipatie uiteindelijk afgevoerd door het substraat. Daarnaast strekken de elektromagnetische velden zich ver uit, wat leidt tot interactie met de diëlektrica.

De realiteit is complex en elk conceptueel kader waarbinnen experimenten geïnterpreteerd worden bevat beduidende vereenvoudigingen. Gelukkig bestaat er een enorme vrijheid in het ontwerp en de fabricage van de experimentele structuren om verschillende geometrieën, materialen en technieken te combineren. Desondanks is het steeds noodzakelijk om het gebruikte conceptuele kader, met zijn vereenvoudigingen, te toetsen aan de waarnemingen.

In *Hoofdstukken 4, 5 en 6* van deze thesis bestuderen we de invloed van het substraat op de eigenschappen van supergeleidende resonatoren. Deze laatste bestaan uit golfgeleiders voor elektromagnetische straling met frequenties in het gigahertz gebied. Wanneer de lengte van zulke supergeleidende lijnen overeenkomt met de golflengte λ van het signaal, wordt de lijn resonant. De overeenkomstige frequentie $f_0 = \lambda v_{ph}$ hangt af van de fasesnelheid v_{ph} en is daardoor afhankelijk van de eigenschappen van de supergeleider. Ze zijn ook erg gevoelig, omdat het gebruik van een supergeleider erg lage verliezen met zich meebrengt; een elektronisch signaal kan wel een miljoen keer heen en weer reizen in de resonator voor het gedissipeerd wordt. De elektromagnetische golven strekken zich echter uit tot ver buiten de supergeleider; ze doorkruisen het vacuum, het substraat en de grensvlakken in de omgeving. Interacties met dipoolmomenten van het diëlektricum leiden tot een toename van elektronische verliezen en ruis. Door een zorgvuldig ontwerp en fabricage van het diëlektricum rond de resonatoren, slagen we erin om zowel de verliezen (*Hoofdstuk 4*) als de ruis (*Hoofdstuk 5*) gevoelig te verminderen. Tezelfdertijd identificeren we het aan de lucht blootgestelde substraat tussen de resonerende lijnen als de dominante bron ervan.

Dankzij hun goede gevoeligheid worden supergeleidende resonatoren gebruikt als stralingsdetector. Lichtdeeltjes (fotonen) met een voldoende hoge energie kunnen Cooperparen breken en creëren zo vrije quasideeltjes. Dit beïnvloedt de resonantiefrequentie van de resonator wat nauwkeurig gemeten kan worden. Deze quasideeltjes recombineren echter terug tot Cooperparen in een random proces over een tijdspanne τ_{rec} . Daarbij wordt er energie van de quasideeltjes omgezet in roostertrillingen (fononen). Als deze fononen van de supergeleidende film ontsnappen naar het substraat wordt deze energie effectief afgevoerd. In de praktijk breken deze ‘warme’ fononen echter dikwijls opnieuw een Cooperpaar vooraleer ze ontsnappen. In *Hoofdstuk 6* tonen we aan hoe dit effect de recombinatie tijd gevoelig verhoogd in resonatoren op een dun membraan. Bovendien

gebruiken we microscopische koelers om de temperatuur van deze fononen artificieel te verhogen of te verlagen.

Deze koeling maakt geen gebruik van gassen of vloeistoffen, maar is volledige op vastestoffysica gebaseerd. We gebruiken de verschillende eigenschappen van supergeleiders en normale metalen om door middel van een elektrische stroom ook een thermische stroom te genereren. Deze laatste voert warmte van het normale metaal naar de supergeleider. In *Hoofdstuk 6* worden 22 van dergelijke vastestofkoelers gebruikt om een membraan met daarop de supergeleidende resonatoren af te koelen. Om grotere temperatuursverschillen te bekomen zou het nuttig zijn om krachtigere koelers te ontwerpen, die een grotere stroom kunnen voeren. De meeste koelers zijn echter gebaseerd op aluminiumoxide, een materiaal dat door zijn inhomogeniteit problematisch is bij grote stroomdichtheden. Daarom onderzoeken we experimenteel en theoretisch hoe een meer uniform materiaal als aluminiumnitride het koelvermogen zou kunnen verbeteren. We bekijken ook hoe zulke grote thermische stromen het elektronische systeem ver uit evenwicht kunnen brengen.

In *Hoofdstuk 8* beschouwen we de interactie tussen een elektronisch niet evenwicht en de supergeleidende eigenschappen van een aluminium draadje. Daartoe injecteren we ‘hete’ elektronen vanuit massieve koperen reservoirs in de supergeleidende nanodraad. Wanneer we dit doen, observeren we twee verschillende supergeleidende toestanden: een globale en een bimodale toestand. Voor relatief kleine stromen is de draad in de globale supergeleidende toestand, met een elektrische weerstand die veroorzaakt wordt door de omzetting van een normale stroom naar een superstroom. Dit proces vindt plaats in de supergeleider, die daardoor toch een weerstand krijgt. Voor grote stromen ontstaat er een sterk niet-evenwicht in de draad, doordat de energie van de geïnjecteerde elektronen steeds groter wordt. Daardoor verdwijnt de globale supergeleidende toestand abrupt en wordt de draad normaal. Wanneer de stroom vervolgens weer kleiner gemaakt wordt, ontstaan er twee kleine supergeleidende eilandjes aan de uiteindes van de draad, dit is de bimodale toestand. Ze ontstaan in de buurt van de normale reservoirs omdat deze relatief koud zijn, waar het midden van de draad sterk opgewarmd wordt door dissipatie. Wanneer de stroom verder vermindert, groeien de supergeleidende eilandjes tot ze elkaar raken. Op dat moment neemt de draad weer de globale toestand aan.

In *Hoofdstuk 9* bekijken we in een gelijkaardig systeem de invloed van ferromagnetische reservoirs op een supergeleidende draad. De aanwezigheid van een ferromagnetisch materiaal onderdrukt supergeleiding, maar kan tegelijkertijd ook magnetische eigenschappen induceren in de supergeleider. We meten we op welke manier de weerstand van een supergeleidend draadje afhangt van de mag-

netische polarisatie van de reservoirs. We observeren een effect dat groter is dan wanneer de draad normaal is. Deze spinafhankelijkheid observeren we ook in de stroom, waarbij het draadje van de supergeleidende toestand overgaat naar de normale toestand (kritische stroom). Het consistente gedrag van weerstand en kritische stroom in combinatie met de spinafhankelijkheid maken deze geometrie aantrekkelijk voor verdere experimenten om magnetisme in supergeleiders te begrijpen. Daartoe zou een extra ferromagnetisch of normaal draadje nodig zijn om lokaal de eigenschappen van de supergeleidende draad te meten.

Nathan Vercruyssen
Delft, Mei 2013

Curriculum Vitæ

Nathan Vercruyssen

18-01-1983 Born in Antwerp, Belgium

1995-2001 Grammar school
Sint-Jozef-Klein-Seminarie, Sint-Niklaas

2001-2006 M.Sc. Applied Physics
University of Ghent
Master Thesis: *Read-out system for a cosmic ray detector.*
Advisor: Prof. dr. ir. D. Ryckbosch

2007-2013 Ph.D. Research
Delft University of Technology
Thesis: *Non-equilibrium electron transport in mesoscale superconducting hybrids.*
Advisor: Prof. dr. ir. T. M. Klapwijk

List of publications

1. N. Vercruyssen, T. G. H. Verhagen, M. G. Flokstra, J. P. Pekola, and T. M. Klapwijk, *Evanescent states and nonequilibrium in driven superconducting nanowires*, Physical Review B 85, 224503 (2012)
2. N. Vercruyssen, R. Barends, T. M. Klapwijk, J. T. Muhonen, M. Meschke, and J. P. Pekola *Substrate-dependent quasiparticle recombination time in superconducting resonators*, Applied Physics Letters 99, 062509 (2011)
3. R. Barends, N. Vercruyssen, A. Endo, P. J. de Visser, T. Zijlstra, T. M. Klapwijk, and J. J. A. Baselmans *Reduced frequency noise in superconducting resonators*, Applied Physics Letters 97, 033507 (2010)
4. R. Barends, N. Vercruyssen, A. Endo, P. J. de Visser, T. Zijlstra, T. M. Klapwijk, P. Diener, S. J. C. Yates, and J. J. A. Baselmans *Minimal resonator loss for circuit quantum electrodynamics*, Applied Physics Letters 91, 023508 (2010)
5. T. Zijlstra, C. F. J. Lodewijk, N. Vercruyssen, F. D. Tichelaar, D. N. Loudkov, and T. M. Klapwijk *Epitaxial aluminum nitride tunnel barriers grown by nitridation with a plasma source* Applied Physics Letters 91, 233102 (2007)

Acknowledgements

Pursuing a PhD has been both an enriching and challenging experience for me. Here I would like to thank those people who supported me professionally and personally during this period.

Teun, I feel grateful that I had the opportunity to have you as a promotor. Your critical and rational approach of problems, whether scientific or not, still surprises me. You gave me time and freedom to explore, also in difficult times. At the same time you were always there when necessary. Thank you.

In the daily life of an experimentalist I had the joy of working together with some remarkable people. Tony, you introduced me into the clean room. Despite the fact that you were always busy, you made time to share your vast experience. Rami, you were there to give me advise in dealing with a PhD and to push me forward. I particularly enjoyed doing experiments together! Zhu, not only we lived and worked in the same buildings, at a certain moment we in addition spent an enjoyable time designing, fabricating and measuring together! Gao, thanks for your understanding and advise when I was at the same time writing my thesis and diving into the world of HEBs.

In the continuous battle with equipment and administration, I was happily assisted by the ever ready staff. Jack, you were so kind to always solve problems whether it concerned deposition equipment or almost thrown-away sources. Also the help Ron, Raymond, Piet, and Rogier is much appreciated. David, thanks for enduring countless hours in the clean room and for teaching me to use the proper tools for the job. Thanks to all the people of the NAF for your support. Thanks to Maria, but also Monique, Irma, and Dorine, for their patience and to kick me whenever necessary! Thanks to Sofie for helping me with designing figures, logos, T-shirts, and more.

The first student I supervised was Tim. You managed me well! It was a pleasure to witness copper fireworks and nitrogen fountains together, and to have the honor to speak to you at your graduation. With Remco and Robbert-Jan, we struggled through photon absorption in tiny wires, although they never existed in real life. Sir Amar, you are a truly great Master, I wish you all the best.

During a half year stay at the PICO group in Helsinki, I dug into the Finnish way of living and the dynamical atmosphere of this beautiful group. Jukka, thank you for giving me this opportunity, your no-nonsense way of working, and humor. Matthias, thanks for your help, travel advise and the nice dinners! The help of Sergey in the clean room and with the dip-stick-dilution fridge is much appreciated. I liked numerous discussions with Andrey and off course the wednesday sauna with Juha, Tommy and the Blue Frost guys.

In Delft I felt very much at home in the somewhat stubborn group of nano-electronics. The group always extended beyond the lab with tea times, evenings in Delft, memorable trips, and discussions on topics of various interest. A dear friend I almost immediately encountered is Tarun, who taught me about cricket, Indian cooking and the complexities of another culture. This all took place in a shared apartment, which we rented from a Columbian landlady after skillful negotiations by Merlijn. The interaction between the enthusiasm of Gabri, the noise of Rami, and the calm of their roommate Chris was inspiring. Thank you Niels for sailing trips, tea times and plenty more. Thanks to Eduard and Rik for your enthusiasm and discussing virtually anything, one day you guys will win a bet! Thanks to my roommates Franz, Pieter, Jing, and Reinier for enduring my presence, the cold, some music, and the aroma of (over)ripe fruit. Franz, I still remember your countless efforts to make a clean tunnel barrier on a 1x1 mm² sample. Pieter, if one day there is a quiz on dutch and vegetables, we should subscribe. Alibey, thanks for letting me win in ping-pong and for your friendship. Jaime, thanks for joining a 'small' bicycle tour, although with relaxing frisbee at the beach. Thanks to Cosmonanorunners Akira, Alessandro, Rik, Dorine, Bastian, and Cristina for enduring running with me. David, we will run a marathon together! Thanks to Dàvid for cycling with me and the many coffees in the morning. Also thanks to Dennis, Mihai, Morris, Pieter-Jan, Jochem, students and former group members. Marc, if you join the group, it will be my turn to visit Delft for enjoying Belgian beers together. Thanks to Yuan, for the honor of being his paranymp. Akira, discussing physics with you always inspires me with the friday afternoon club as a climax! In short, I feel grateful to have been part of this enthusiast group!

Finally, this work would have been impossible without the unconditional support from friends and family, and the love of the most caring person during all of these years, Valérie. Thank you.